12-2010

A computational method for analysis of material properties of a non-pneumatic tire and their effects on static load deflection, vibration and energy loss from impact rolling over obstacles

Akshay Narasimhan
Clemson University, anarasi@clemson.edu

A COMPUTATIONAL METHOD FOR ANALYSIS OF MATERIAL PROPERTIES OF A NON-PNEUMATIC TIRE AND THEIR EFFECTS ON STATIC LOAD-DEFLECTION, VIBRATION, AND ENERGY LOSS FROM IMPACT ROLLING OVER OBSTACLES

A Thesis
Presented to
The Graduate School of
Clemson University

In Partial Fulfillment
Of the Requirements for the Degree
Master of Science
Mechanical Engineering

By
Akshay Narasimhan
August 2010

Accepted by:
Dr. Lonny L. Thompson, Committee Chair
Dr. Sherrill Biggers
Dr. John C Ziegert

ABSTRACT

One of the potential sources of vibration during rolling of a non pneumatic tire is the buckling phenomenon and snapping back of the spokes in tension when they enter and exit the contact zone. Another source of noise was hypothesized due to a flower pedal ring vibration effect due to discrete spoke interaction with the ring and contact with the ground during rolling as the spokes cycle between tension and compression. Transmission of vibration between the ground force, ring and spokes to the hub was also considered to be a significant contributor to vibration and noise characteristics of the Tweel. Previous studies have studied spoke vibration, ground vibration and related geometrical factors on a two-dimensional (2D) Tweel model. In the present work, a three-dimensional finite element model of a non-pneumatic tire (Tweel) was considered which uses a hyperelastic Marlow material model for both ring and spokes based on uni-axial test data for Polyurethane (PU). Changes in material properties on static load-deflection curves and vibrations of spoke and ground force reaction during high-speed rolling are studied. In addition, energy loss upon impact with an obstacle is also studied.

For static load deflection studies, a new analysis procedure is developed which allows for a cooling step to proceed prior to loading, and yet maintains continuous contact with the ground. For the dynamic rolling studies, a direct analysis procedure is developed, where the Tweel is accelerated from rest. This procedure avoids potential numerical difficulties when defining nonzero initial speeds as used in previous studies. In order to study the effect of changes in shear modulus for the ring and spokes while

keeping the ratio of volumetric bulk modulus to shear modulus unchanged, the value of shear modulus is varied from Mooney-Rivlin and Neo-Hookean models obtained from a least-squares fit of the uni-axial stress-strain data. A total of 6 different material models are examined together with the original Marlow model. The 6 material models are divided into 2 sets and each set has 3 levels (unchanged and plus/minus 25% change in shear modulus).

Upon evaluation of the uniaxial data, the results show that on increasing the shear modulus, the tangent slope of the normal stress-strain curve increases; whereas with decreasing shear modulus, the slope decreases. For tensile stresses and strains, the Mooney-Rivlin best matches the original Marlow material model, compared to the simpler Neo-Hookean model. However, for large compressive stresses, the Mooney-Rivlin diverges significantly from the Marlow curve. The simple Neo-Hookean model is able to fit the Marlow curve better for compression, but is less accurate in tension. As a result of decreasing shear modulus, the vertical displacement in the static load-deflection curves increases upon loading. The Neo-Hookean model resulted in decrease in stiffness when compared to the Mooney-Rivlin and original Marlow model.

The effects of material changes on spoke vibration as measured by changes in perpendicular distance and vibration in ground interaction measured by FFT frequency response of vertical reaction force during rolling are also reported. Results show a trend the vibration decreased when the stiffness of the Mooney Rivlin and the Neo Hookean models was increased from +25% to -25%. Conversely, the vibration increased when the stiffness decreased between the extreme limits. However, in several of the material

models for the ring and spokes, the unchanged stiffness gave the lowest vibration amplitude, suggesting that a optimal value is somewhere between the plus/minus 25% stiffness limits.

To study energy loss the 3D finite element model of the Tweel is rolled over an obstacle whose height is 7.5% of the radius of the Tweel. Energy loss is measured by the reduction in axial hub velocities and kinetic energies (KE) relative to an analytical rigid wheel with the same mass, moment of inertia and initial velocity. Results show that the reference Tweel with Marlow material properties, after traversing the obstacle, resulted in an average reduction in axial velocity and total kinetic energy of only 1.3% and 2.3%, respectively. Results show that for Mooney Rivlin, a decrease in shear modulus caused a decrease in energy loss. Conversely, for Neo Hookean, a decrease in shear modulus resulted in an increase in energy loss and an increase in shear modulus resulted in a decrease in energy loss.

DEDICATION

This thesis is dedicated to my parents, Mr. R. Narasimhan and Mrs. Hemalatha Narasimhan.

ACKNOWLEDGMENTS

I offer my deepest gratitude to my research advisor Dr. Lonny L. Thompson who was abundantly helpful and offered invaluable assistance, support and guidance throughout this research project and for my thesis writing. I attribute the level of my Masters degree to his encouragement and effort without which this thesis would not have been completed. I would like to thank Dr. Sherrill Biggers and Dr. John C. Ziegert for serving on my committee and for their valuable suggestions for improving my thesis.

I would also like to thank Dr. Timothy Rhyne and Mr. Steve Cron of Michelin and Dr. Andreas Obieglo of BMW for their abundant personal assistance and for financial support for this research project.

TABLE OF CONTENTS

LIST OF TABLES

LIST OF FIGURES

CHAPTER ONE - INTRODUCTION

John Boyd Dunlop developed the pneumatic wheel in the late 18th century. The importance of the pneumatic wheel was realized when it was rolled along with a rigid wheel on a rough terrain paved with cobble stones. During impacts with obstacles, the pneumatic wheel was at an advantageous position than the rigid wheel due to different characteristics. These are termed as the critical characteristics of the pneumatic wheel and are discussed in detail in [1].

Over the years, constant efforts have been made to improve the design of the pneumatic wheel. However, even the current design of the pneumatic wheel has its disadvantages such as inflation loss from punctures, regular maintenance to keep correct air pressure and durability. In addition, with different constraints imposed on the current design of the pneumatic wheel, there is no optimal design till date. These constraints are explained in [1]. As a solution to these prevailing problems, a non-pneumatic wheel design called a Tweel was proposed by Michelin Engineers, T. B. Rhyne and S. M. Cron. This design not only possesses the critical characteristics of the pneumatic wheel, but also expands the limited design space provided by the pneumatic wheel [1]. A prototype Tweel used for testing at Michelin and the Clemson University International Center for Automotive Research (CU-ICAR) is shown in Figure 1.1.

Figure 1.1: Tweel Prototype at CU-ICAR

1.1 Critical Characteristics

The pneumatic tire possesses four important characteristics. These characteristics were recognized from the behavior when impacting obstacles [1] and used to design the structure of the Tweel.

1. Low contact pressure for the non pneumatic wheel was achieved by replacing the inflation pressure with a circular beam which deforms primarily in shear. This beam is comprised of two in-extensible membranes separated by a relatively low elastic modulus material layer.
2. Low stiffness for the non pneumatic wheel was proposed by connecting the elastic layer to the hub using thin deformable elastic spokes.

3. Low mass for the non pneumatic wheel is achieved by having the same structure as the bicycle wheel (invention of the tensioned spokes). This is explained in detail [1].
4. Finally, the most important characteristic, low energy loss from impacting obstacles is achieved by designing a Tweel with similar mass, moment of inertia as the pneumatic tire. When rolling with the same initial velocity over an obstacle, it was observed that the Tweel loses less energy compared to the pneumatic wheel.

1.2 Salient Features of the Tweel™

It has been explained in [1] that the non-pneumatic Tweel possesses the critical characteristics seen in the pneumatic wheel. These characteristics compliment the design of the non-pneumatic wheel, thereby increasing the design space and eliminating many constraints.

The contact pressure and the vertical stiffness of the non pneumatic wheel are decoupled unlike the pneumatic structure where they are interdependent. In this new proposed structure, combinations like high contact pressure / low stiffness and low contact pressure / high stiffness can be achieved.

The stiffness curve for the non pneumatic wheel can be adjusted according to the design requirements. On the other hand, the pneumatic wheel always acts like a slightly hardening spring.

With the shear beam replacing the inflation pressure, it eliminates the need for an enclosed space to hold the compressed gas and also saves a lot of weight. The shear beam also eliminates the need for maintaining optimal inflation pressure

1.3 Non Pneumatic Wheel design

The proposed non-pneumatic structure consists of three basic parts: a circular deformable beam, thin elastic collapsible spokes and a rigid hub. To come up with a practical integrated structure, thin elastic collapsible spokes connect the rigid hub and the shear beam. The use of these spokes is an easily understood approach but other alternatives can be used [1].

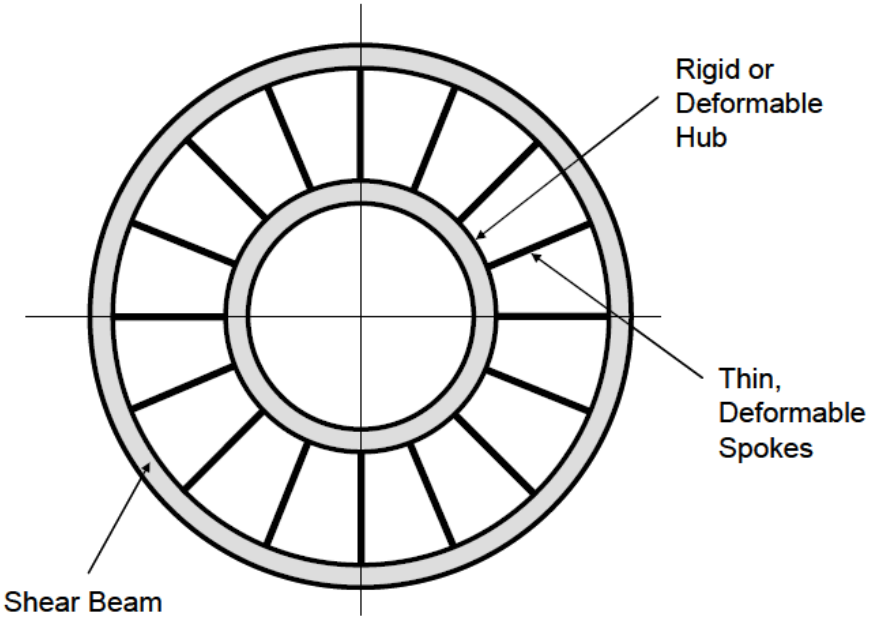

Figure 1.2: Initial TWEEL setup where the ring is connected to the rigid hub using thin deformable spokes, [1].

The circular deformable beam in the Tweel consists of a relatively low modulus elastic layer sandwiched between two surfaces. This beam deforms almost entirely due to shear and hence it is called the shear beam. The shear beam performs the function of the inflation pressure in the pneumatic tire. The two surfaces, also called in-extensible

membranes, are thin with low stiffness in the radial direction but high stiffness in the circumferential direction.

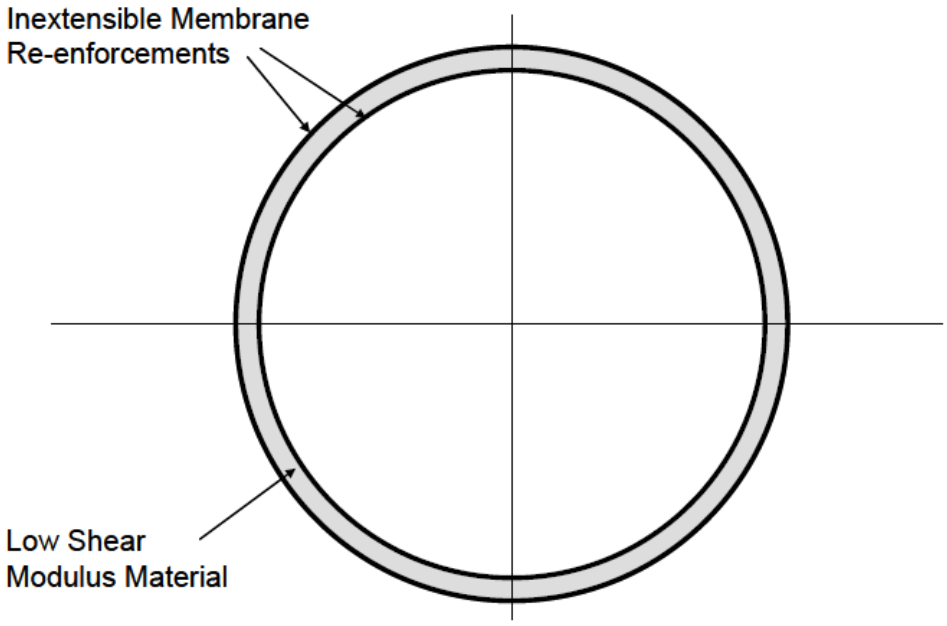

Figure 1.3: Components of the integrated ring structure [1].

When loaded, the shear beam deforms in the contact region. The spokes have a very low critical buckling load. In the contact region, these spokes buckle and effectively carry no load. Due to this phenomenon, the shear layer is compressed and creates a contact patch with the ground. When the shear beam is flattened in the contact region, it takes a shorter path to complete the original circle. This signifies that there is a loss of length of the shear beam. It is well known that the shear beam is in-extensible due to the membranes and hence there are two ways to account for the loss of length. The length can go into a long contact patch or it can be accounted for the increase in the beam

diameter. If the stiffness of the spokes is low, the ring expands and the contact patch becomes small. On the other hand, if the stiffness of the spokes is high, the ring resists expansion and excess length goes in increasing the contact length [1].

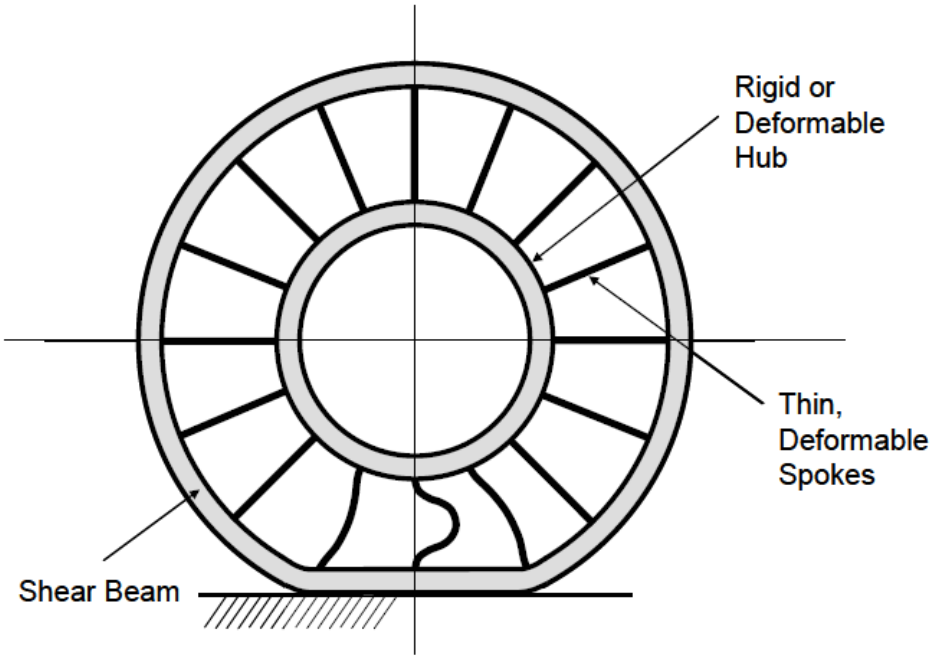

Figure 1.4: The buckling phenomenon of the spokes in the contact region when a load acts on the TWEEL [1].

1.4 Current Tweel design

The current Tweel design considered in this work is molded from polyurethane (PU) and consists of five different parts: (1) Ring, (2) Reinforcements, (3) Spokes, (4) Tread and (5) Rigid hub. A 3D geometric model of the Tweel created using ABAQUS/CAE v6.8 and v6.9 is shown in Figure 1.5.

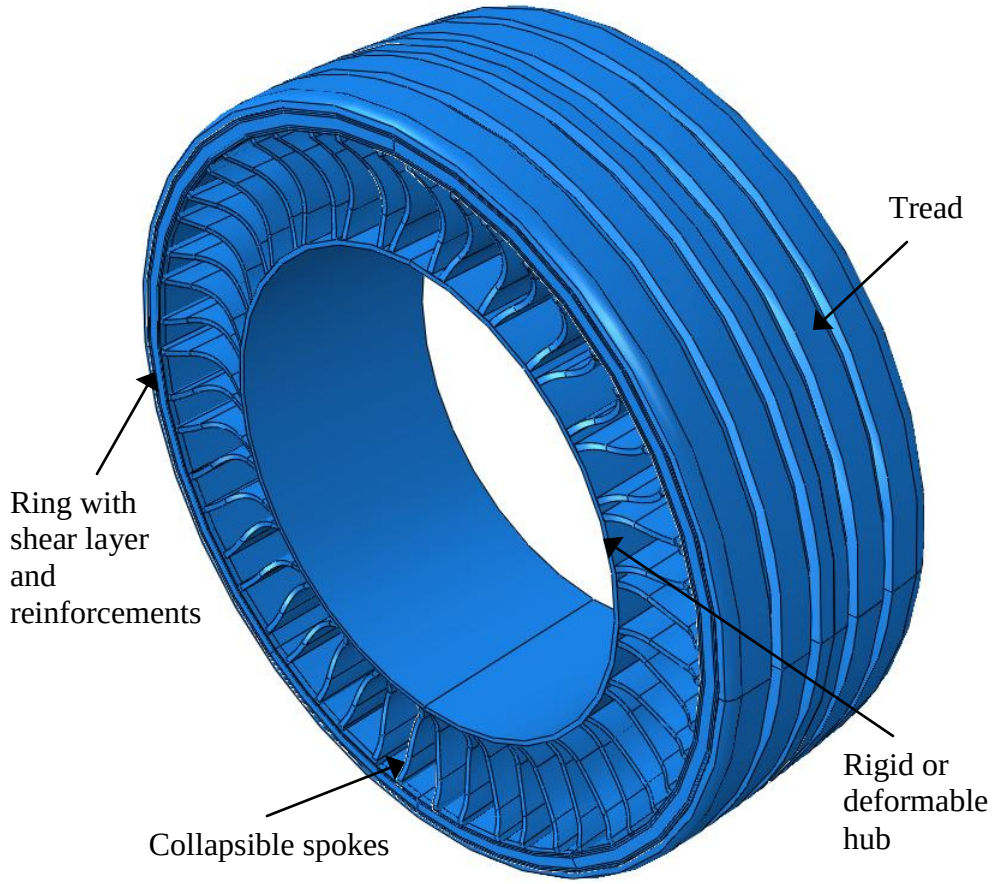

Figure 1.5: Isometric view of 3D TWEEL model consisting of the rigid hub, collapsible spokes, ring and the tread.

The ring is a composite structure consisting of a shear beam and in-extensible membranes. These membranes are embedded inside the ring structure. These in-extensible membranes are also called reinforcements due to the high stiffness and strength of these membranes in the circumferential direction. The number of reinforcements in the shear ring varies by design but a minimum of two is required to form the shear beam behavior. The reinforcements flank the shear beam on either side thereby dividing the ring into number of layers depending on their number. In this work, the Tweel is designed for the BMW Mini Cooper with specified dimensions for the

outside diameter and hub diameter and uses two reinforcement membranes in the shear ring, see Figure 1.6.

Figure 1.6: Isometric view of the 3D shear ring model and reinforcement membranes.

As stated, the Mini Cooper Tweel has 2 in-extensible membranes flanking the shear beam and hence divides the ring into three layers; the shear layer and outer and inner coverage. The reinforcement that is situated nearer to the hub center is called the inner reinforcement. The other reinforcement is called the outer reinforcement. Also, the section of the ring above the inner reinforcement is called the inner coverage while the section of the ring below the shear beam is called the outer coverage; see Figure 1.7.

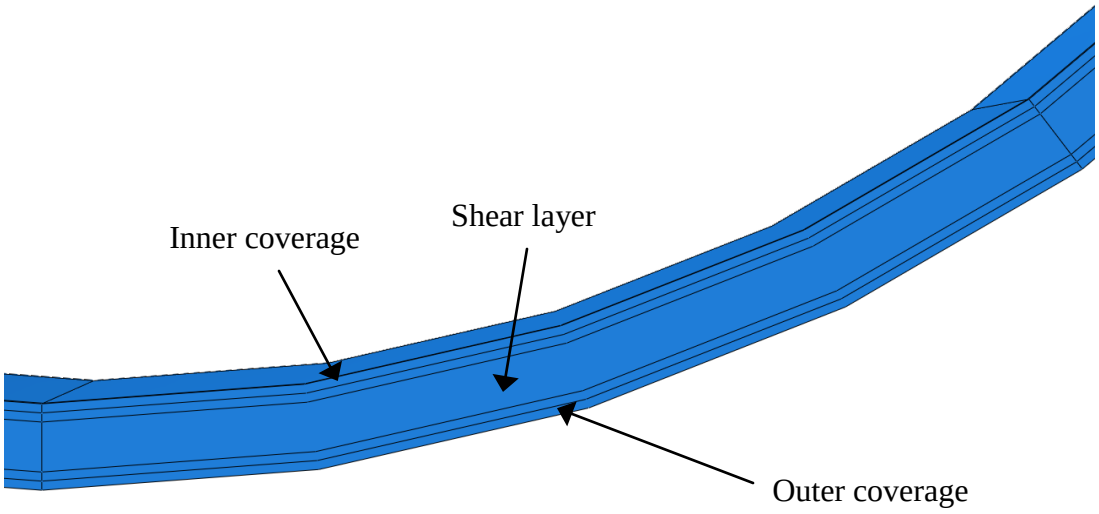

Figure 1.7: Different parts of the 3D Ring

In addition to the ring, a rubber tread is also modeled. The tread establishes contact with the ground and helps in providing traction.

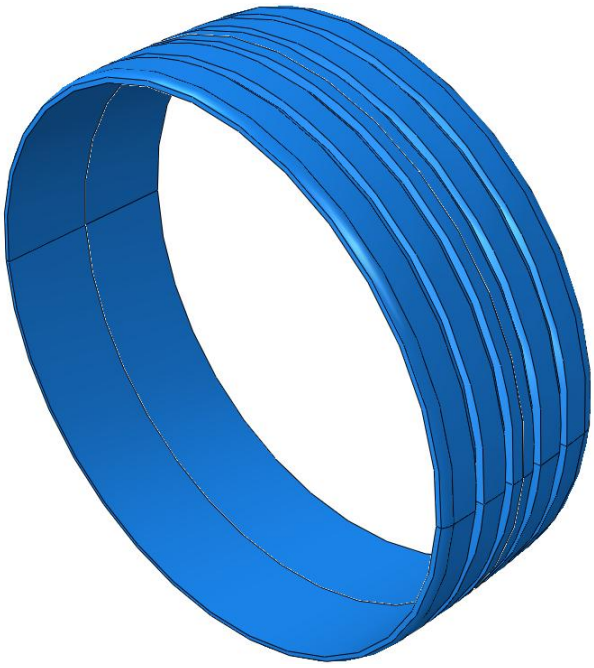

Figure 1.8: Isometric view of the 3D Tread.

The collapsible spokes that are used in these models connect the ring and the rigid hub. The spokes, unlike the initial design of the Tweel, has a curvature, thickness and also deviates from the radial line. The spokes are paired and placed at equal intervals along the circumference of the Tweel.

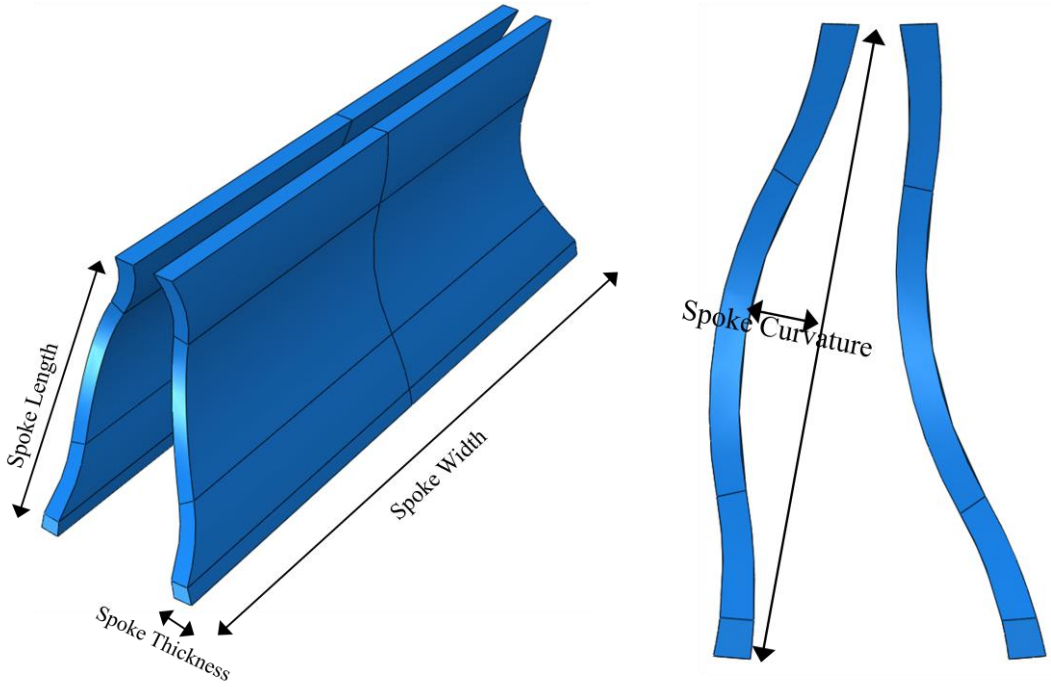

Figure 1.9: Geometric aspects of the 3D collapsible spoke

1.5 Previous Work

In [1], it was stated that spoke dynamics at high speed rolling was one of the issues of the Tweel and needed more attention. When rolling at high speeds, if not designed properly, the Tweel can produce unwanted noise and spoke vibration which might reduce the durability of the spoke. In [3-9], the noise was hypothesized to be due to

the buckling phenomenon of the spoke when entering and leaving the contact zone and the resulting vibration during the tension phase of the spoke as it passes around the top portion of the rotating wheel. In [10] another source of noise was hypothesized due to a flower pedal ring vibration effect due to discrete spoke interaction with the ring and contact with the ground during rolling as the spokes cycle between tension and compression. Transmission of vibration between the ground force, ring and spokes to the hub was also considered to be a significant contributor to vibration and noise characteristics of the Tweel.

In [2], spoke dynamics was investigated by analyzing a single 3D spoke in ABAQUS. The 3D spoke was tied to point (hub center) using different connector elements and was rotated. A 3% static tensile strain was imposed on the spoke and was then accelerated to a speed of 80 km/hr. This is equivalent to simulating a Tweel rolling at a high speed over a rigid surface.

The research work in [3] involved the development of a computational procedure for simulating high speed rolling of a Tweel in contact with a rigid plane. In addition, the spoke vibration frequencies were monitored and the spoke length vs. time profile was obtained. This served as an input boundary condition for a 3D Tweel spoke to capture in-plane and out-of-plane vibrations. From the computational procedure, it was concluded that the spoke vibrations were not significantly affected by the thickness of the spoke. From the 3D spoke analysis, significant out-of-plane vibrations were captured which were not present in the 2D Tweel models.

In the research work of [4], changes were made to modeling techniques to accurately represent the cooling and loading phases during steady state rolling using ABAQUS/Explicit. In addition, the single 3D spoke was analyzed under high speed rolling conditions. From this analysis was concluded that scalloping the edges of the spoke drastically reduced the vibration amplitude but did not have a strong effect on the dominant frequency. An optimal amount of scalloping was suggested.

In [5], important spoke and ring (geometric) parameters were considered for vibration and were studied using Taguchi's Robust Parameter Design and orthogonal arrays. To evaluate every combination, set of output parameters such as perpendicular distance of the spoke from a virtual plane, ground reaction forces due to vibration of the Tweel and ring vibration were monitored and compared. Increasing spoke curvature and decreasing spoke length resulted in decreasing the magnitude of the output parameters.

In the research work of [6], a systematic study of the effects of spoke angle deviations from radial lines (DeRad) was performed using Taguchi's Robust Parameter Design Method and Orthogonal Arrays. Also, effects of a new alternate spoke pair concept wherein every other pair has same thickness, curvature, or combinations of both were examined. It was concluded that DeRad did not affect the spoke and ground vibration as much as spoke curvature and spoke length. On comparing with a reference model having uniform spoke thickness, the alternating spoke pair model with plus/minus 5% difference in thickness between the odd and the even spoke resulted in reducing the RMS and maximum amplitudes, and also spread out the excitation frequencies of the ground force reaction.

In [7], more importance was given to other parameters of the Tweel although the spoke thickness and spoke curvature were the most influencing parameters. Also, an additional L_8 orthogonal array with variables of shear beam thickness, inner coverage, and outer coverage, leaving appropriate columns open to expose interactions between the ring variables was created. All key geometric variables were combined and included the effects of uncontrollable factors of rolling speed and ground pushup in a Robust Parametric Design study. For a complete study, a L_{27} orthogonal array was proposed with combinations of 9 geometric design parameters considered as control factors with three levels each. It was concluded that the Tweel stiffness is dominated by the change in spoke thickness as compared to the change in number of spoke pairs. Spoke curvature was concluded to be the most important parameter which influenced ground and spoke vibration. Strong interactions were found between the ring variables such as shear beam, inner and outer reinforcements.

In the computational studies in [3,4], the analysis procedure consisted of an nonzero initial condition followed by a ground and hub center motion. This allowed for a steady-state rolling condition with constant speed (zero acceleration) to be achieved without starting from rest and accelerating up to steady speed, resulting in significantly reduced compute time. In [5,6,7], a different analysis procedure is used with the same goal of starting the analysis with an initial nonzero speed. While these procedures give effective results for studying steady-state rolling, they do not allow for the possibility of a ground which includes obstacles. In addition, all of the full Tweel rolling models used previously where 2D planar models which are approximations to the physical 3D Tweel

structure. While many of the geometric features of the Tweel are planar and projected in the width dimension to form a 3D structure, some components are not entirely planar, such as the spokes and tread which have a taper across the width dimension. In addition, the grooves in the tread can only be captured in a 3D model of the Tweel.

1.6 Thesis Objectives

In this work, the computational procedure is expanded to a complete 3D model of the Tweel including a detailed model of the 3D geometry of the spokes and tread. Since the model is 3D, the idealized orthotropic properties of the reinforcements in the 2D planar model, are treated more accurately with 3D geometric effects. In addition, a major goal of this work is to investigate energy loss due to Tweel impact over obstacles; a new analysis procedure is developed. In this procedure, rolling is started from rest and accelerated to steady speed and then held constant prior to impacting ground obstacles. For efficiency, the static load is applied during the acceleration step prior to reaching a steady speed. History outputs of hub velocity and kinetic energy are also reported. The flat ground surface also had to be modified to model the shape of a typical obstacle, and a friction model between the ground and wheel tread contact was also utilized.

For static load deflection studies, a new analysis procedure is developed which allows for a cooling step to proceed prior to loading, and yet maintains continuous contact with the ground.

In addition to the study of energy loss, another objective was to study spoke vibration and ground force vibration during steady rolling without any assumptions or potential artificial numerical artifacts due to approximations of nonzero initial speed in

the Abaqus model. The benefit of starting the simulation from rest in the new analysis procedure, allows for vibration results during rolling which should better compare to physical experiments. Since the analysis steps start from rest, the total time required by the solver to fully accelerate to the desired steady speed is greater than previous studies using approximate nonzero startup procedures. As a result, the analysis requires significant CPU processing time. To solve this problem, all analysis are performed on the Clemson Palmetto computer cluster, with multiple processors and compute cores in a highly paralyzed environment facilitated by Abaqus/Explicit finite element software.

Both geometric and material properties play an important role in the performance of tires. In previous work, geometric factors were studied on the vibration of spokes and ground force interaction of a rolling non-pneumatic tire. In this present work, material factors are considered. Changes in material properties on static load-deflection curves, energy loss rolling over obstacles, and vibrations of spoke and ground force reaction during rolling are studied. For this study, a 3D finite element model of a non-pneumatic tire was considered which uses a Hyperelastic Marlow material model for both ring and spokes based on uni-axial test data for Polyurethane (PU). In order to study the effect of changes in shear modulus for the ring and spokes while keeping the ratio of volumetric bulk modulus to shear modulus unchanged, the value of shear modulus is varied from Mooney-Rivlin and Neo-Hookean models obtained from a least-squares fit of the uni-axial stress-strain data. A total of 6 different material models are examined together with the original Marlow model. The 6 material models are divided into 2 sets and each set has 3 levels (unchanged and plus/minus 25% change in shear modulus). In addition to static

load-deflection curves which are important for vehicle design integration, the effects of material changes on spoke vibration as measured by changes in perpendicular distance and vibration in ground interaction measured by FFT frequency response of vertical reaction force during rolling are also reported.

Another goal is to compute the energy loss of the current 3D Tweel model as it traverses an obstacle. In this work, a computational procedure is developed to study the effects of changes in shear modulus on Kinetic energy loss during impact over obstacles. Reduction in Kinetic energy and velocity after traversing an obstacle results in a smaller change in linear momentum, implying reduced linear impulse, which in turn leads to reduced harshness over rough surfaces. Results of the 3D Tweel model are compared with a rigid wheel finite element model having the same mass, outside radius, and moment of inertia as that of the Tweel. An analytical model of the rigid wheel with a simplified analysis of the obstacle is also developed and is compared with FEA models of both the Tweel and rigid wheel.

An outline of the thesis is as follows.

In Chapter 2, details of the material and geometric features of the 3D Finite Element Tweel model are described, including mesh and element properties and interactions and constraints. At the end of this chapter, the new analysis procedure from rolling starting from rest is given.

In Chapter 3, a comparison of stress-strain curves for the PU material and hyperelastic models with different shear modulus is given.

In Chapter 4, the effects of shear modulus on the slope and magnitude static load vs. displacement curves are studied. The slope of these curves gives a measure of the vertical stiffness of the Tweel which is a key design variable for vehicle integration.

In Chapter 5, vibration due to steady-state rolling on a flat ground is studied. Measures of vibration include changes in perpendicular distance from a virtual plane of a spoke, and ground force interaction. Vibration amplitudes and frequencies are quantified using Fast Fourier Transform (FFT) response of the time-dependent signals during rolling.

In Chapter 6, results for energy loss during rolling over an obstacle are reported and compared.

Finally, in Chapter 7, conclusions are made and suggestions are given for future work.

CHAPTER TWO - 3D FINITE ELEMENT TWEEL MODEL

In previous works [3-10], the Tweel™ model was a 2D planar model generated using a Abaqus/CAE plug-in and Python scripts. As discussed earlier, in this work a 3D Tweel model is used. The original 3D geometric model was constructed by Steve Cron at Michelin [11]. The finite element mesh and materials in this 3D model are modified for studies of the shear modulus in the PU material in the ring and spokes. Different element types are defined for the static and dynamic/explicit analysis performed in this work. In addition, a new analysis step procedure was developed to allow rolling from rest and the ground was recreated to construct obstacles for energy loss studies. The geometric dimensions of the 3D Tweel that are used for analysis purposes are given in Table 2-1. The geometric model of the 3D Tweel is shown in Figure 2.1.

Table 2-1: Reference Tweel™ model parameters

Parameters	Reference Tweel Model
Outside Diameter	584 mm
Inside Diameter	422 mm
Tread Thickness	5 mm
Ring Thickness	15 mm
Outside Coverage	8.3 mm
Inside Coverage	3 mm
Number of Spoke Pairs	25
Spoke Thickness	4.2 mm
Spoke Curvature	8 mm

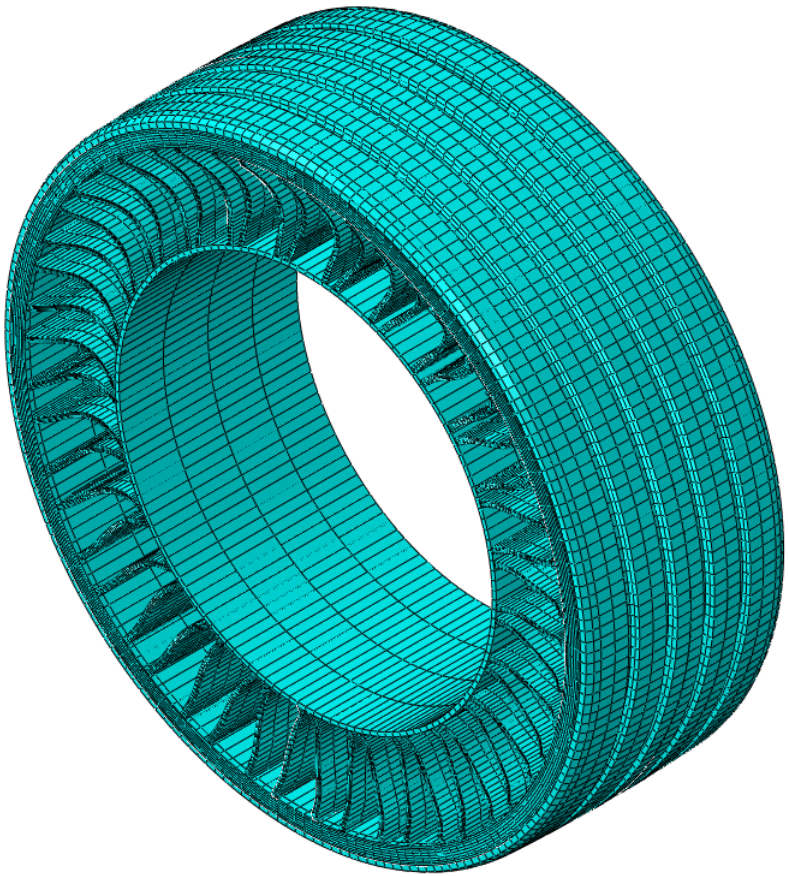

Figure 2.1: Finite Element Model of the TWEEL

2.1 3D Tweel Model Material Properties

The 3D Tweel model consists of two different materials; Isotropic Hyperelastic materials for the ring, spokes, reinforcement surface and tread, and Orthotropic Elastic material for the reinforcements.

Hyperelastic materials are isotropic, nonlinear and show instantaneous elastic responses up to large strain values. On the other hand, elastic materials are valid for only small elastic strains and can be isotropic or orthotropic. Depending on the number of

symmetry planes passing through every point, an elastic material can be classified into isotropic, anisotropic and orthotropic. Symmetry planes refer to the number of axes of rotational symmetry. Isotropic material has infinite number of symmetry planes whereas an orthotropic material has two or three orthogonal symmetry planes. Hence, the mechanical properties for orthotropic materials vary in different directions [13].

The default/reference 3D model has Hyperelastic Marlow uni-axial stress-strain properties for the shear beam, reinforcement surface and collapsible spokes. The same properties are used for the shear beam and spokes to model the Polyurathane (PU), while the reinforcement surface has different properties.

2.1.1 Isotropic Hyperelastic material for the shear beam, collapsible spokes, tread and reinforcement surface

The materials for the shear beam collapsible spokes are modeled with an Isotropic Hyperelastic model. The constitutive behavior of a Hyperelastic material is defined based on a stress-total strain relationship. These materials are very often considered to be incompressible [12]. In this work, three different material models have been used for measuring spoke vibration, ground reaction force and strains on the spokes.

The Marlow properties are defined by the experimental stress-strain test data provided by Michelin. The density of the material is given in daN.sec^2/mm^4 and the thermal expansion coefficient is defined in /^{o} C. As mentioned earlier, the Marlow properties are the same for both the shear beam (ring) and the collapsible spokes but are different for the reinforcement surface. The mass density and thermal expansion

coefficients for the different parts are summarized in Table 2-2. The Poisson's ratio for this material model is 0.45 which is nearly incompressible.

Table 2-2: Density and Thermal expansion coefficients for the ring, spokes and the reinforcement surface

	Ring and Spokes	Reinforcement Surface
Density	1.1E-10 daN.sec^2/mm^4 (1100 kg/m^3)	1.8E-010 daN.sec^2/mm^4 (1800 kg/m^3)
Thermal Expansion coefficient	0.0002 /^{o}C	1.2E-005 /^{o}C

The other types of Hyperelastic material models that are utilized for comparison to the Marlow model are the Mooney-Rivlin and the Neo-Hookean material models. Mooney-Rivlin is a particular case of the Polynomial form strain energy potential. This polynomial strain energy material model [12] is described as shown below.

$$U = \sum_{i+j=1}^{N} C_{ij}(\bar{I}_1 - 3)^i(\bar{I}_2 - 3)^j + \sum_{i=1}^{N} \frac{1}{D_i}(J_{el} - 1)^{2i}$$

The parameter N can take up to 6 values but values more than 2 are not used when the first and second invariants are used for defining the material model [12]. The first and the second invariants are defined as shown below,

$$\bar{I}_1 = \bar{\lambda}_1^2 + \bar{\lambda}_2^2 + \bar{\lambda}_3^2$$

$$\bar{I}_2 = \bar{\lambda}_1^{-2} + \bar{\lambda}_2^{-2} + \bar{\lambda}_3^{-2}$$

The deviatoric stretches can be defined as $\bar{\lambda}_i = J^{-\frac{1}{3}}\lambda_i$. J is the total volume strain and all λ_i are principal stretches [12]. The total volume strain J can be broken into two

components namely J^{el} and J^{th}. The following relation can be established to define the total volume strain,

$$J^{el} = \frac{J}{J_{th}}$$

J^{th} follows from the linear thermal expansion,

$$J^{th} = (1+\varepsilon_{th})^3,$$

where ε_{th} depends on the temperature and isotropic thermal expansion coefficient.

$$\varepsilon_{th} = \alpha_{th}\Delta T$$

The D_i values relate to compressibility of the model. If all D_i are zero, then the model is fully incompressible. If D_1 is zero, all other D_i should be zero. The D values are related to the initial bulk modulus of the material model K_0. Similarly, the values of C_{ij} are related to the initial shear modulus of the material model μ_0.

For the material to be consistent with linear elasticity in the limit of small strains, it is necessary for the initial moduli to be defined as,

$$\mu_0 = 2(C_{10} + C_{01})$$

$$K_0 = \frac{2}{D_1}$$

where μ_0 is the initial shear modulus and K_0 is the initial bulk modulus. The shear modulus controls the material distortion, whereas the bulk modulus controls the volume change. For Hyperelastic materials, the relative compressibility of a material can be determined from the ratio of the initial bulk modulus over the initial shear modulus, i.e.

K_0 / μ_0. These coefficients, in the form of a ratio can be related to the Poisson's ratio by the formula,

$$\nu = \frac{3K_0/\mu_0 - 2}{6K_0/\mu_0 + 2}$$

Using this relation, numerous material models can be derived for a fixed Poisson's ratio and/or the ratio between initial shear and bulk modulus. A few values for the relative compressibility to distortion ratio and its corresponding Poisson's ratio are given below in Table 2-3.

Table 2-3: List of K_0/μ_0 values and their corresponding Poisson's Ratio

K_0/μ_0	υ
10	0.452
20	0.475
50	0.49
100	0.495
1000	0.4995
10,000	0.49995

If no value is given for the material compressibility for a hyperelastic material in ABAQUS, default values of 0.475 for the Poisson's ratio and 20 for the ratio between initial bulk modulus and the initial shear modulus are taken.

From the above displayed equations for the polynomial form, we can derive the Mooney Rivlin material model. This model is obtained when N=1 such that only the linear deviatoric strain energy terms are retained. This model is defined as,

$$U = C_{10}(\bar{I}_1 - 3) + C_{01}(\bar{I}_2 - 3) + \frac{1}{D_1}(J_{el} - 1)^2$$

$$\mu_0 = 2(C_{10} + C_{01}), \quad K_0 = \frac{2}{D_1}$$

A reduced polynomial form can be obtained from the above equations established for the Polynomial form by setting all C_{ij}=0 for j≠0. This model is as shown below,

$$U = \sum_{i=1}^{N} C_{i0}(\bar{I}_1 - 3)^i + \sum_{i=1}^{N} \frac{1}{D_i}(J_{el} - 1)^{2i}$$

The Neo-Hookean material model is a particular case of the reduced polynomial form. It is obtained by setting N=1 [8], and results in the following form of strain energy potential,

$$U = C_{10}(\bar{I}_1 - 3) + \frac{1}{D_1}(J_{el} - 1)^2$$

$$\mu_0 = 2(C_{10}), \quad K_0 = \frac{2}{D_1}$$

The Neo-Hookean model can also be viewed as the Mooney-Rivlin model specialized with C_{01} = 0. The Neo-Hookean model is the simplest of the hyperelastic models and is often used in the absence of accurate material data. On the other hand, the Mooney-Rivlin material model is an extension of the Neo-Hookean form and has an additional term that depends on the second invariant of the Cauchy-Green tensor, enabling a better fit of experimental stress-strain test data.

The material model that is used for the tread of the Tweel™ is a hyperelastic material model with Neo-Hookean strain energy potential. The shear modulus μ_0 and the bulk modulus K_0 are dictated by the coefficients C_{10} and D_1. The density of the material is $1.1e10^{-10}$ daN.sec^2/mm^4 (1100 kg/m^3), and the thermal expansion coefficient is .00017/^{0}C. The coefficient C_{10} is given as 0.0833, corresponding to an initial shear modulus of 0.1666 daN/mm^2, and coefficient D_1 is given as 1.241384, corresponding to an initial bulk modulus of 1.61 daN/mm^2. The specific Hyperelastic material coefficients defined for the spokes and shear beam will be discussed in detail in Chapter 3.

2.1.2 Orthotropic Elastic material for the reinforcements

The material that is being used for defining the reinforcements that are to be embedded into the shear beam is an orthotropic elastic material. Orthotropic materials have three perpendicular mirror planes giving rise to orthotropic symmetry. These reinforcements are modeled to be relatively inextensible. Since the material is elastic, the orthotropic relation between strain and stress is of the form,

$$\begin{Bmatrix} \varepsilon_{11} \\ \varepsilon_{22} \\ \varepsilon_{33} \\ \gamma_{12} \\ \gamma_{13} \\ \gamma_{23} \end{Bmatrix} = \begin{bmatrix} C_{1111} & C_{1122} & C_{1133} & 0 & 0 & 0 \\ & C_{2222} & C_{2233} & 0 & 0 & 0 \\ & & C_{3333} & 0 & 0 & 0 \\ & & & C_{1212} & 0 & 0 \\ & sym & & & C_{1313} & 0 \\ & & & & & C_{2323} \end{bmatrix} \begin{Bmatrix} \sigma_{11} \\ \sigma_{22} \\ \sigma_{33} \\ \tau_{12} \\ \tau_{23} \\ \tau_{31} \end{Bmatrix}$$

The compliance matrix C, is symmetric and has nine independent compliances. The constants are directly related to conventional engineering moduli and the Material Compliance Matrix (C) can be written [13],

$$C = \begin{bmatrix} \frac{1}{E_1} & \frac{-\upsilon_{12}}{E_1} & \frac{-\upsilon_{13}}{E_1} & 0 & 0 & 0 \\ \frac{-\upsilon_{21}}{E_2} & \frac{1}{E_2} & \frac{-\upsilon_{23}}{E_2} & 0 & 0 & 0 \\ \frac{-\upsilon_{31}}{E_3} & \frac{-\upsilon_{32}}{E_3} & \frac{1}{E_3} & 0 & 0 & 0 \\ 0 & 0 & 0 & \frac{1}{G_{12}} & 0 & 0 \\ 0 & 0 & 0 & 0 & \frac{1}{G_{13}} & 0 \\ 0 & 0 & 0 & 0 & 0 & \frac{1}{G_{23}} \end{bmatrix}$$

The Poisson's ratio of an orthotropic material is different in each direction. Due to the symmetry of the compliance matrix, the Poisson's ratios are related by

$$\frac{\upsilon_{12}}{E_1} = \frac{\upsilon_{21}}{E_2}, \quad \frac{\upsilon_{23}}{E_2} = \frac{\upsilon_{32}}{E_3}, \quad \frac{\upsilon_{31}}{E_3} = \frac{\upsilon_{13}}{E_1}$$

From above relations we can see that if $E_1 > E_2$ then $\upsilon_{12} > \upsilon_{21}$. The larger Poisson's Ratio (υ_{12} in this case) is called the major Poisson Ratio's while the smaller Poisson's Ratio (υ_{21} in this case) is called minor Poisson's Ratio [12]. The inverse of the Compliance matrix (C) is the Material stiffness matrix (D) relating stress to strain [12],

$$\begin{Bmatrix} \sigma_{11} \\ \sigma_{22} \\ \sigma_{33} \\ \tau_{12} \\ \tau_{23} \\ \tau_{31} \end{Bmatrix} = \begin{bmatrix} D_{1111} & D_{1122} & D_{1133} & 0 & 0 & 0 \\ & D_{2222} & D_{2233} & 0 & 0 & 0 \\ & & D_{3333} & 0 & 0 & 0 \\ & & & D_{1212} & 0 & 0 \\ & sym & & & D_{1313} & 0 \\ & & & & & D_{2323} \end{bmatrix} \begin{Bmatrix} \varepsilon_{11} \\ \varepsilon_{22} \\ \varepsilon_{33} \\ \gamma_{12} \\ \gamma_{13} \\ \gamma_{23} \end{Bmatrix}$$

The constants in the material matrix defined in terms of Directional Moduli and Poisson's Ratios are,

$$D_{1111} = E_1(1 - \nu_{23}\nu_{32})\gamma$$
$$D_{2222} = E_2(1 - \nu_{13}\nu_{31})\gamma$$
$$D_{3333} = E_3(1 - \nu_{12}\nu_{21})\gamma$$
$$D_{1122} = E_1(1 - \nu_{23}\nu_{32})\gamma$$
$$D_{1133} = E_1(\nu_{21} + \nu_{31}\nu_{23})\gamma = E_2(\nu_{12} + \nu_{32}\nu_{13})\gamma$$
$$D_{1111} = E_1(\nu_{31} + \nu_{21}\nu_{32})\gamma = E_3(\nu_{13} + \nu_{12}\nu_{23})\gamma$$
$$D_{2233} = E_2(\nu_{32} + \nu_{12}\nu_{31})\gamma = E_3(\nu_{23} + \nu_{21}\nu_{13})\gamma$$
$$D_{1212} = G_{12}$$
$$D_{1313} = G_{13}$$
$$D_{2323} = G_{23}$$

where,

$$\xi = \frac{1}{1 - \upsilon_{12}\upsilon_{21} - \upsilon_{23}\upsilon_{32} - \upsilon_{31}\upsilon_{13} - 2\upsilon_{21}\upsilon_{32}\upsilon_{13}}$$

The numbers 1111, 2222 and 3333 specify the directions of the orthotropic materials on the reinforcements. 1111 represents the radial direction, 2222 represents the tangential direction and 3333 represents out of plane direction. The reinforcements are defined with small orthotropic moduli and are given in Table 2-4. The stiffness of the reinforcements is defined by isotropic Marlow stress-strain data for the embedded reinforcement surface combined together with the embedded orthotropic reinforcement to define non-isotropic directions. The number 1 refers to the radial direction while 2 refers to the circumferential direction, thus D1212 defines the relation between shear stress and shear strain in the 1-2 plane.

Table 2-4: Orthotropic Elastic Moduli coefficients for reinforcements

D1111	D1122	D2222	D1133	D2233	D3333	D1212	D1313	D2323
0.01	0	10	0	0	0.01	10	2	2

The density of the reinforcement material is 1.1E-10 daN.sec^2/mm^4 (1100 kg/m^3) and the thermal expansion coefficient α_{22} is 1.2E-05/^{0}C.The other components α_{11} and α_{33} are 0.

2.2 3D Tweel Mesh and Element Properties

There are different types of elements used for the finite element model which depend on the intended geometric and analysis type. In ABAQUS, every element is characterized by the family, degrees of freedom, number of nodes, formulation and integration. 3D stress elements are used for modeling the shear beam, collapsible spokes and the reinforcements. The reinforcement surface that houses the reinforcements is modeled as special surface elements in ABAQUS. The parts that have 3D stress elements are defined as 8-node linear hexahedral brick element with reduced integration and hourglass control (C3D8R) [12]. On the other hand, the reinforcement surface has elements that are 4-node and quadrilateral with reduced integration (SFM3D4R). These elements are used for Dynamic Explicit analysis only.

When static load deflection analysis is done on the Tweel, a different element type is used. They are referred to as Hybrid elements. These elements are intended primarily for use with incompressible and almost incompressible material behavior. When the material response is incompressible, the solution to a problem cannot be obtained in terms of the displacement history only, since a purely hydrostatic pressure

can be added without changing the displacements. Since hyperelasticity is associated with incompressibility, hybrid elements are used [12]. The mesh of the shear beam, collapsible spokes and the reinforcements have 8-node hybrid brick elements (C3D8H). On the other hand, the reinforcement surface has elements that are 4-node and quadrilateral without reduced integration (SFM3D4).

As already explained in the earlier sections, the ring is a structure which houses the reinforcements, reinforcement surfaces and the shear layer.

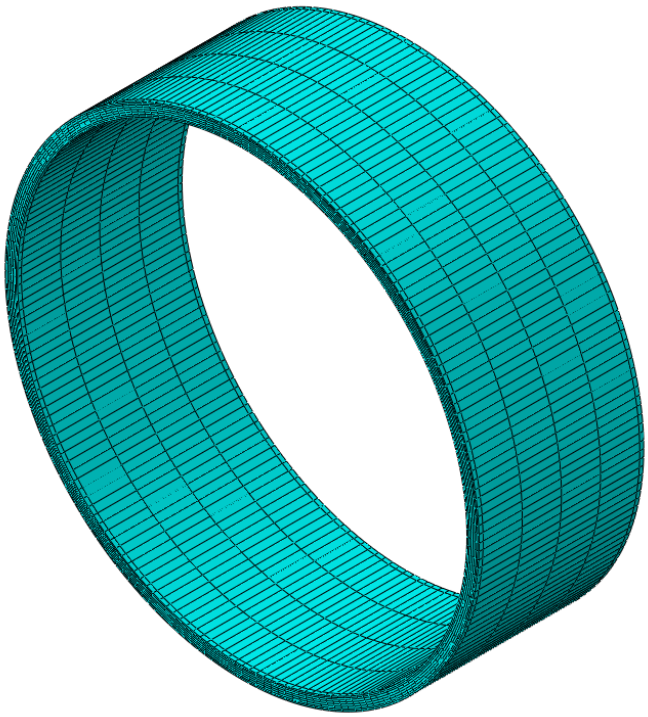

Figure 2.2: Finite element model of the ring

As shown in Figure 2.2 the finite element model of the ring is meshed such that it is discretized into 9600 elements. The ring has 8 elements along its thickness, 6 elements across the width, and 1200 elements along its circumference (3.33 elements per degree).

The thickness is defined as the difference in the distance between the outer and the inner radius. As shown in Figure 2.3, the shear layer has a total of 4 elements along its thickness and coverages have 2 elements each.

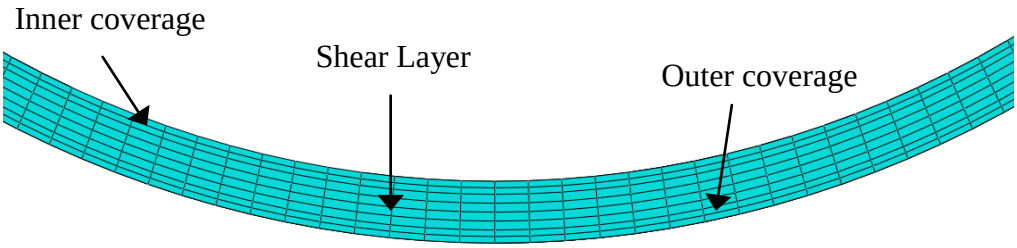

Figure 2.3: Elements along the thickness of the ring structure

The collapsible spokes of the Tweel are meshed such that a single spoke is discretized into a total of 1152 elements. It has 4 elements along its thickness, 12 elements along its width, and 24 elements along its length. Here, the thickness is defined as the distance between the two faces. The finite element model of the spoke is shown in Figure 2.4. Note that the geometry for the spoke is not planar and has a taper from the top width near the hub to the bottom width at the shear ring.

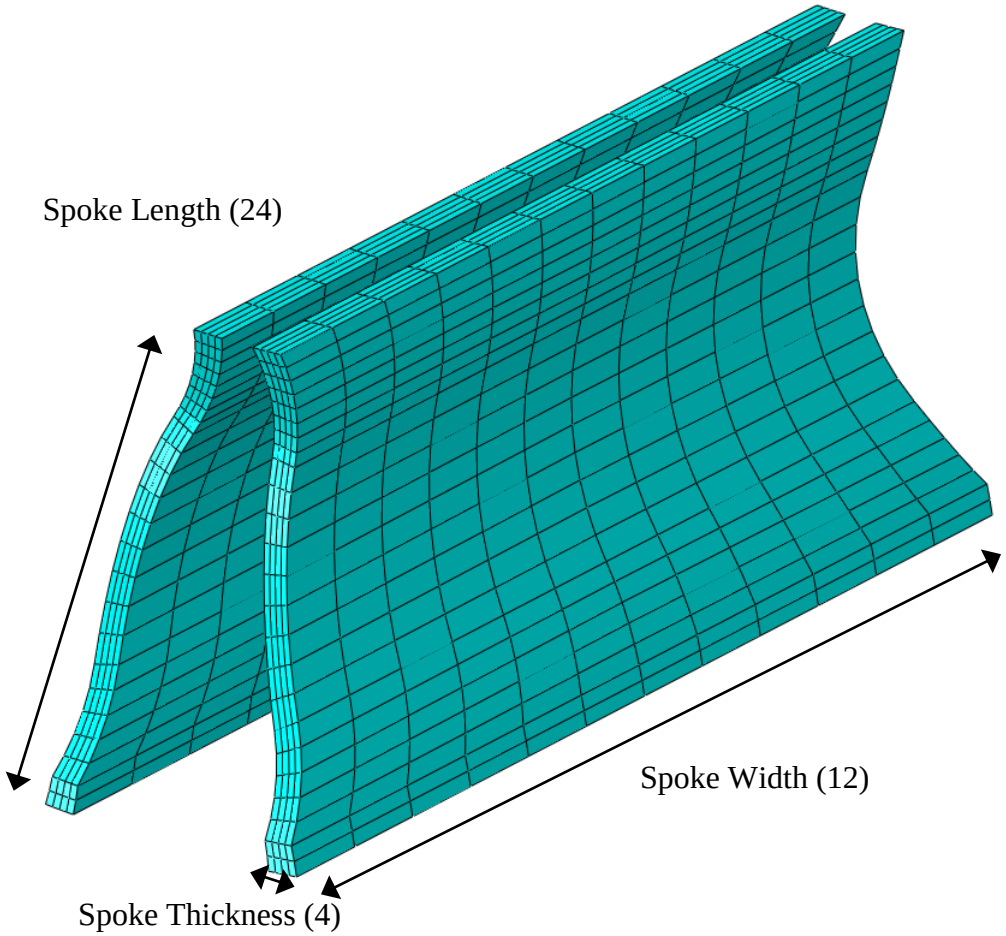

Figure 2.4: Finite element model of the 3D collapsible spoke. The number of elements across each element are given in parenthesis.

The tread model is created such that it is an assembly of two half treads. The two inner surfaces of the half treads are tied together to form an integrated tread model. The inner surface has 3 elements along its thickness and the outer surface has 1 element along the thickness. The total elements along the circumference after assembling both the half treads together are 6000. The integrated tread structure is discretized into 10400 elements.

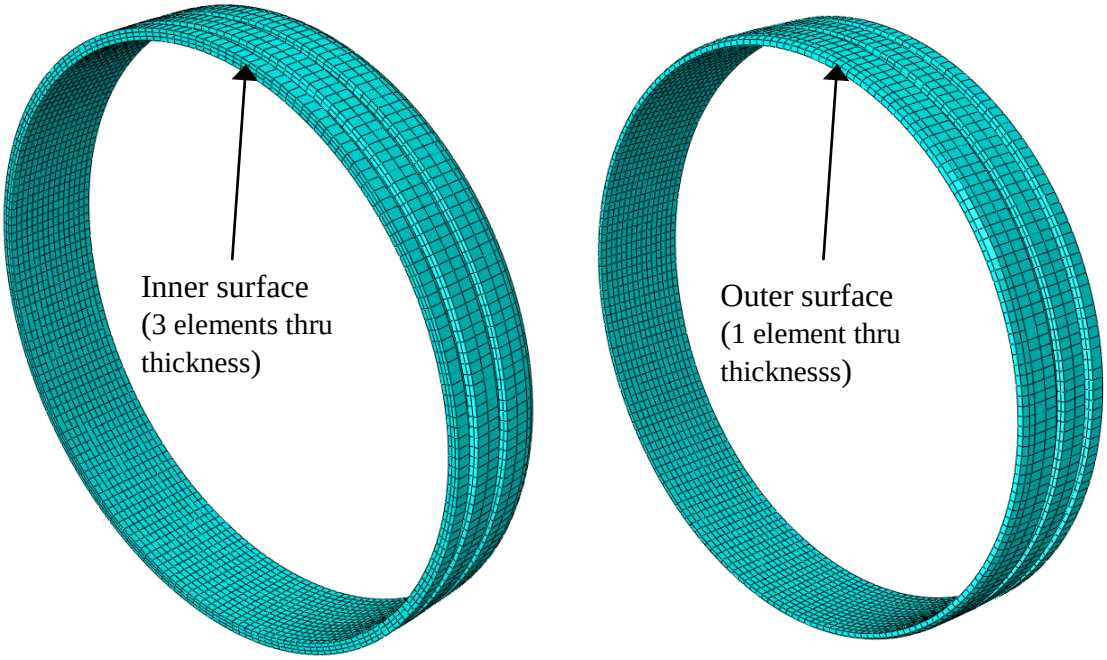

Figure 2.5: The inner and outer surfaces of the Finite Element 3D Tread model

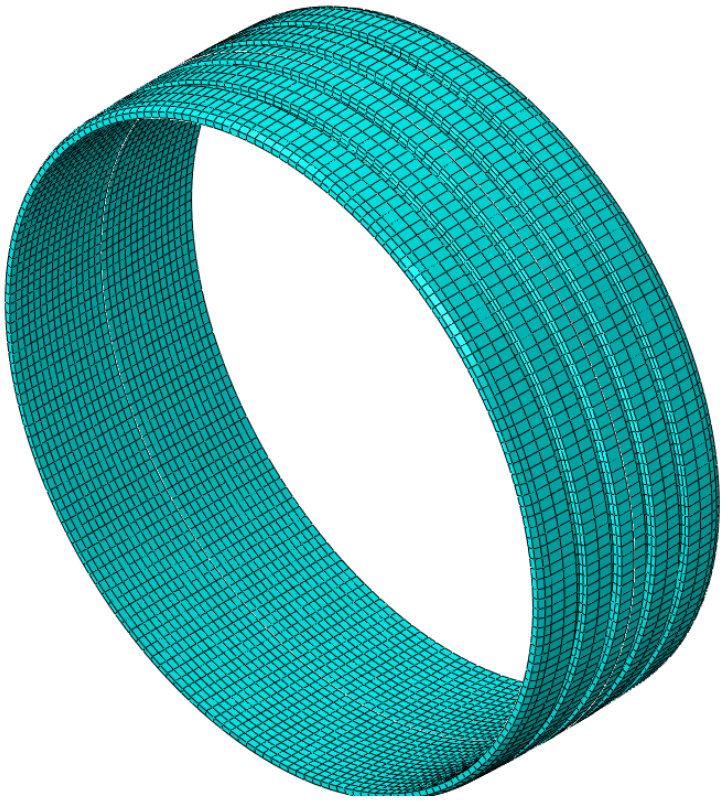

Figure 2.6: Integrated Finite element model of the 3D Tread

2.3 Interactions and Constraints

Interactions and constraints are extremely important in connecting different parts of the Tweel™ to make it an integrated structure. The different interactions and the constraints in the model are described below.

An interaction is a step dependant object, which means that they have to be defined in different steps. The interactions are active for all the steps defined. The interactions are established between the Tweel and the rigid surface using contact modeling. The type of contact that is used between the deformable tread and the rigid surface is a surface-to-surface contact [12, 17].

For the static load deflection procedure, the contact model is defined in ABAQUS/Standard. The sliding formulation between the rigid surface and the deformable tread is finite sliding. The discretization method that defines the contact model is surface-to-surface. A tangential interaction property is defined to be frictionless for the interaction between the two surfaces. In this analysis, the Tweel is not subjected to rolling and hence, to establish contact, it is not mandatory to select the entire tread surface.

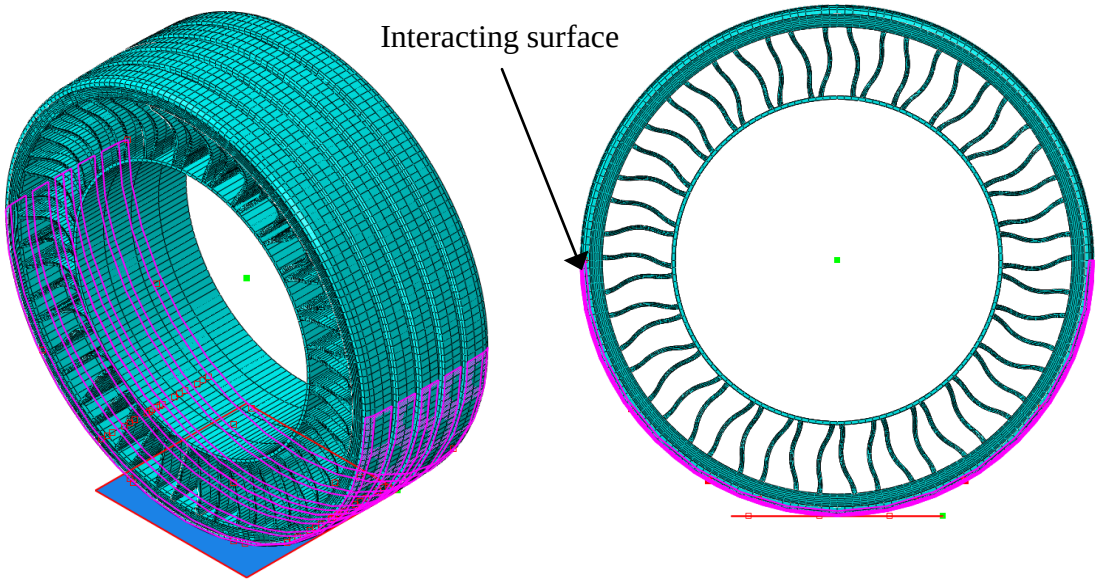

Figure 2.7: Surface-to-surface interaction established between the tread surface and the rigid ground

For the dynamic rolling analysis, the contact model is defined in ABAQUS / Explicit. The mechanical constraint formulation between the rigid surface and the deformable tread is defined by penalty contact method. The sliding formulation is finite sliding. The tangential interaction property is defined as a penalty contact method with a friction coefficient value of 1. In both static general and dynamic explicit, a normal

interaction property is defined such that the pressure over closure is “Hard” contact. Also, the contacting surfaces are allowed to separate during the analysis.

In a dynamic explicit analysis, the surfaces have to be continuous for an interaction to be established. Since the tread is divided into 6 grooves, the outer tread surface is no longer continuous. Hence 6 different interactions have been created. Also, since the Tweel is subjected to rolling in this analysis, the entire tread surface is selected.

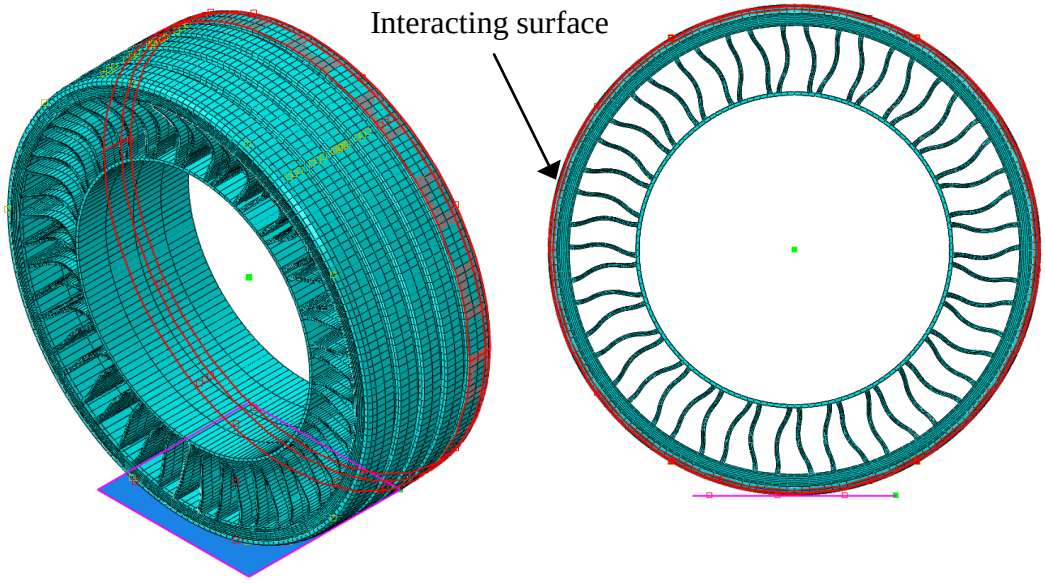

Figure 2.8: Surface-to-surface contact established between the tread surfaces and rigid ground.

The constraints used in the model to form an integrated Tweel are Tie, Coupling and Embedded Regions. They are described below.

2.3.1 Constraint - Embedded Region

An embedded region constraint allows one to embed a region of the model within another region of the model or within the whole model. Embedded region constraint is based on the embedded element technique. These elements are assembled within the "host" structure whose response will be used to constrain the translational degrees of freedom of the nodes of the embedded elements [12]. This constraint is used to embed the reinforcements and reinforcement surfaces into the ring, which is the host structure. These in-extensible membranes are assembled such that the shear layer lies between the two reinforcements. The reinforcement surfaces are assembled above the reinforcements.

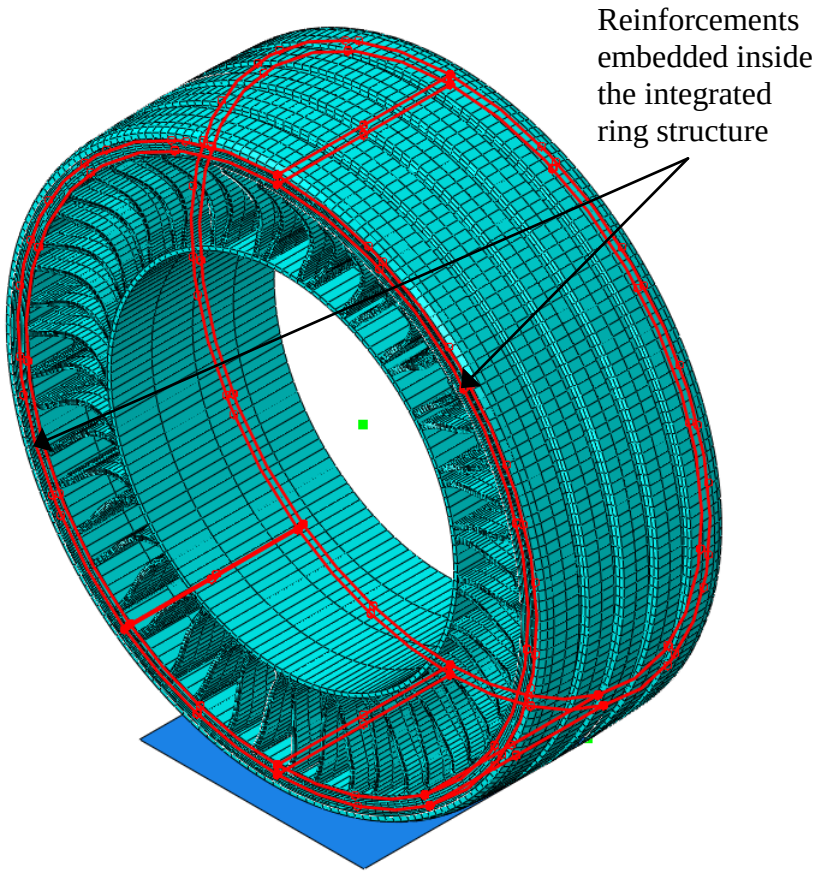

Figure 2.9: Embedded region constraints established to embed the reinforcements and reinforcement surfaces into the integrated structure of the ring

2.3.2 Constraint - Coupling

A surface based coupling constraint couples the motion of a collection of nodes on a surface to the motion of a reference node. The constraint can be applied to user-specified degrees of freedom at the coupling nodes with respect to the global or a local coordinate system. When the group of nodes is coupled to the rigid body motion by the reference node, the type of coupling is kinematic. On the other hand, when the group of nodes can be constrained to the rigid body motion defined by a reference node in an

average sense by allowing control over the transmission of forces through weight factors specified at the coupling nodes, the type of coupling is distributive [12]. In the Tweel, a kinematic coupling constraint is defined such that the inner surface of rigid hub is coupled to a reference node which is referred to as the hub center.

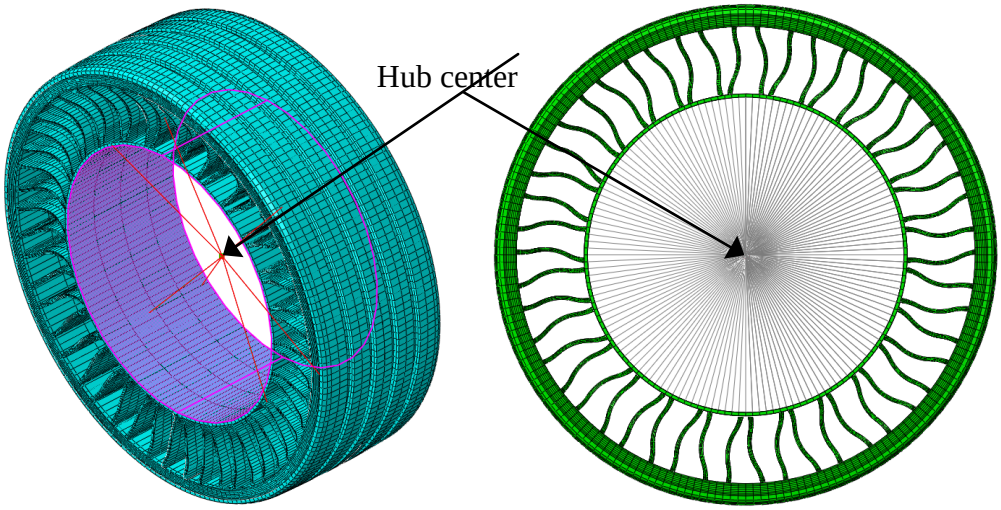

Figure 2.10: Coupling constraint used to connect the inner surface of the rigid hub to the hub center (reference point)

2.3.3 Constraint - Tie

A surface-based tie constraint ties two surfaces together for the duration of a simulation. It constrains each of the nodes on the slave surface to have the same motion and the same value of temperature, pore pressure, acoustic pressure, or electrical potential as the point on the master surface to which it is closest [12]. In other words, it eliminates the degrees of freedom of the slave surface nodes that are constrained, where possible. The relative stiffness of the surfaces that are being tied help in determining the master

and the slave surface. The stiffer surface is considered to be the master surface. In the Tweel™ model, four tie constraints have been used:

1) Outer surface of the rigid hub and the interacting spoke surfaces,

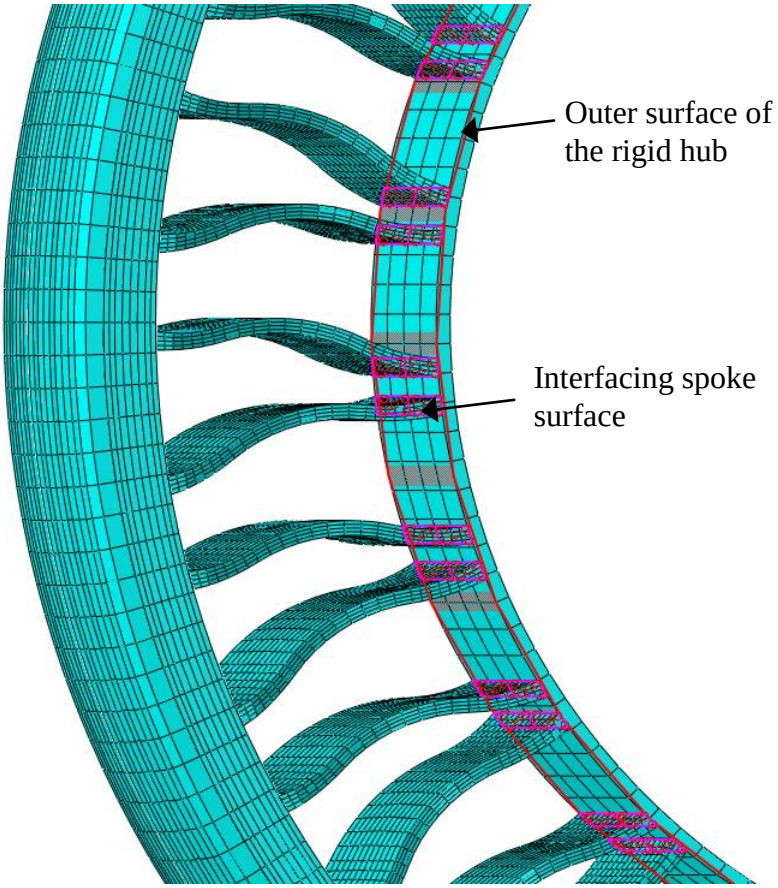

Figure 2.11: Tie constraint to tie the outer surface of the rigid hub and the interfacing spoke surfaces

This constraint links the rigid hub and the spokes. The outer surface of the rigid hub is chosen as the master surface while the interfacing surfaces are chosen as slave surfaces.

2) Outer surface of the inner coverage with the interacting spoke surfaces,

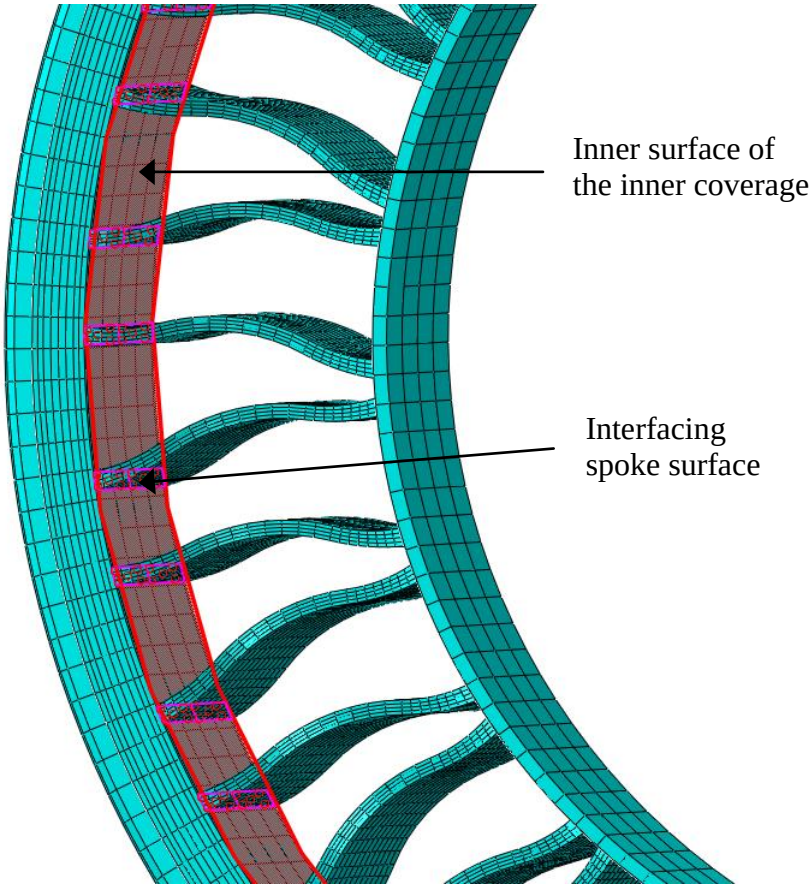

Figure 2.12: Tie constraint to tie the interfacing spoke surfaces and the inner surface of the inner coverage of the ring

This constraint is used for linking the rigid hub to the integrated ring structure. The inner surface of the outer coverage is chosen as the master surface and the interfacing spoke surfaces are chosen as slave surfaces.

3) Outer surface of the outer coverage and Tread

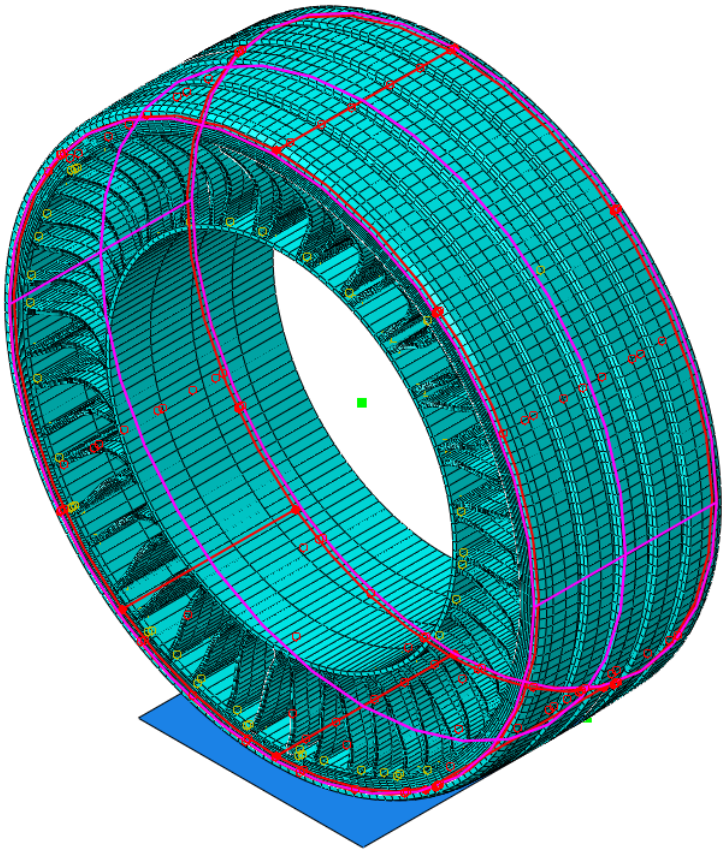

Figure 2.13: Tie constraint to tie the outer surface of the outer coverage and the tread

This constraint links the integrated ring structure and the deformable tread. The outer surface of the outer coverage is selected as the master surface and the inner surface of the tread is selected as the slave surface.

4) Both half tread models

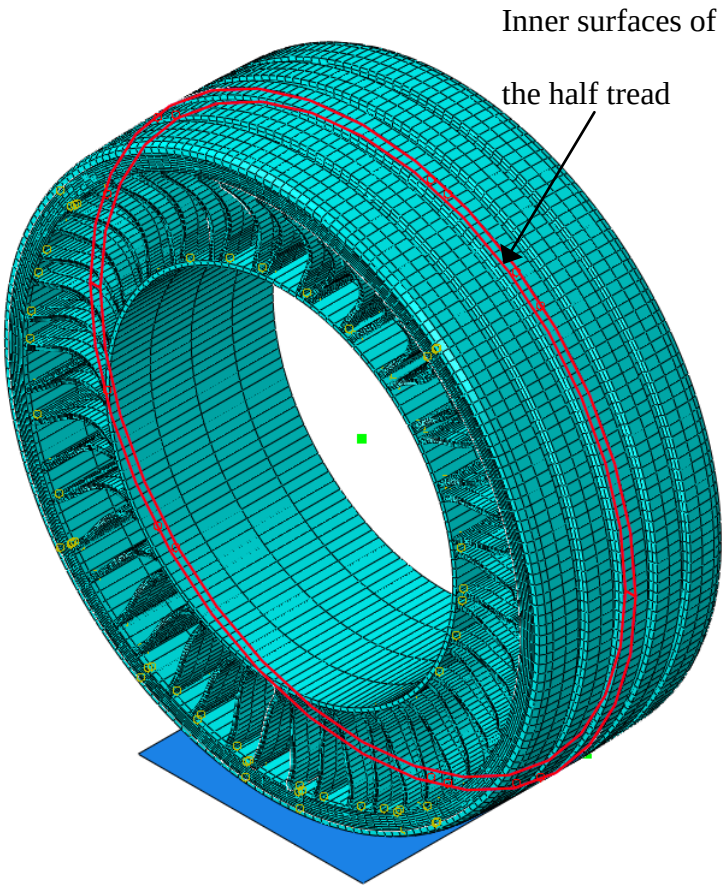

Figure 2.14: Tie constraint to tie the two inner surfaces of the half treads

This constraint is used to tie the two half treads together to form an integrated tread structure. Both the inner surfaces of the half treads are selected and are tied.

2.4 3D Tweel Analysis procedures and boundary conditions on the Tweel™

The different types of analysis procedures are listed below,

- *Procedure 1* (P1): Static Load Deflection Analysis using ABAQUS Standard.
- *Procedure 2* (P3): High speed steady state rolling on a flat ground with friction using ABAQUS Explicit
- *Procedure 3* (P4)*:* Rolling over an obstacle using ABAQUS Explicit.

2.4.1 Static Load Deflection

This computational procedure for the TWEEL model is divided into two steps.

1. *Predefined field*: Temperature of the model is set to 125 ^{0}C
2. *Step 0*: Initial Condition: Temperature is 125 ^{0}C.
3. *Step 1*: Cooling: A 50 ^{0}C temperature change is brought about over a time period of 0.1 seconds.
4. *Step 2*: Loading: Temperature is maintained at 75 ^{0}C and a load of 366.5 daN (824 lb) is applied at the hub center over a time period of 0.1 seconds. This weight corresponds to the quarter weight of the vehicle.

This procedure is executed in ABAQUS Standard and is used to find out the corresponding displacement of the model in the vertical direction when a vertical force is applied at the hub center. This procedure is described below in further detail.

In Step 1, the Tweel is at an initial temperature of 125 ^{0}C and the model is completely stationary. The temperature is reduced by 50^{0}C to model the molding process in manufacturing so that the Tweel develops pre-stress due to thermal strains. The ring contracts when the Tweel is cooled from 125 ^{0}C to 75 ^{0}C. As a result, the Tweel tends to lose contact with the ground. An adjustment has been made to avoid loss of contact during this step. The ground is tied to the tread of the Tweel and is allowed to move freely in the vertical direction during cooling. When step 2 commences, the temperature is maintained at 75 ^{0}C and a vertical load of 366.5 daN is applied at the hub center. The ground is completely constrained when the load is being applied. Due to the application of load, the Tweel is compressed against the ground and hence the displacement of the

hub center in the vertical direction is obtained. This is referred to as the “deflection” of the Tweel upon the action of a “load”.

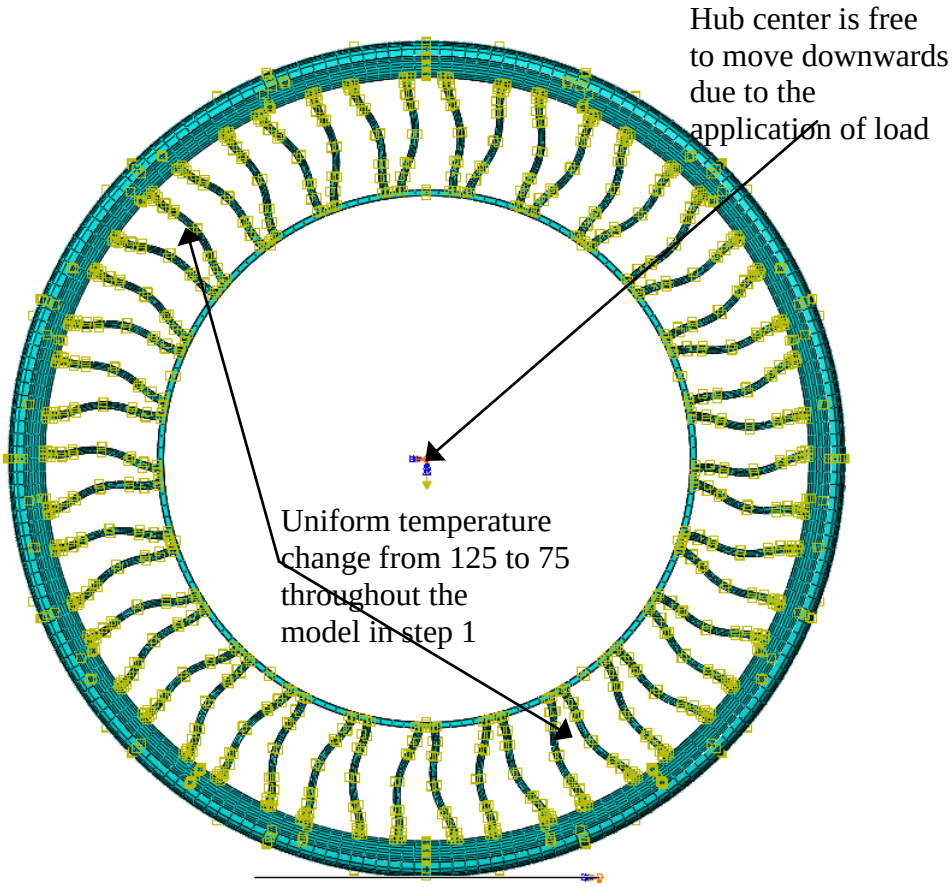

Figure 2.15: Boundary conditions imposed on the Tweel during static load deflection procedure

2.4.2 High speed steady state rolling on a flat ground with friction

This procedure is divided into three steps.

1. *Predefined field*: Temperature of the model is set to 125 ^{0}C
2. *Step 0*: Temperature is 125^{0}C. The ground and the hub center are fixed.
3. *Step 1*: Loading, Acceleration and Cooling: Temperature is reduced to 75^{0}C. A load of 366.5 daN is applied. Hub center is free to move in the vertical direction

and is also free to rotate. Tweel is accelerated with a horizontal velocity of 27.7778 m/s (approximately 100 km/hr) in the negative x-direction. Time period of this step is 1 second.

4. *Step 2*: Rolling: Temperature, Load and Horizontal velocity are maintained and propagated from the previous step. Time period of this step is 0.3 seconds.

In this procedure, a situation where a vehicle attains steady state from rest is simulated. A predefined field is created which sets the temperature of the Tweel to 125^0C. Initial conditions are such that both the Tweel and the ground have all the DOFs constrained. Step 1 is a combination of three different phases, viz. loading, cooling and accelerating. In loading, a vertical load is applied at the hub center such that compression of the Tweel is enforced. A load of 366.5 daN is smoothly applied over a time period of 1 second. At the same time, the temperature of the model is reduced smoothly from 125^0C to 75^0C. In addition to cooling and loading, another phase also takes place called acceleration. A horizontal velocity of 27.7778 m/sec (100 km/hr) is applied smoothly at the hub center in the negative x-direction. This phase ensures that the Tweel gains enough momentum to steadily roll. The different phases occur simultaneously to save computational time. In step 2, temperature is maintained at 75^0C, axial hub velocity is maintained at 27.7778 m/sec and the load is maintained at 366.5 daN. The Tweel is forced to roll at constant speed (acceleration is zero) on the ground over a time period of 0.3 seconds.

2.4.3 Rolling over an obstacle

This procedure is divided into three steps.

Predefined field: Temperature of the model is set to 125 ^{0}C

1. *Step 0*: Temperature is 125^{0}C. The ground and the hub center are fixed.
2. *Step 1*: Loading, Acceleration and Cooling: Temperature is reduced to 75^{0}C. A load of 366.5 daN is applied. Hub center is free to move in the vertical direction and is also free to rotate. Tweel is accelerated with a horizontal velocity of 3m/s. Time period of this step is 1 second.
3. *Step 2*: Intermediate: Temperature, Load and Horizontal velocity are maintained are maintained a constant from the previous step. Time period of this step is 0.1 seconds.
4. *Step 3*: Free Rolling: Temperature is maintained at the same value from the previous step. The horizontal velocity is no longer maintained at 3 m/s (10.8 km/hr). No boundary condition is enforced at the hub center

In this procedure, a situation where a vehicle attains steady state from rest is simulated. A predefined field is created which sets the temperature of the Tweel to 125^{0}C. Initial conditions are such that both the Tweel and the ground have all the DOFs constrained. Step 1 is a combination of three different analyses, viz. loading, cooling and accelerating. In loading, a vertical load is applied at the hub center such that compression of the Tweel is enforced. A load of 366.5 daN (824 lb) is smoothly applied over a time period of 1 second. At the same time, the temperature of the model is reduced smoothly from 125^{0}C to 75^{0}C. In addition to cooling and loading, another phase also takes place called acceleration. A horizontal velocity of 3 m/second is applied smoothly at the hub center. This phase ensures that the Tweel gains enough momentum to steadily roll. The

different phases occur simultaneously to save computational time. In step 2, temperature is maintained at 75^0C, axial hub velocity is maintained at 3m/sec and the load is maintained at 366.5 daN. The Tweel is forced to roll at constant speed (acceleration is zero) on the ground over a time period of 0.1 seconds. In Step 3, all the other conditions remain the same from the previous step except for the axial velocity which is made inactive. This can be related to a situation where the driver of the vehicle takes his/her foot off the accelerator. Once the acceleration is not provided, the Tweel travels due to the momentum generated in the previous step.

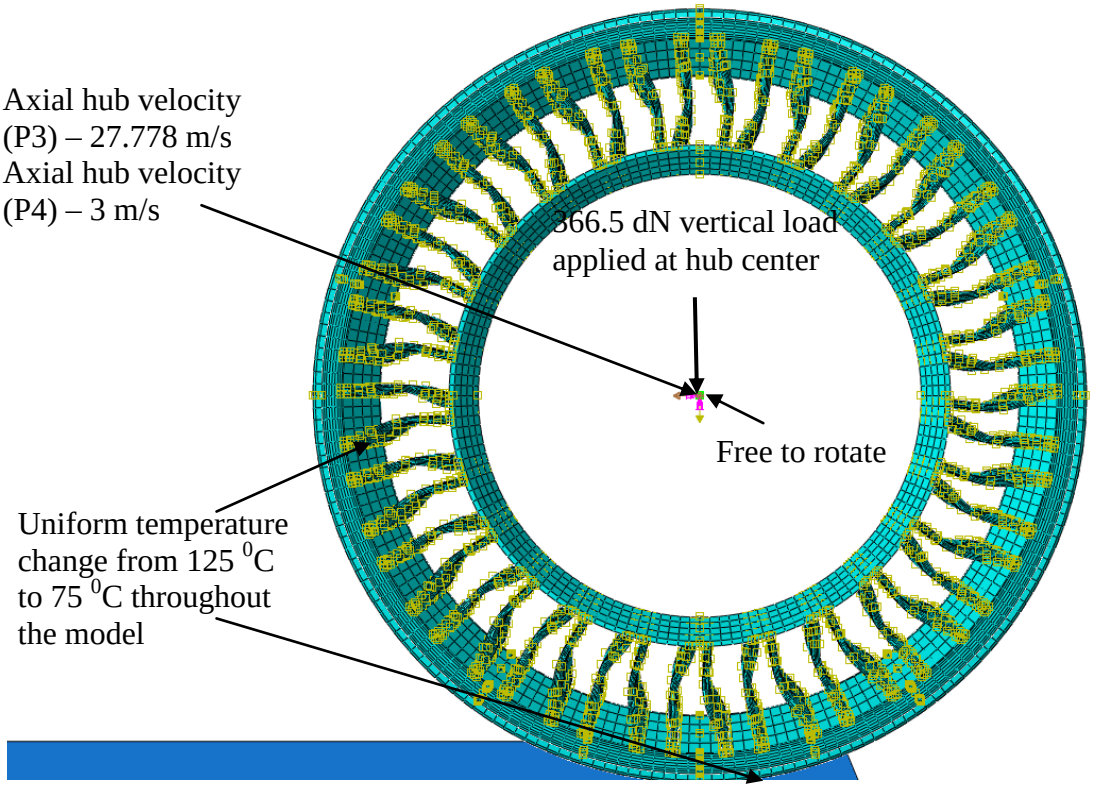

Figure 2.16: Boundary conditions imposed on the Tweel during loading, accelerating and cooling (step 1) in procedures 2 and 3

CHAPTER THREE – EFFECTS OF CHANGING MATERIAL MODELS ON STRESS-STRAIN CURVES

There are many factors that may affect the noise level and/or vibrations of the TWEEL. They may be classified as Geometric, Material and other factors. Geometric factors include spoke curvature; spoke thickness, ring dimensions and number of shear ring reinforcements. Material factors may include the stiffness characteristics, mass, damping, and nonlinear material models used for the spoke, ring, reinforcements and tire tread. In this chapter, a detailed explanation of the different material models used for the spokes, ring and reinforcements are given. Also, the stress-strain curves for the different material models are analyzed and compared.

3.1 Material models

The reference Tweel model uses a hyperelastic Marlow material model for the ring and the spokes. The properties for this material model have been obtained from the uni-axial test data for polyurethane (PU). In addition, two material models have been selected to study the effects of changing material stiffness. They are,

1) Mooney Rivlin

This material model has been derived from the general polynomial strain energy potential form. The polynomial strain energy potential is given below,

$$U = \sum_{i+j=1}^{N} C_{ij}(\bar{I}_1 - 3)^i(\bar{I}_2 - 3)^j + \sum_{i=1}^{N} \frac{1}{D_i}(J_{el} - 1)^{2i}$$

The terms in this energy potential model have been explained in detail in Chapter 2. The Mooney Rivlin material model is derived from the polynomial strain energy potential by setting N=1. On expanding, the Mooney Rivlin material model is,

$$U = C_{10}(\bar{I}_1 - 3) + C_{01}(\bar{I}_2 - 3) + \frac{1}{D_1}(J_{el} - 1)^2$$

The strain energy potential is divided into a deviatoric and a hydrostatic component. The deviatoric component controls distortion is defined by the shear modulus of the material model, while the hydrostatic component controls volumetric changes, and is defined by the bulk modulus of the material model. The shear modulus is given as,

$$\mu_0 = 2(C_{10} + C_{01})$$

while the bulk modulus is given as,

$$K_0 = \frac{2}{D_1}$$

2) Neo Hookean

A reduced polynomial form can be obtained from the above equations established for the Polynomial form by setting all C_{ij}=0 for j≠0. This model is as shown below,

$$U = \sum_{i=1}^{N} C_{i0}(\bar{I}_1 - 3)^i + \sum_{i=1}^{N} \frac{1}{D_i}(J_{el} - 1)^{2i}$$

The Neo-Hookean material model is a particular case of the reduced polynomial form. It is obtained by setting N=1. It is as shown below.

$$U = C_{10}(\bar{I}_1 - 3) + \frac{1}{D_1}(J_{el} - 1)^2$$

Similar to the Mooney Rivlin, the hydrostatic component of the material model is governed by the coefficient $C_{10.}$ The shear modulus for the material is given as,

$$\mu_0 = 2(C_{10})$$

The bulk modulus is given as,

$$K_0 = \frac{2}{D_1}$$

Given the experimental test data, the material constants can be determined through a nonlinear least squares fit procedure, which minimizes the relative error in stress. For n nominal stress-nominal strain data pairs, the relative error E can be minimized,

$$E = \sum_{i=1}^{n} (1 - T_i^{th} / T_i^{test})^2$$

where, T_i^{test} are the stress values from the test data and T_i^{th} are nominal stress expressions which are different for different material models. For the Mooney-Rivlin model,

$$T_k^{th} = \sum_{i+j=1}^{N} C_{ij} X_{ij}(\lambda_k),\ k = 1 \ldots n,$$

The nominal stress expression for a Mooney-Rivlin model is obtained by setting N=1 in the above equation. For the Neo-Hookean model,

$$T_k^{th} = \sum_{i=1}^{N} C_{i0} X_i(\lambda_k), \quad k = 1 \ldots n,$$

In the above equations, the X (λ) are functions that depend on the stress state (uniaxial, biaxial or planar). Since the Mooney-Rivlin material model includes higher-order polynomials in deviatoric stretch, it gives a better least square curve fit to the experimental test data when compared to the Neo-Hookean material model.

3.2 Material study for the ring and the spokes

As discussed earlier in Chapter 2, the Poisson's ratio depends on the shear modulus and the bulk modulus of the material model considered. It is defined as,

$$\nu = \frac{3(K_0/\mu_0) - 2}{6(K_0/\mu_0) + 2}$$

Using this relation, numerous material models can be derived for the required Poisson's ratio and/or the ratio between initial shear and bulk modulus. Hence, it can be concluded that the Poisson's ratio remains the same if the ratio between the bulk modulus and the shear modulus remains the same.

When defining the Marlow properties for the ring and the spoke, in addition to the uni-axial test data, the Poisson's ratio for the material has to be defined. The Poisson's ratio for the Marlow strain energy potential is defined as 0.45, modeling the nearly

incompressible nature of polyurethane (PU). To study the effect of changing material models for the ring and the spokes of the Tweel, different material models are generated with the same Poisson's ratio of 0.45. From the above equation, the ratio of the bulk modulus and the shear modulus is defined as,

$$\frac{K_0}{\mu_0} = \frac{2(1+\nu)}{3(1-2\nu)}$$

From this equation, the ratio of the initial bulk modulus to the initial shear modulus is 29/3. In this material study, Mooney Rivlin and Neo Hookean material models are fit to the Marlow strain energy potential. The Mooney Rivlin and Neo Hookean models allow us to change the material behavior by a defined amount by changing the coefficients in the model. Three levels are defined for every material thereby making it a total of 6 materials in addition to the Marlow strain energy potential. The first level is when the shear modulus of the material remains unchanged. The second level is when the shear modulus of the material is reduced by 25%. Finally the third level is when the shear modulus is increased by 25%. For each of these models, the bulk modulus is adjusted in order to keep the same Poisson's ratio as the reference Marlow model.

For the Mooney Rivlin material model, the ratio of the initial bulk modulus and the initial shear modulus is defined as,

$$\frac{K_0}{\mu_0} = \frac{1}{D_1(C_{10} + C_{01})}$$

As explained before, the shear modulus depends on the coefficients C_{10} and C_{01}. To maintain a constant Poisson's ratio of 0.45, the ratio of the initial bulk modulus and the initial shear modulus have to be 9.666666667. When the coefficients C_{10} and C_{01} are reduced by 25% such that the shear modulus is reduced by 25%, to keep the ratio K_0/μ_0 fixed, the bulk modulus must be reduced by 25% as well. Since K_0 is inversely proportional to D_1, to keep the ratio K_0/μ_0 fixed (and thus ν fixed) of a 33% increase is made to the existing value of D_1, as shown below

$$\frac{K_0}{\mu_0} = \frac{1}{(\frac{4}{3}D_1)(\frac{3}{4}C_{10} + \frac{3}{4}C_{01})}$$

On the other hand, when the shear modulus is increased by 25%, the bulk modulus is increased by 25% as well. The coefficient D_1 is decreased by 20% to maintain a fixed ratio K_0/μ_0 fixed (and thus ν fixed). This is as shown below.

$$\frac{K_0}{\mu_0} = \frac{1}{(\frac{4}{5}D_1)(\frac{5}{4}C_{10} + \frac{5}{4}C_{01})}$$

In the above equations, when the coefficient C_{01} is made zero, the ratio is defined for a Neo Hookean strain energy potential model.

The coefficients of the different material models considered with 25% increase and decrease in modulus are given in Table 3-1. Since the ratio of K_0/μ_0 is fixed, Poisson's ratio remains a constant value for all models. Using Abaqus, a least squares fit

of the Marlow data is used to determine the unchanged coefficients (denoted as 0%) in the Mooney-Rivlin and Neo-Hookean models.

Table 3-1: Hyperelastic Material Coefficients used in the material study for the ring and spokes. Units for moduli are dN/mm2. Fixed Poisson's ratio ν = 0.45, K0/μ0=9.6667

Material		D_1	C_{10}	C_{01}	Shear Modulus μ_0	Bulk Modulus K_0
Mooney-Rivlin	+25%	.099552403	-.968195876	2.00732976	2.078267768	20.08992189
	0%	.124440504	-.774556701	1.60586381	1.662614218	16.07193748
	-25%	.165920257	-.580917525	1.20439786	1.24696067	12.05398326
Neo-Hookean	+25%	.168449137	.614121730	0	1.22824346	11.87302016
	0%	.210561422	.491297384	0	.982594768	9.498416096
	-25%	.280748562	.368473038	0	.736946076	7.123812089

3.3 Comparison of nominal stress – nominal strain curves

The nominal stress – nominal strain curves for the different Hyperelastic material models are obtained by evaluating the coefficients using ABAQUS. The following set of nominal stress – nominal strain curves are provided for all the material models. The range of the nominal values of strain is from -0.2 to +0.2. The strains are plotted on the X-axis and their corresponding nominal stress values are plotted on the Y-axis.

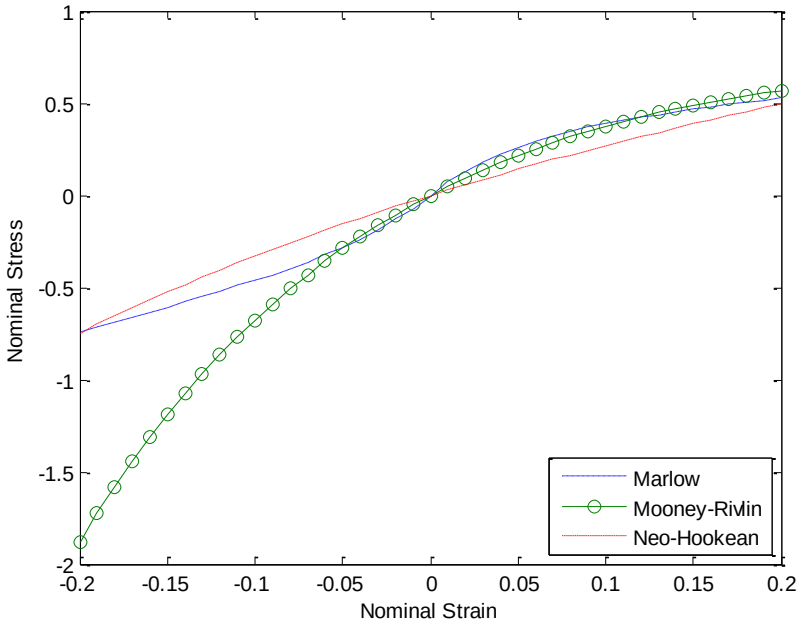

Figure 3.1: Comparison of the nominal stress – nominal strain curves for the Marlow, Mooney Rivlin and Neo Hookean strain energy potential models fitted to the Marlow data.

In Figure 3.1, the nominal stress – nominal strain curves for the Marlow, and fitted Mooney Rivlin and Neo Hookean material model are compared. The nominal stress and the nominal strain values for the Marlow model are available in the form of a uni-axial test data. The Mooney Rivlin and the Neo Hookean material models approximate the behavior of the Marlow strain energy potential using a least-squares fit as described earlier. For tensile stresses and strains, the Mooney Rivlin unchanged model fits the Marlow curve more accurately than the simpler Neo Hookean unchanged model. However, for large compressive stresses with strains less than -0.1, the Mooney-Rivlin unchanged model diverges significantly from the Marlow curve. The simple Neo-Hookean unchanged model is able to fit the Marlow curve better for compression, but is less accurate in tension. After evaluation of the uniaxial test data, it was seen that the

Mooney-Rivlin model was unstable for normal strains greater than 0.47 and less than -0.3056; these are extremely large strain magnitudes and are not expected to occur for Tweel operating within design limits. The Neo-Hookean model was stable for all strains.

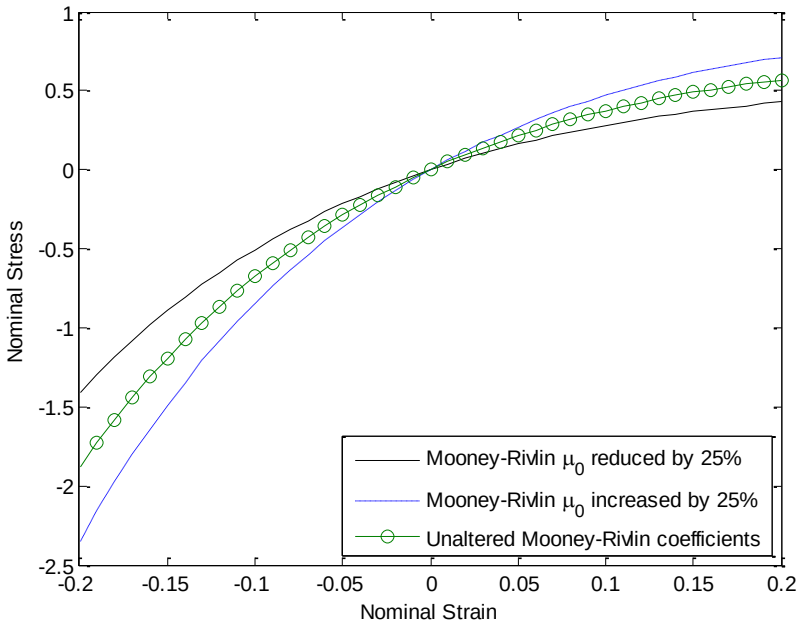

Figure 3.2: Comparison of nominal stress – nominal strain curves of the original fitted, reduced and increased modulus Mooney Rivlin material models.

Figure 3.2, the nominal stress – nominal strain curves for the different Mooney Rivlin material models are plotted against each other and compared. When the shear modulus of the Mooney Rivlin unchanged model is reduced by 25%, the tangent slope of the reduced model is smaller than that of the original fitted Mooney Rivlin model. Similarly, the tangent slope of the increased model is larger than that of the unchanged model.

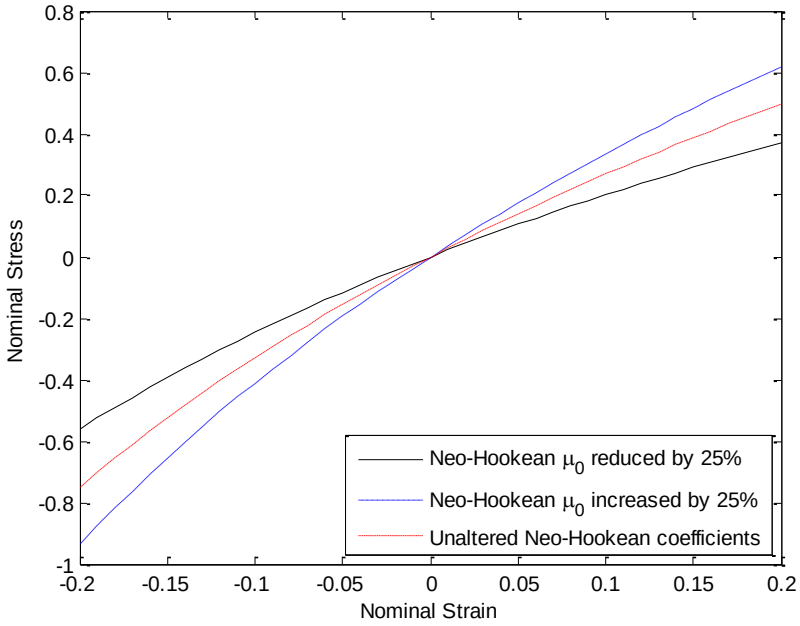

Figure 3.3: Comparison of nominal stress – nominal strain curves of the original fitted, reduced and increased modulus Mooney Rivlin material models.

In Figure 4.4 the nominal stress – nominal strain curves for the different Neo Hookean material models are plotted against each other and compared. When the shear modulus of the Neo Hookean unchanged model is reduced by 25%, the tangent slope of the reduced model is smaller than that of the unchanged model. Similarly, the tangent slope of the increased model is larger than that of the unchanged model.

As already explained, the shear modulus can be related directly to the stiffness of the material model. Based on the results, it can be concluded that the higher the shear modulus, the more the stiffness of the material model and vice versa.

CHAPTER FOUR – EFFECTS OF CHANGING MATERIAL PROPERTIES ON STATIC LOAD DEFLECTION OF 3D TWEEL™

4.1 Procedure

The Static Load Deflection procedure determines the displacement of the hub center upon the application of load. This can also be related to the compression of the Tweel upon load. Static Load Deflection also helps in determining the stiffness of the Tweel.

Using the load deflection procedure described in Section 2.4.1, Figure 4.1 shows the deformed Tweel model at the end of loading. Due to the application of load, the spokes present in the contact region experience compression and undergo buckling.

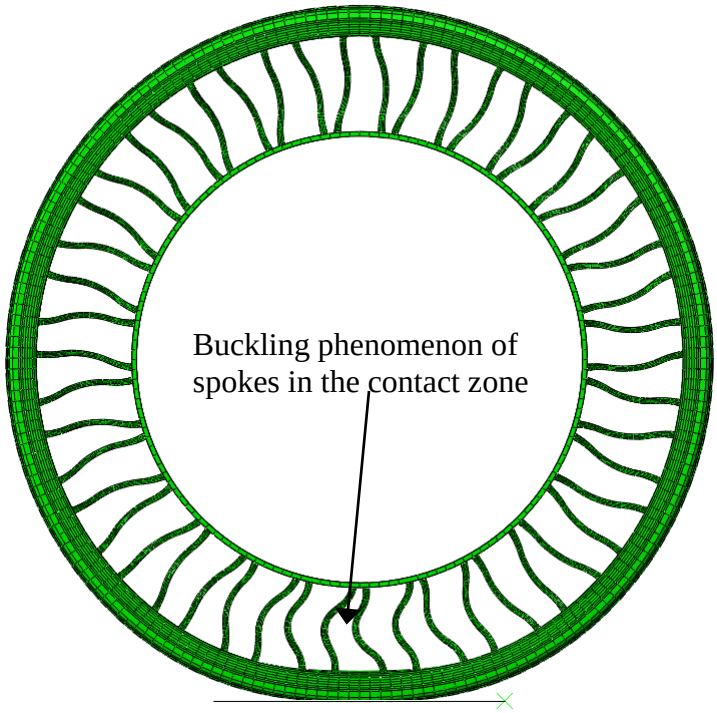

Figure 4.1: Fully compressed Tweel upon the action of applied load at the hub center

4.2 Comparison of Static Load Deflection curves

In the following static load-deflection curves are generated for the Tweel models with different material properties. In the first section, the material properties and of the different Hyperelastic models for the polyurethane in the ring are changed while keeping the Marlow model for the polyurethane in the spokes unchanged. In the second study, the material properties of the polyurethane spoke are changed while keeping the original Marlow model for polyurethane in the ring unchanged. The load-deflection curves were obtained by combining the vertical reaction force exerted on the wheel with respect to time and the corresponding vertical displacement with respect to time. Ask discussed earlier, for each model studied, the ratio of initial bulk modulus to shear modulus is kept constant. The values on the Y-axis correspond to the reaction force in deca Newton (dN) on the TWEEL and the corresponding vertical displacement values in millimeter (mm) are plotted on the X-axis.

4.2.1 Change in ring material properties

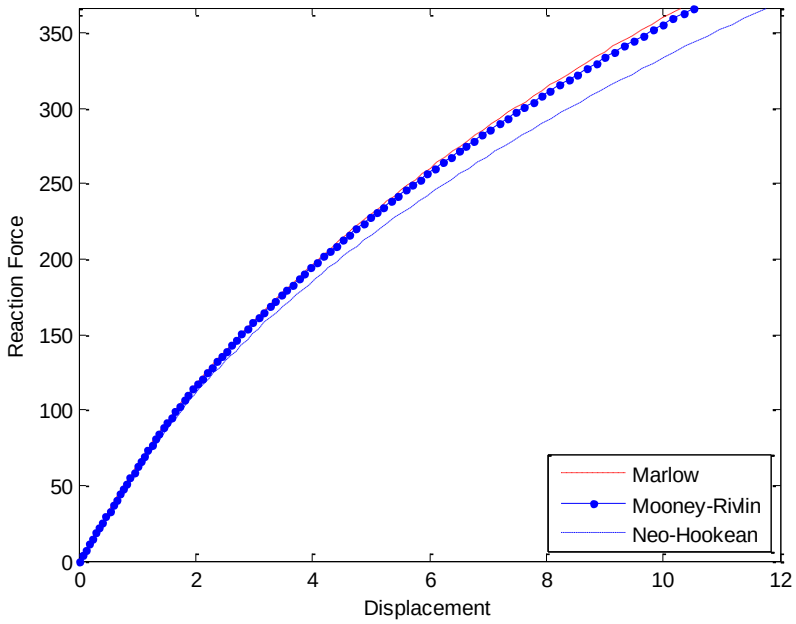

Figure 4.2: Comparison of load deflection curves for Marlow, and fitted Mooney Rivlin and Neo Hookean material models for the ring. Properties for the spokes are not changed.

Figure 4-2 shows the load deflection curves for changes in ring material model from the original Marlow properties obtained from uni-axial stress-strain data and Mooney-Rivlin and Neo-Hookean models obtained by least-squares fit of this data. The load deflection plots for Marlow and the Mooney-Rivlin are almost the same. In other words, the tangent slopes are almost the same for both the curves whereas, the Neo-Hookean has a slope lesser than the other two curves. An increase in tangent slope indicates increased stiffness while a decrease in slope indicates decreased stiffness.

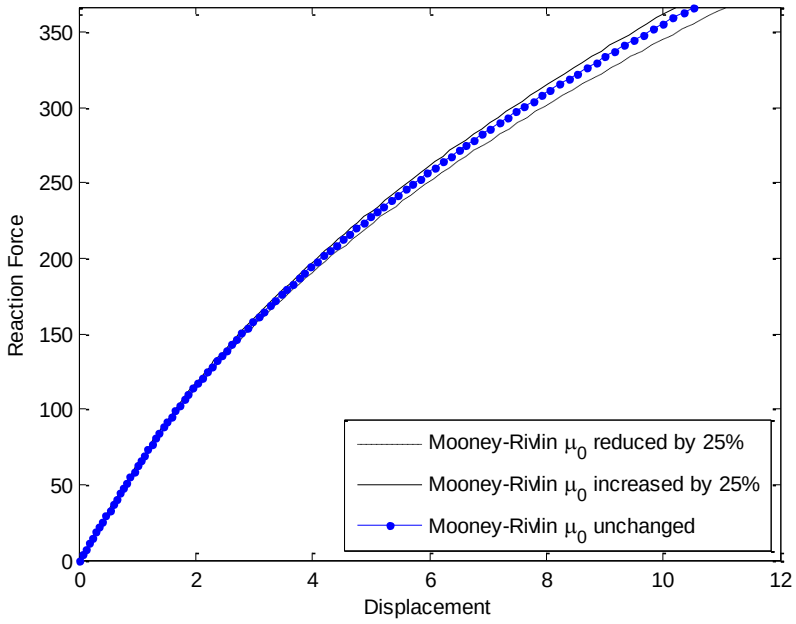

Figure 4.3: Comparison of load deflection curves for different Mooney Rivlin models for the ring. Properties for spoke are not changed.

Figure 4.3and Figure 4.4 show the load deflection curves for cases when the initial shear modulus for the Mooney-Rivlin and Neo-Hookean models is changed by plus/minus 25%. It is seen that as the shear modulus is increased, the tangent slope increases as well. Since the vertical stiffness can be correlated with the tangent slope, it is concluded that the vertical stiffness is directly proportional to the shear modulus.

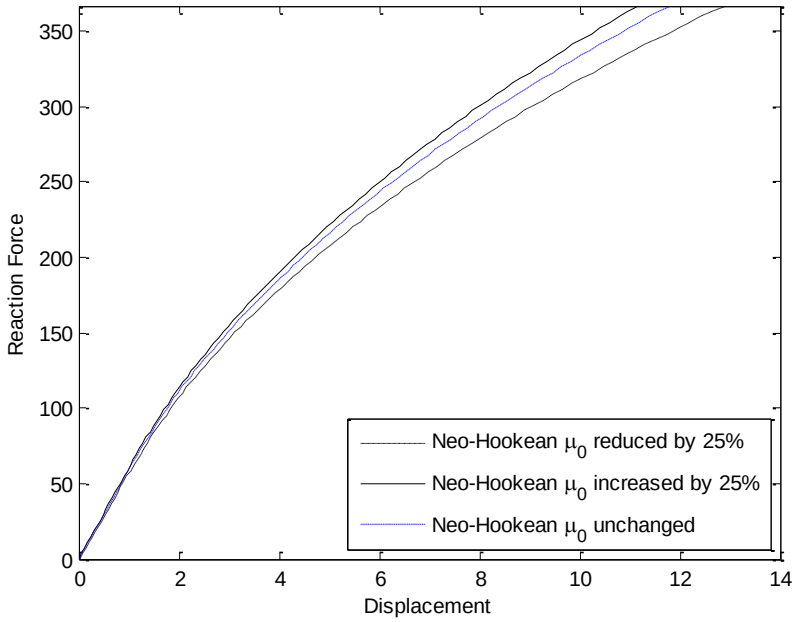

Figure 4.4: Comparison of load deflection curves for different Neo Hookean models for the ring. Properties of spokes are not changed.

The vertical displacement of the Tweel hub center for a constant load of 366.5 dN for different material models are summarized in Table 4-1.

Table 4-1: Vertical displacement of the Tweel model with changing ring material properties after a vertical load of 366.5 dN.

Material Model		Hub center displacement (mm)
Marlow	Shear modulus μ_0	10.29
Mooney Rivlin	minus 25%	11.07
	plus 25%	10.22
	unchanged	10.52
Neo Hookean	minus 25%	12.87
	plus 25%	11.16
	unchanged	11.78

4.2.2 Change in spoke material properties

Figure 4-5 shows the load-deflection curves for the three different models in the spoke, keeping the ring with the original Marlow material properties unchanged. In this case, the differences in the load-deflection curves for the Mooney-Rivlin and Neo-Hookean material models when compared to the Marlow model are significantly larger than in the study where only the ring properties where changed.

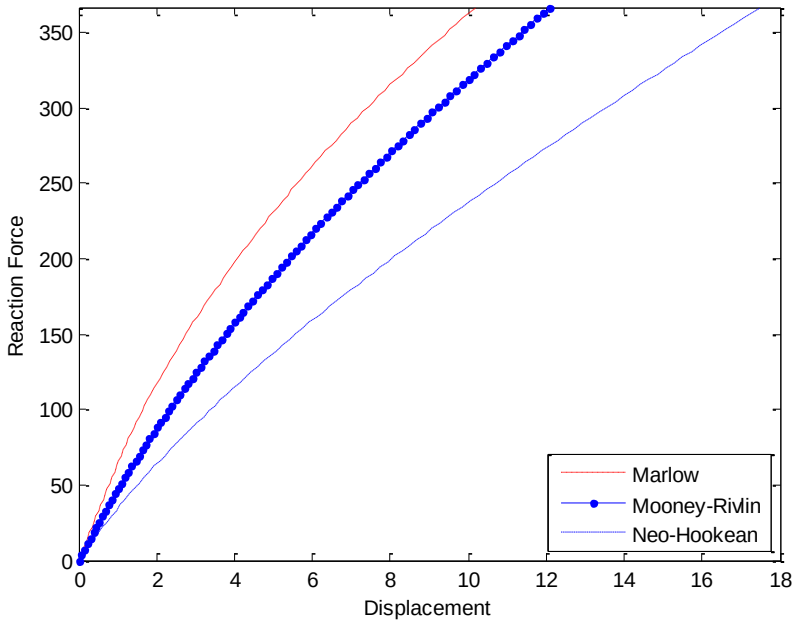

Figure 4.5: Comparison of load deflection curves for Marlow, fitted Mooney Rivlin and Neo Hookean material models for the spokes. Ring properties are not changed.

Figure 4.6 describes the tangent slopes of the load deflection curves for changing the initial shear modulus for the Mooney Rivlin by plus/minus 25%. Similarly, Figure 4.7 describes the tangent slopes of the load deflection curves for changing the initial shear

modulus for the Neo Hookean model by plus/minus 25%. When the load deflection curves for changing spoke material are compared, the tangent slopes have the same pattern as that of the ring, but the magnitudes of the vertical stiffness' are different.

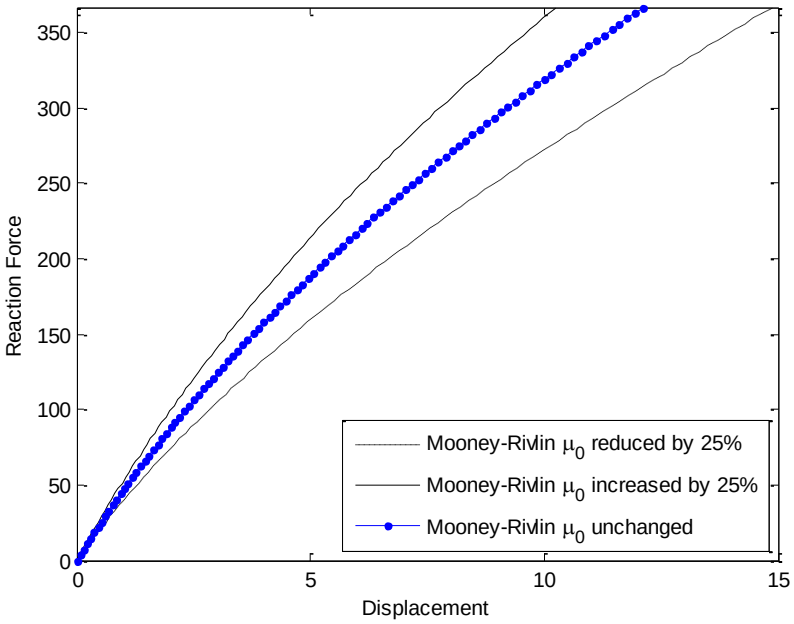

Figure 4.6: Comparison of load deflection curves for different Mooney-Rivlin models for the spoke. Ring properties are not changed.

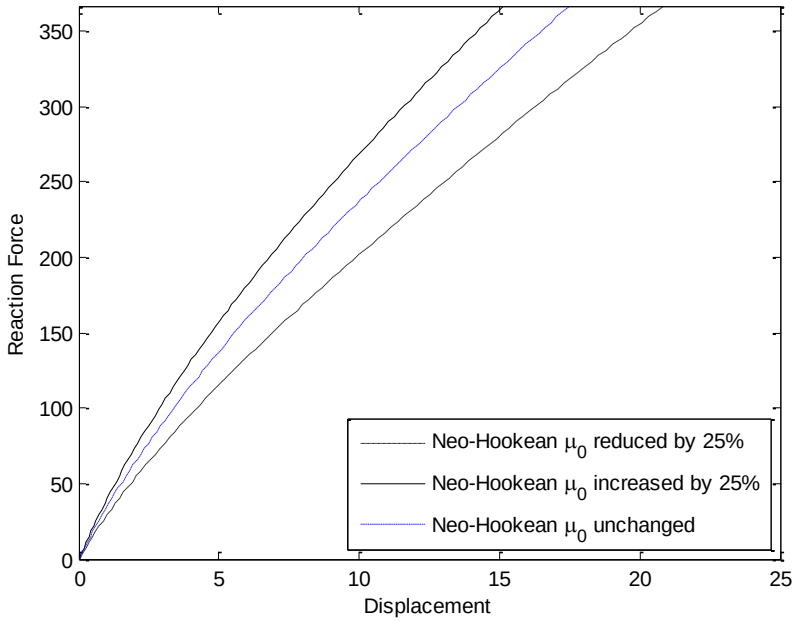

Figure 4.7: Comparison of load deflection curves for different Neo Hookean models for the spoke. Ring properties are not changed.

The deflections for a constant load of 366.5 dN for different material models are summarized in Table 4-2. From the values provided in Table 4-1 and Table 4-2, it is seen that the Tweel deflects more when its stiffness is less and vice versa.

Table 4-2: Vertical displacement of the Tweel model with changing spoke material properties after a vertical load of 366.5 dN.

Material Model		Deflection (mm)
Marlow	Shear modulus μ_0	10.29
Mooney Rivlin	minus 25%	14.88
	plus 25%	10.25
	unchanged	12.11
Neo Hookean	minus 25%	20.84
	plus 25%	15.12
	unchanged	17.5

CHAPTER FIVE – EFFECTS OF CHANGING MATERIAL PROPERTIES ON STEADY STATE ROLLING ON A FLAT GROUND

From [3, 4, 5, 6, 7], it has been hypothesized that the prime sources of noise and vibration produced by the Tweel include spoke vibration, ring vibration and ground contact interaction. When the spokes come into the contact zone, they buckle due to the application of load and snap back into tension on exiting the contact zone. This behavior of the spokes creates vibration, which may lead to unwanted sound radiation and noise. Since the spokes are connected to the ring, this causes the ring to vibrate, and visa versa. Another source of noise and vibration is due to the shearing of the shear beam and the bending of the integrated ring structure when in the contact zone. Due to application of load, the contact patch created by the Tweel with the ground becomes flat and causing the entire ring to vibrate. As a result, the tread starts to vibrate along with the ring and causes fluctuations in the contact forces. This also can be a possible source of noise.

In [3, 4, 5, 6, 7], spoke vibration, ring vibration and ground reaction forces were investigated to study the vibrations produced by the Tweel. All these previous studied used a planar model for the Tweel. In [3,4], the time-signal for changes in spoke length from the 2D planar model are transferred as boundary conditions for a detailed 3D single spoke model. As discussed in the thesis objectives in Chapter 1, a goal of this work is to study spoke and ground force vibration using a complete 3D Tweel model. In addition, in order to remove any possibility of potential numerical artifacts due to assumptions of nonzero initial conditions, the analysis in the present study is carried out starting from rest, with the Tweel rolling across a fixed ground surface, including the effects of

friction. Similar to the previous studies, the Tweel vibration during steady state rolling is measured by perpendicular distance of spoke marker nodes from the virtual plane of the spoke and fluctuations in contact ground contact forces. The time signals are processed using Fast Fourier Transforms (FFT) for analyzing frequency response. Using the analysis procedure described in 0, in the rolling phase (0.105 – 0.405 seconds), the Tweel makes approximately 4 revolutions. The time increment of the output time history used in the frequency response analysis during the rolling step is 0.000416 sec.

The purpose of this study is to determine the sensitivity and effects of changes in material properties for the spokes and ring on the vibration amplitudes in the Tweel spokes and ground force interaction. Results for vibration of the spokes and ground force are first reported for the reference Tweel with Marlow properties for the spoke and ring as described in Chapter Three. In the remaining sections of this chapter, comparisons are made from changes in Marlow properties to Neo Hookean and Mooney Rivlin for ring and spoke materials, including plus/minus 25% changes in modulus.

5.1 Vibration due to collapse of spokes

Spoke vibration is an important behavior of the Tweel which plays a role in fatigue and source of noise. To measure the spoke vibration, the lateral movement of the spokes is calculated from an imaginary plane passing through the ends of the spoke. This distance is also referred to as the perpendicular distance of the spoke. The lateral movement is recorded at selected marker nodes on the spoke. There are five marker nodes that are taken into consideration. They are the top node, upper quarter node, middle node, lower quarter node and the bottom node of a spoke edge. These nodes are present

on the inner edge of the left spoke on the spoke pair which is in the original contact zone before rolling. Figure 5.1 shows the marker nodes used to measure perpendicular distance.

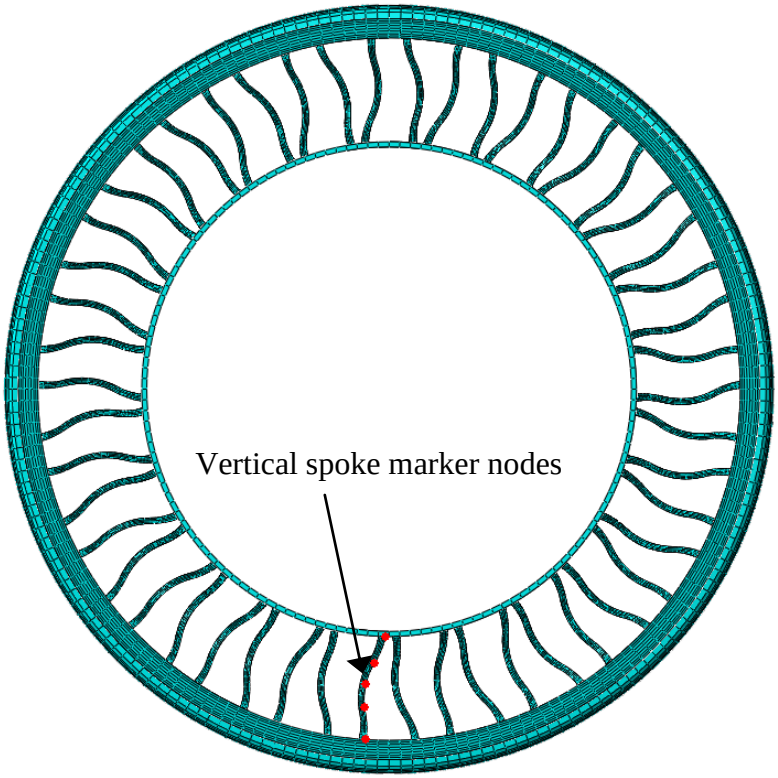

Figure 5.1: Vertical marker nodes involved in the calculation perpendicular distance of spoke marker nodes from virtual plane of spoke

In this Section the vibration due to alternating spoke collapse and tensioning is examined for the Tweel with hyperelastic Marlow reference material properties for the spokes and ring. The results will be used for comparisons in the later sections of this chapter. In Figure 5.2, the spoke marker nodes have been displayed in both the initial and deformed geometries after loading. Due to the buckling phenomenon of the spokes in the contact region, there is lateral displacement of the vertical marker nodes. It can be

seen that the spoke curvature for the deformed geometry is much larger than the initial geometry due to buckling. Since the spoke alternates between compression and tension during rolling, the spoke length keeps varying. The time history of displacements of the marker nodes are recorded for four revolutions during the steady rolling step (0.105 – 0.405 seconds).

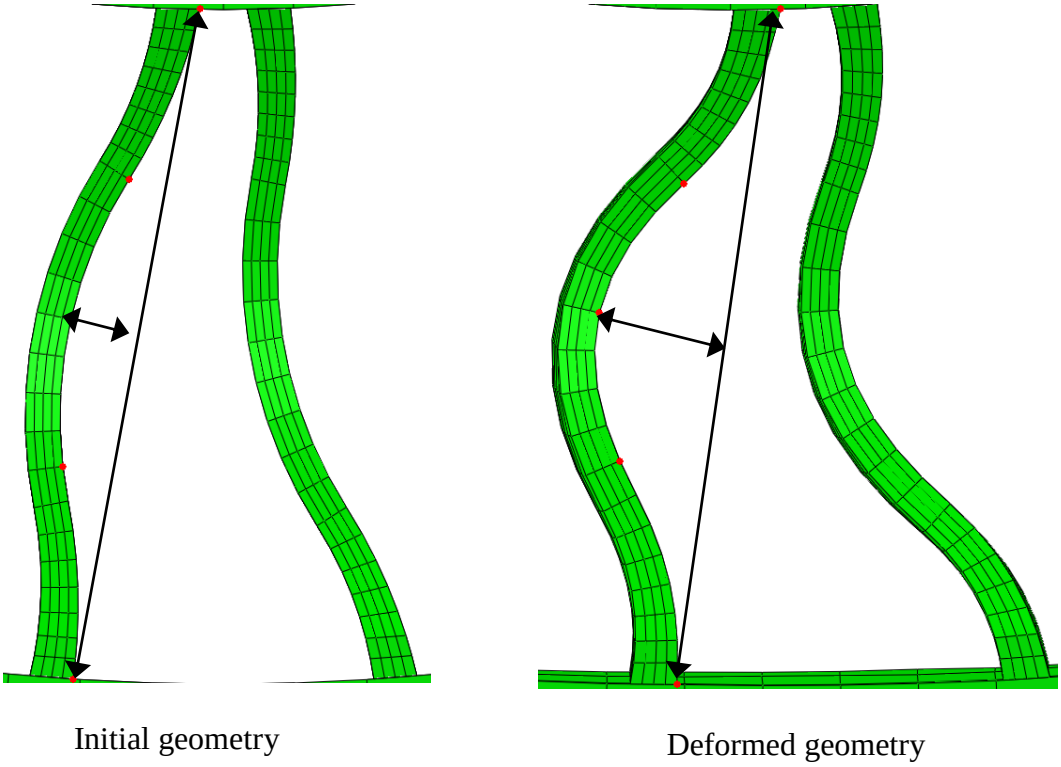

Initial geometry

Deformed geometry

Figure 5.2: Vertical spoke marker nodes in both initial and deformed geometries of the Tweel

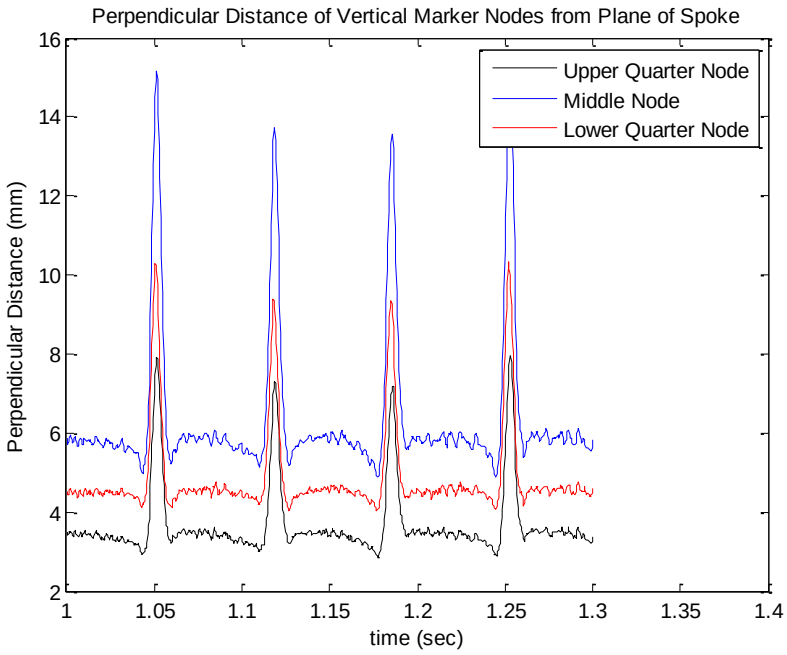

Figure 5.3: Perpendicular distance of the vertical spoke marker nodes from the plane of spoke

In Figure 5.3, the perpendicular distance of the spoke marker nodes is plotted during the steady rolling period. The mean length of the spoke during this period is 83.9872 mm. The amplitude of the middle node is the maximum when compared to the other quarter nodes on the spoke. The spoke collapse after each revolution of the Tweel is clearly seen in the data for all marker nodes by the large change in displacement at every 0.067 seconds. This corresponds to the spoke collapse frequency of 14.15 Hz. This is due to the buckling phenomenon of the spokes in the contact zone. We observe that the middle node has the largest lateral displacement when compared to the other marker nodes. Between spoke collapses, we observe oscillations in the time signals.

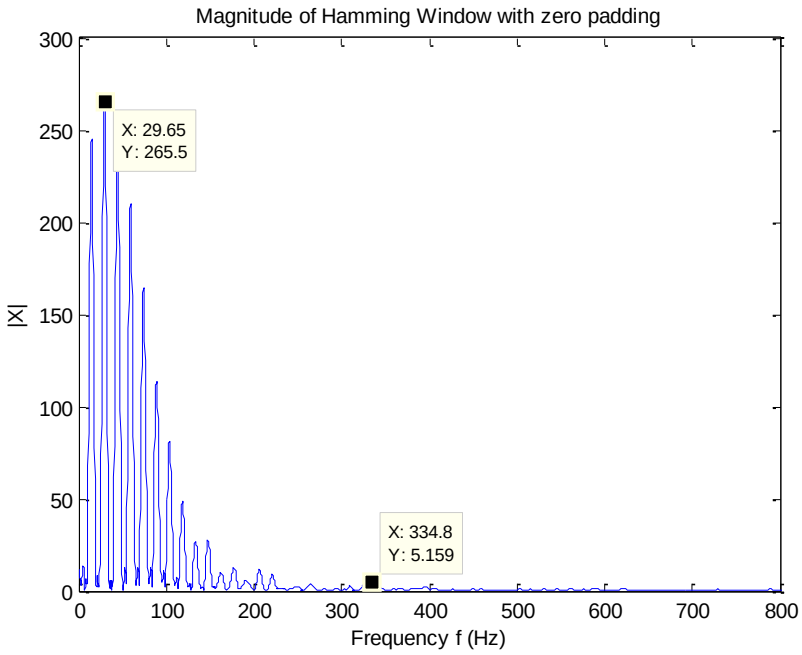

Figure 5.4: Magnitude of FFT with hamming window for perpendicular distance for middle vertical node.

Figure 5.4 is the magnitude of the FFT with hamming window and zero padding for the middle vertical node perpendicular distance. There are two peaks that are considered in this plot. The peak that occurs at 29 Hz is a multiple of the spoke collapse frequency of 14.15 Hz. This frequency corresponds to the spoke collapse that occurs at every 0.067 seconds. Since this peak is a result of the spoke collapsing due to the buckling phenomenon, it will not be considered for analyzing spoke vibration. The amplitudes below approximately 100 Hz are considered the response from the spoke collapse frequency and associated harmonics. Above approximately 100 Hz, the amplitudes due to spoke vibration are very small. The peak that will be considered is the one that occurs at 335 Hz. These small peaks near 335 Hz result from the oscillations in the perpendicular distance time signal during the tension phase of the spoke. The root-

mean-square (RMS) of the FFT amplitudes for the middle node in the reference model over a frequency range between 200 to 800 Hz is 1.4246. RMS gives a measure of the overall vibration amplitude for frequency region of interest. The RMS of a set of *N*, amplitude values is computed from,

$$RMS = \sqrt{\sum_{i=1}^{N} \frac{x_i^{\,2}}{N}} \ .$$

5.2 Vibration due to ground interaction

One of the main sources of vibration is due to the interaction between the Tweel and the ground while rolling. This is estimated by observing the ground reaction force time signal during rolling and the corresponding FFT frequency response of the zero mean signal. The results in this Section are given for the reference Marlow model and will be used for comparisons in the later sections of this chapter.

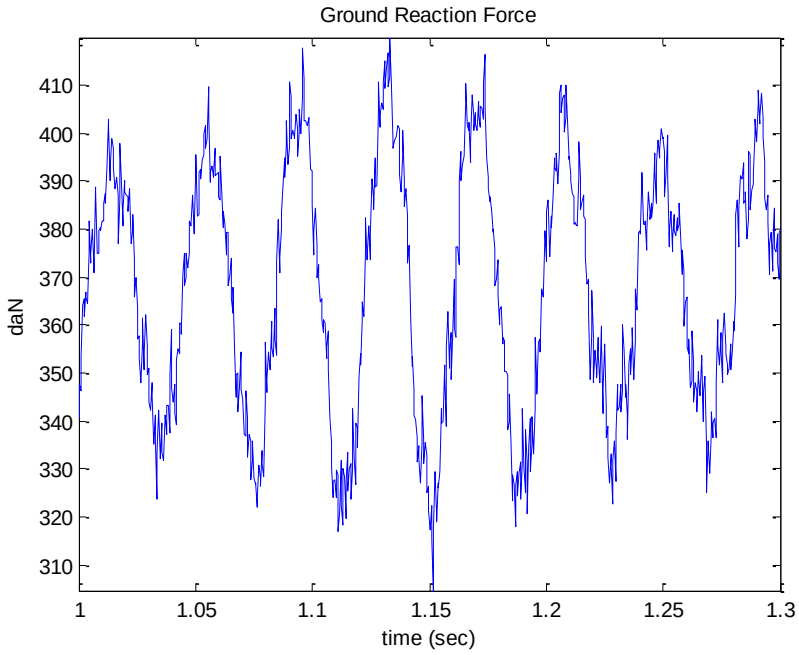

Figure 5.5: Reaction force exerted by the ground on the Tweel

Figure 5.5 gives the reaction force interaction time signal between the rigid flat ground and the Tweel during steady rolling. The mean value of the ground reaction force for the reference model during steady rolling is recorded as 367.6758 daN. Low frequency oscillations in the signal with period of approximately 0.067 seconds correspond to the spoke collapse frequency for one complete revolution of the Tweel.

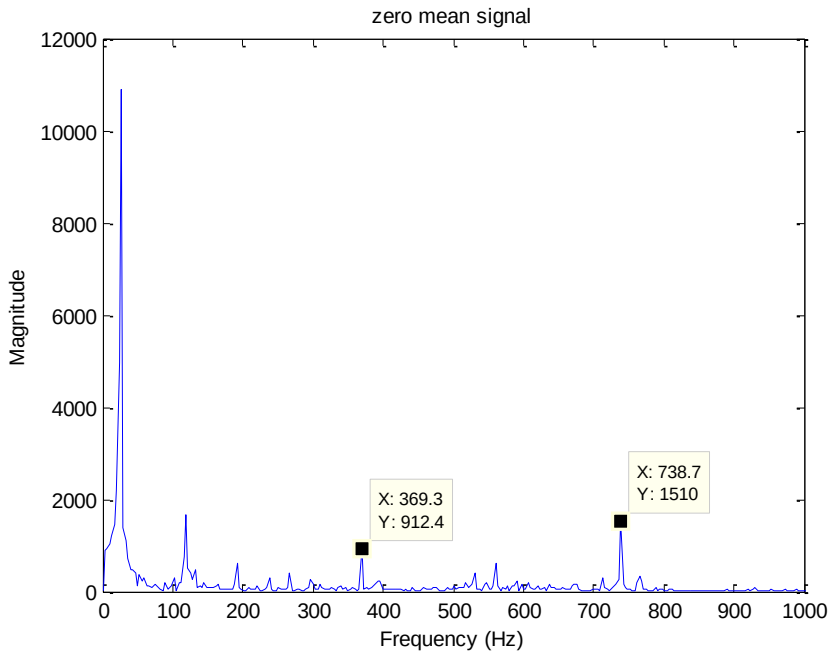

Figure 5.6: FFT amplitude for the ground reaction force

In Figure 5.6, the highest FFT amplitude peak occurs at the spoke collapse frequency of 14.15 Hz. Other large FFT amplitude peaks occur at 369.3 Hz and 738.7 Hz. The first peak at 369.3 Hz corresponds to the spoke pair passing frequency which depends on the angular velocity with which the Tweel is rolling and the number of spokes (recall the Tweel considered has 25 spoke pairs). The vibration at this frequency

may be due to the discrete stiffness of the spokes [5]. Also, the peak at 738.7 Hz corresponds to the single spoke passing frequency which is twice the spoke pair passing frequency. The RMS of the ground reaction force amplitudes over a frequency range of 200 to 1000 Hz is 94.

5.3 Effects of Material Properties on Vibration during steady state rolling

A material study is performed in the following sections of this chapter. In this study, the spoke and the ground interaction vibration is analyzed and compared using corresponding FFT amplitude RMS values. The following sets of results are reported for the ring material changed to Mooney Rivlin and Neo Hookean while keeping the same Marlow material on the spokes.

5.3.1 Mooney Rivlin model for ring with unchanged shear modulus

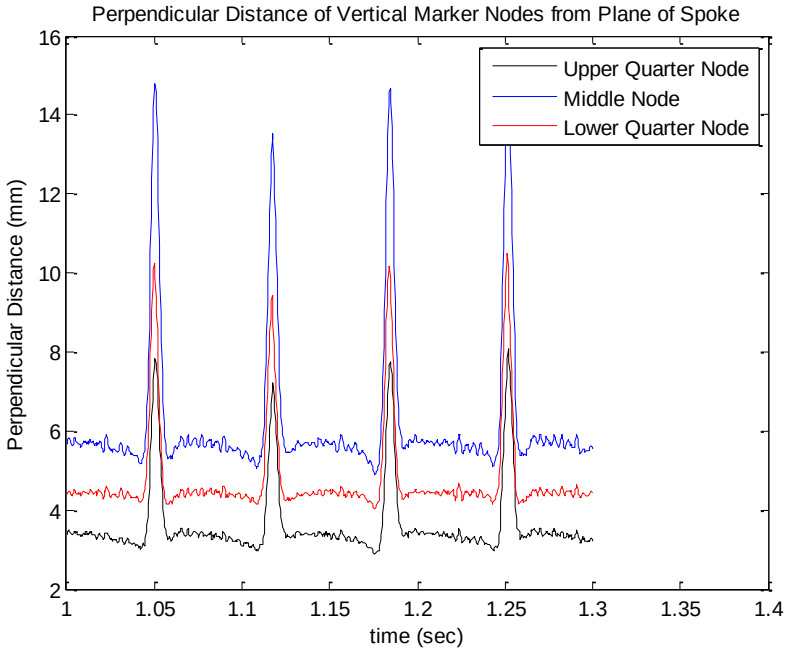

Figure 5.7: Perpendicular distance of spoke marker nodes from plane of spoke.

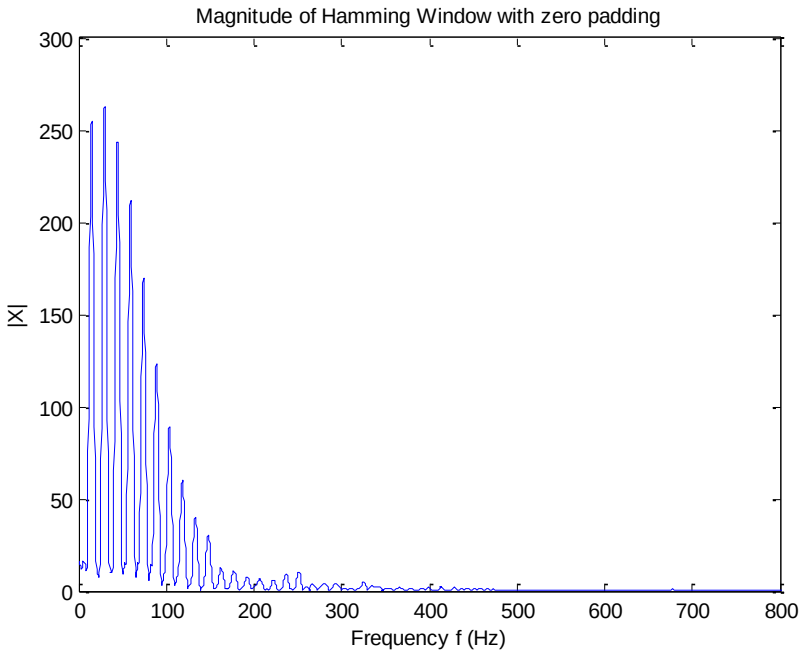

Figure 5.8: Magnitude of FFT amplitude of perpendicular distance for middle node.

From Figure 5.7 and Figure 5.8, the RMS of the FFT amplitudes for spoke vibration is 1.5971. The average spoke length is 83.9813 mm. The peak amplitude for spoke vibration occurs at 325 Hz.

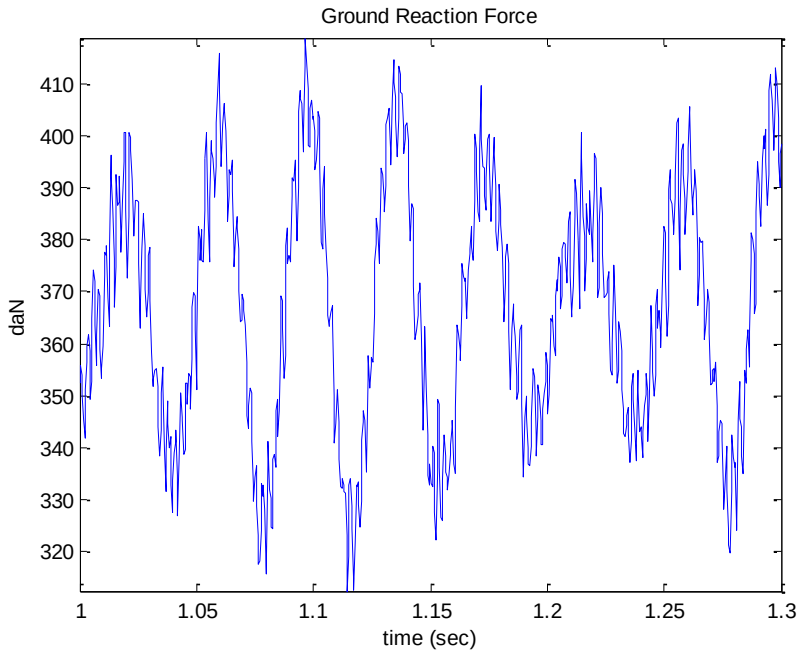

Figure 5.9: Ground Reaction force

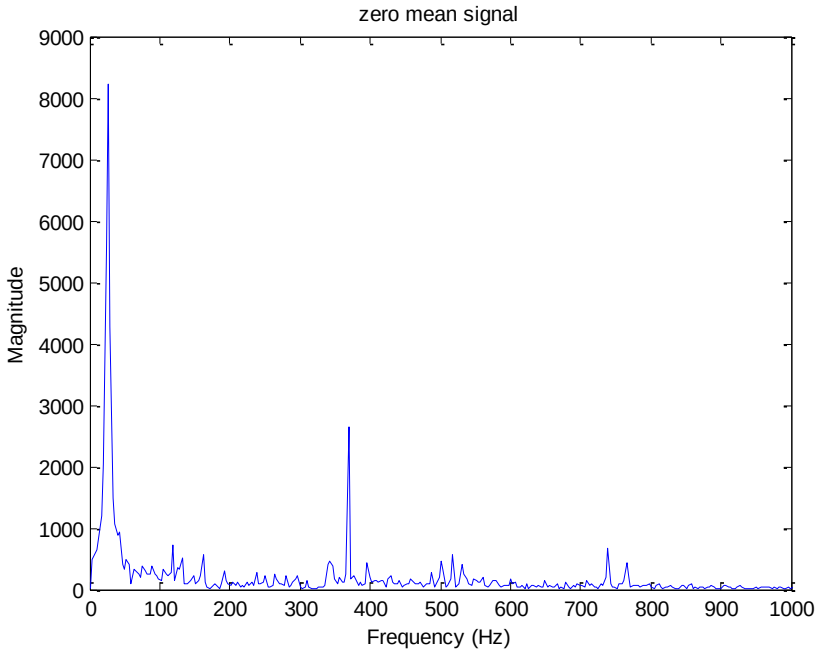

Figure 5.10: FFT amplitude for the ground reaction force

From Figure 5.9 and Figure 5.10, the average ground reaction force for the Tweel model with a Mooney Rivlin unchanged model is 367.1612 daN. In Figure 5.10, the two

peaks that are considered the spoke pair passing frequencies occur at 369 Hz and 739 Hz. The RMS of the FFT amplitude for the ground reaction force over a frequency range from 200 Hz to 1000 Hz is 130.

5.3.2 Shear modulus of Mooney Rivlin model for the ring is reduced by 25%

From Figure 5.11 and Figure 5.12, the RMS of the FFT amplitudes for spoke vibration is 2.4242. The average spoke length is 83.9872 mm. The peak amplitude for spoke vibration occurs at 322 Hz.

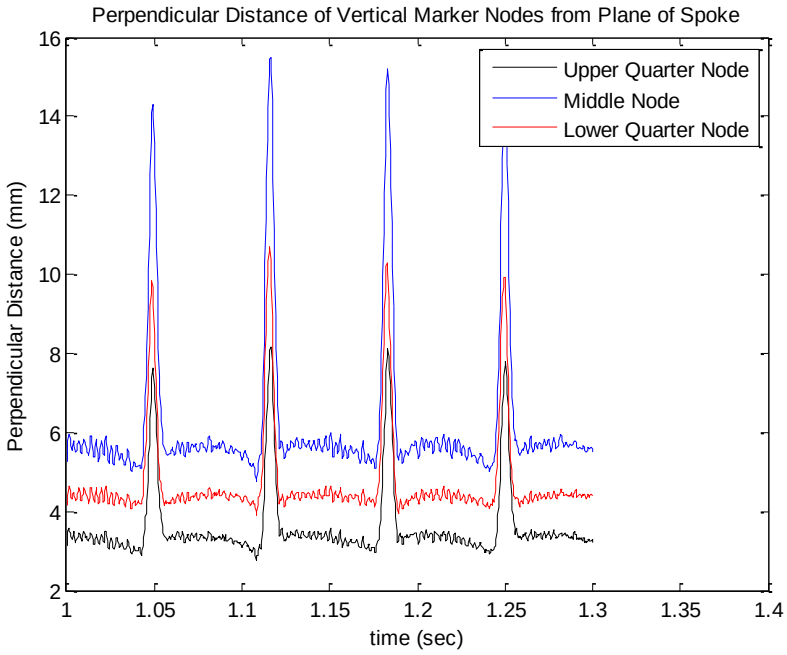

Figure 5.11: Perpendicular distance of vertical marker nodes from plane of spoke

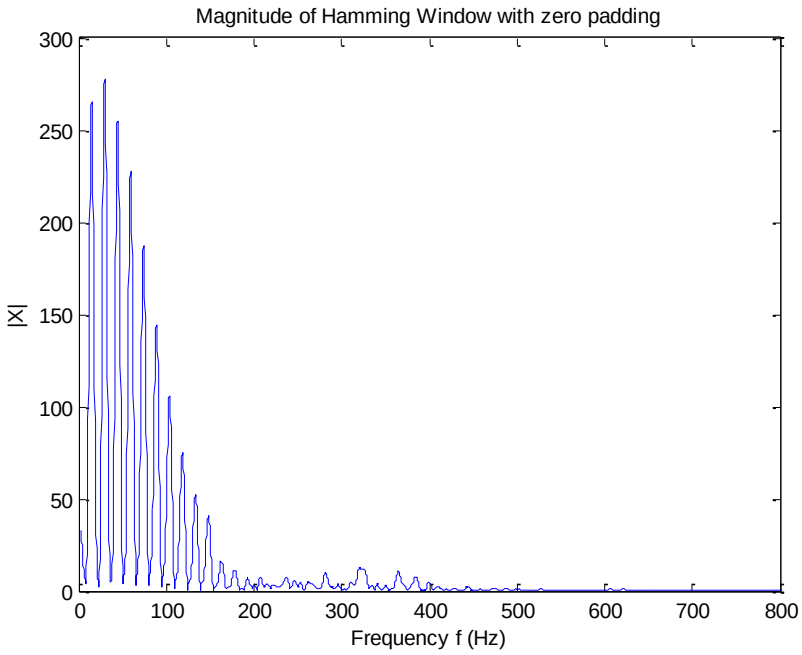

Figure 5.12: Magnitude of FFT amplitude of perpendicular distance for the middle node

From Figure 5.13, the average ground reaction force for the Tweel model with a Mooney Rivlin reduced model is 365.6308 daN. In Figure 5.14, the two peaks that are considered occur at 370 and 740 Hz. The RMS of the FFT amplitude for the ground reaction force over a frequency range from 200 Hz to 1000 Hz is 313.

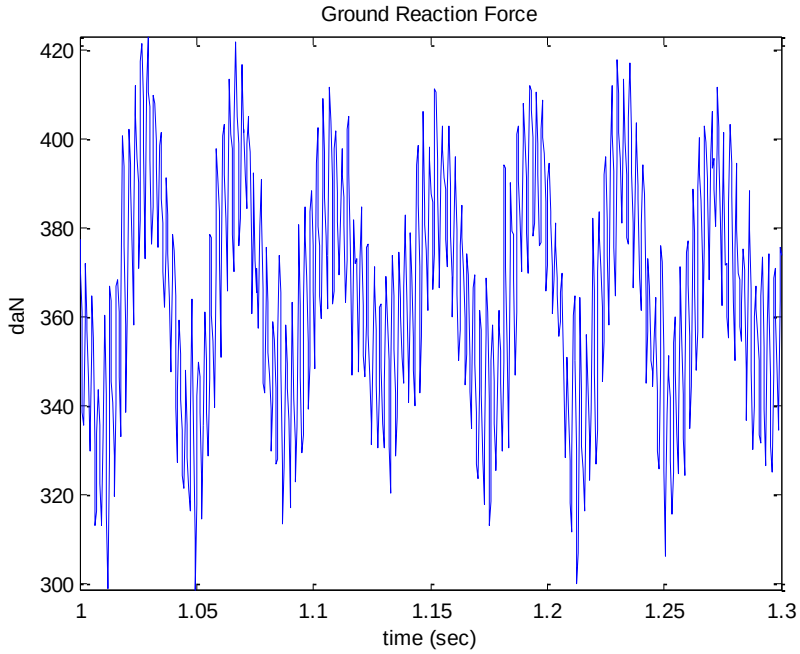

Figure 5.13: Ground reaction force

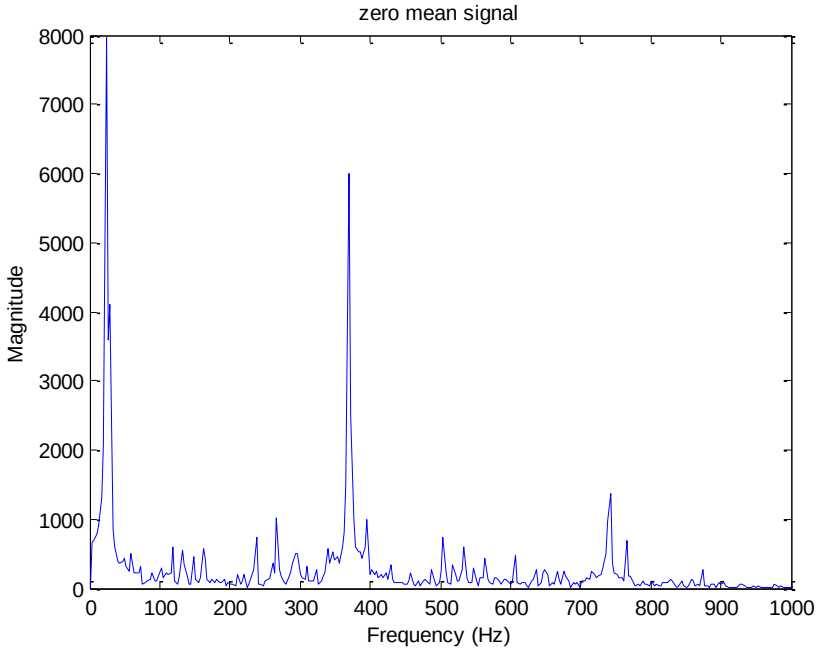

Figure 5.14: FFT amplitude for ground reaction force

5.3.3 Shear modulus of the Mooney Rivlin model for the ring is increased by 25%

From Figure 5.15 and Figure 5.16, the RMS of the FFT amplitudes for spoke vibration is 1.7761. The average spoke length is 83.9246 mm. The peak amplitude for spoke vibration occurs at 328 Hz.

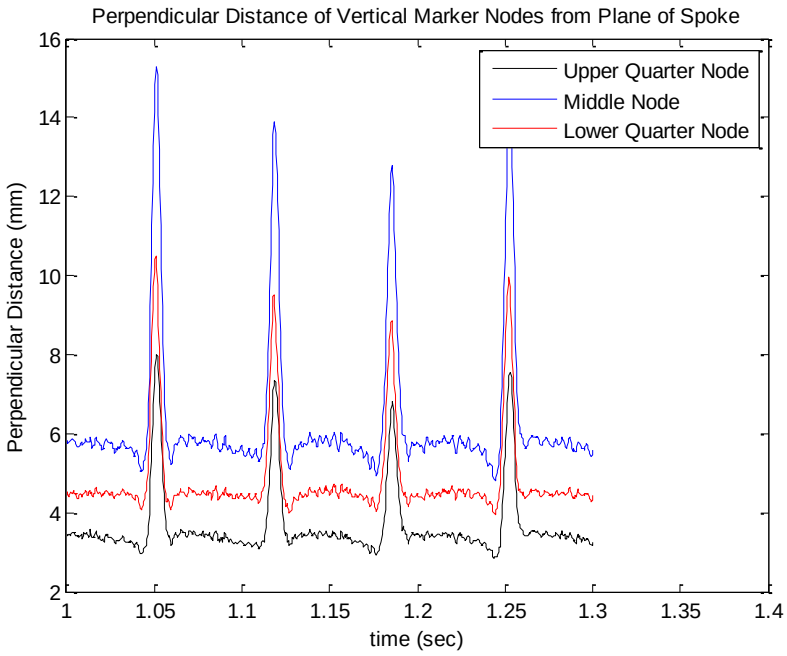

Figure 5.15: Perpendicular distance of vertical marker nodes from plane of spoke

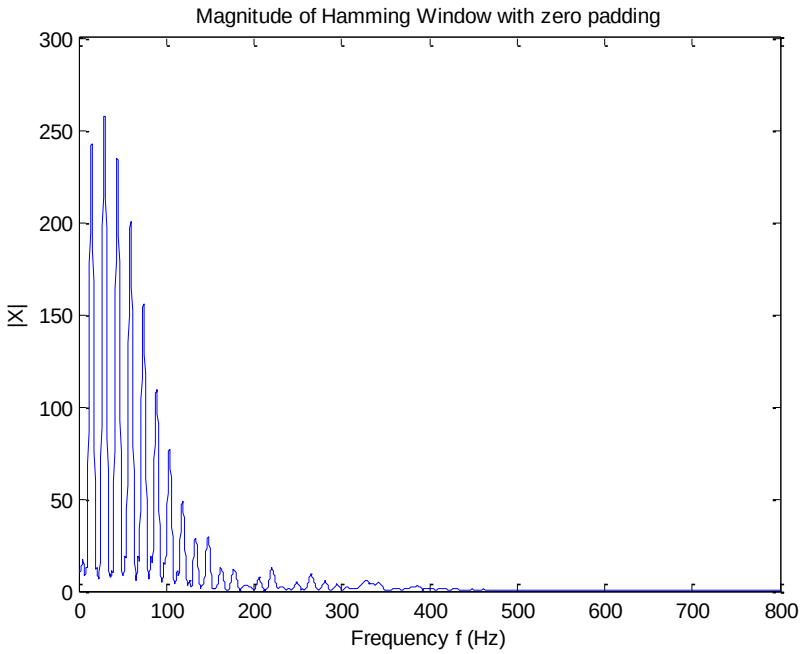

Figure 5.16: Magnitude of FFT amplitudes of perpendicular distance for the middle node

In Figure 5.17, the average ground reaction force for the Tweel with a Mooney Rivlin increased model is 367.7807 daN. In Figure 5.18, the two important peaks occur at frequencies 343 and 765 Hz. The RMS of the FFT amplitudes for the ground reaction force over a frequency range from 200 Hz to 1000 Hz is 71.

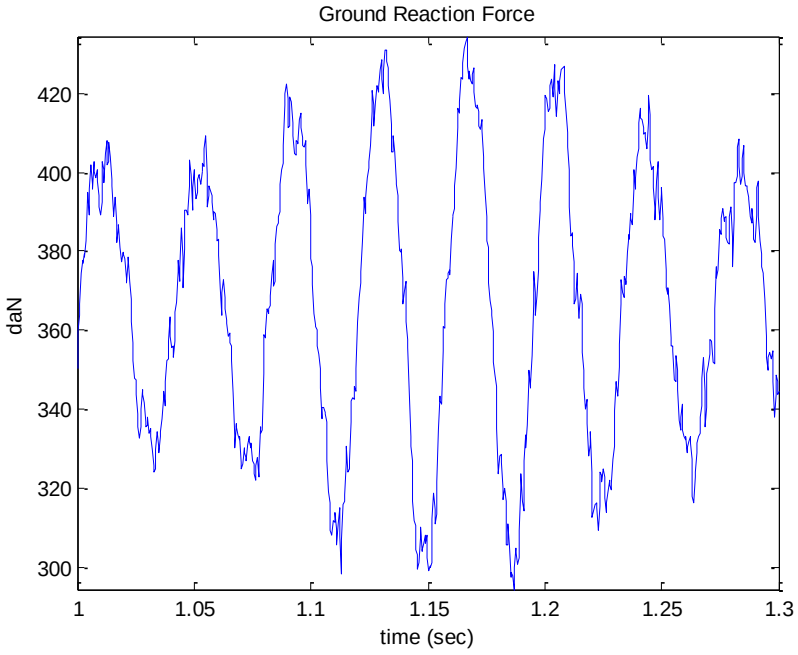

Figure 5.17: Reaction force exerted by the ground on the Tweel

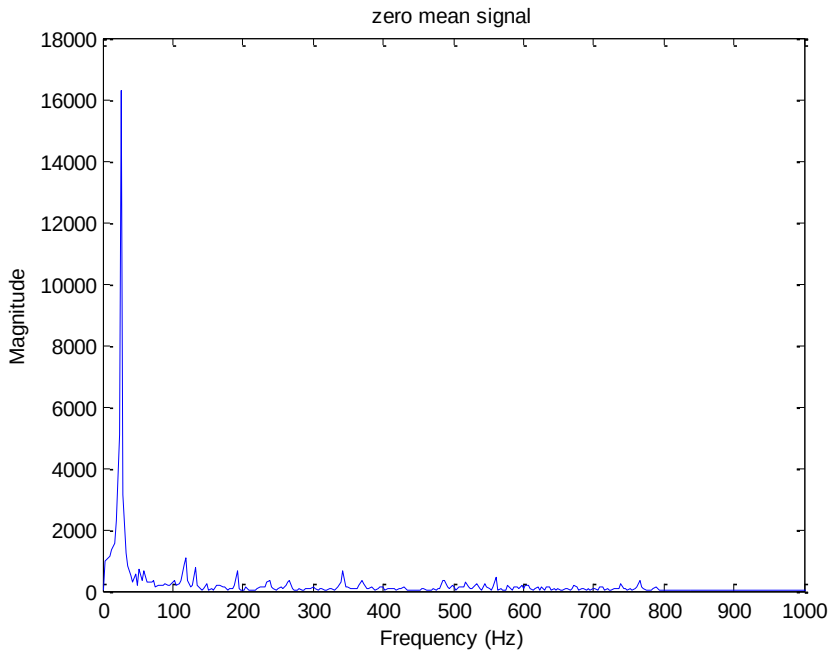

Figure 5.18: Magnitude of FFT amplitudes for ground reaction force

5.3.4 Neo Hookean model for the ring with original fitted data

From Figure 5.19 and Figure 5.20, the average length of the spoke is computed as 84.0367 mm. The RMS of the FFT amplitudes for spoke vibration is 2.4281. The peak amplitude for spoke vibration occurs at 311 Hz.

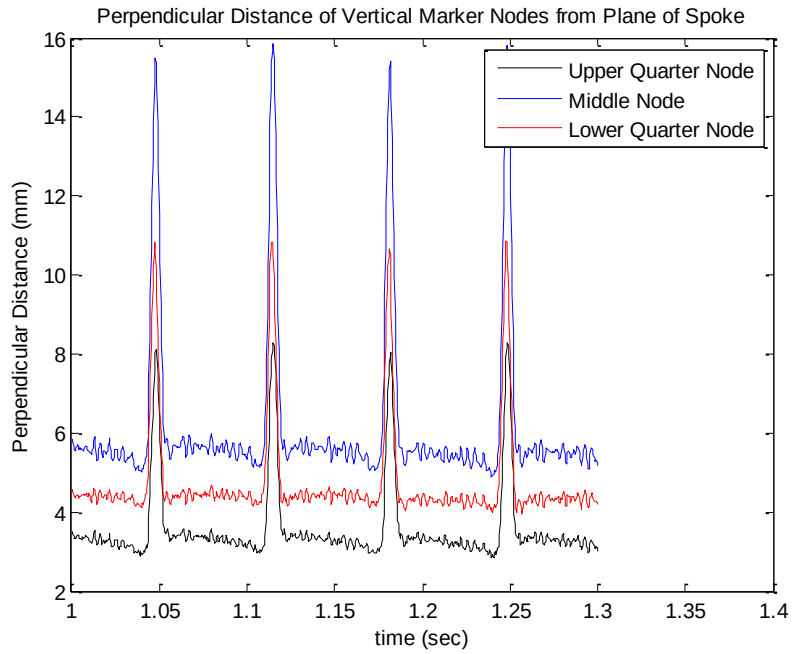

Figure 5.19: Perpendicular distance of vertical spoke marker nodes from plane of spoke

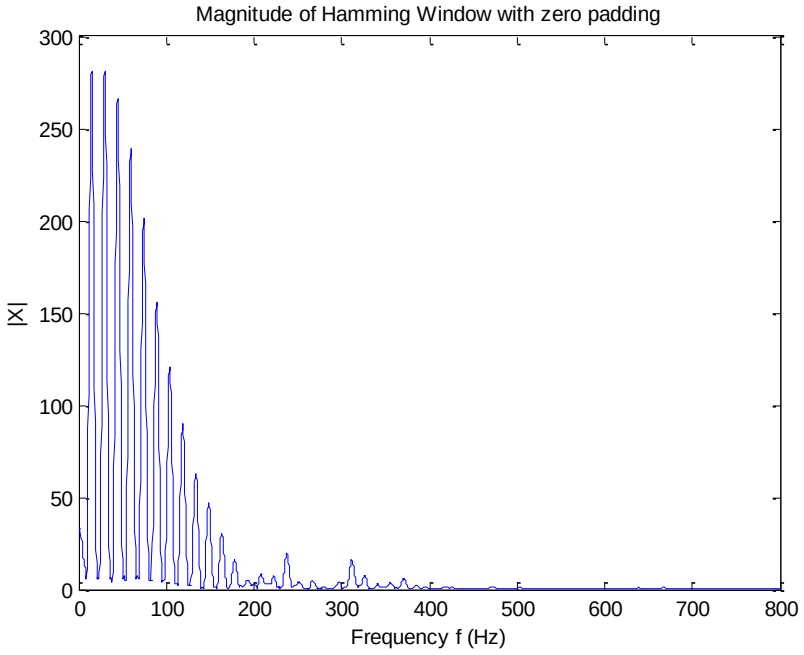

Figure 5.20: Magnitude of FFT amplitudes of perpendicular distance for the middle node

From Figure 5.21, the average reaction force is 366.4391 daN. In Figure 5.22, the two important peaks occur at 371 Hz and 742 Hz. The RMS of the FFT amplitudes for ground reaction force over a range from 200 Hz to 1000 Hz is computed as 213.

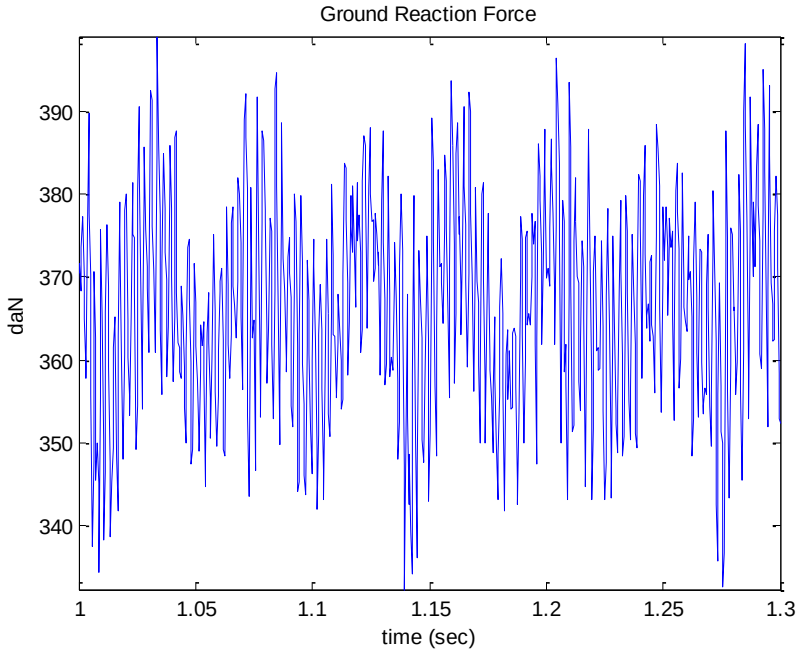

Figure 5.21: Ground reaction force

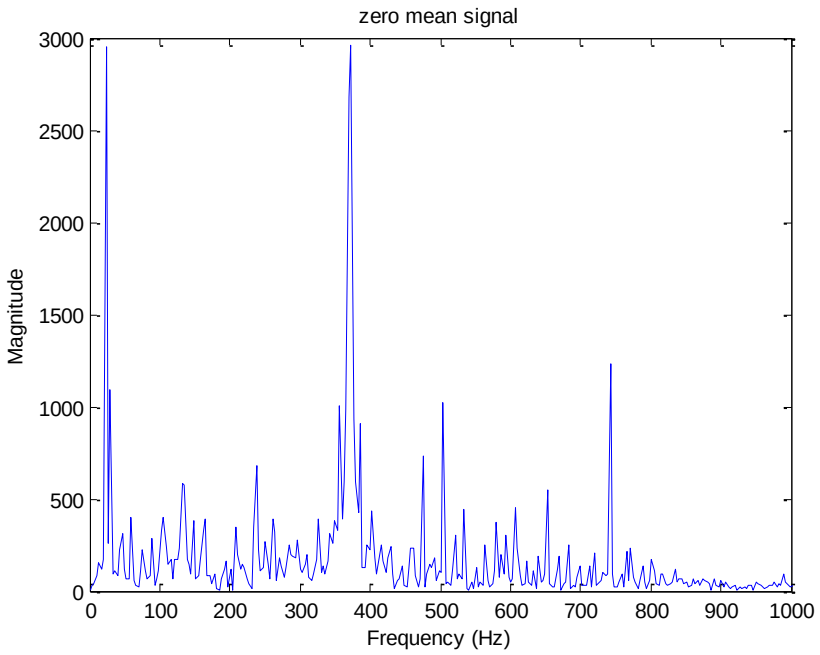

Figure 5.22: Magnitude of FFT amplitudes for ground reaction force

5.3.5 Shear modulus of the Neo Hookean model for the ring is reduced by 25%

From Figure 5.23 and Figure 5.24, the average length of the spoke is 84.0566 mm. The peak amplitude occurs at 372 Hz. The RMS of the FFT amplitude of spoke vibration for the middle node is 6.2373. In this case, there is clearly a large amplitude vibration in the spokes during the tension phase.

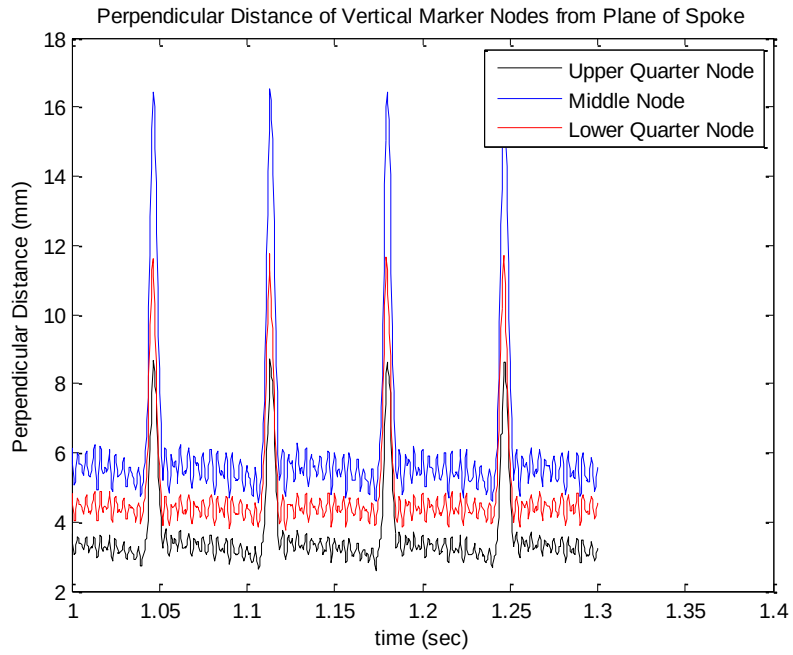

Figure 5.23: Perpendicular distance of vertical spoke marker nodes from plane of spoke

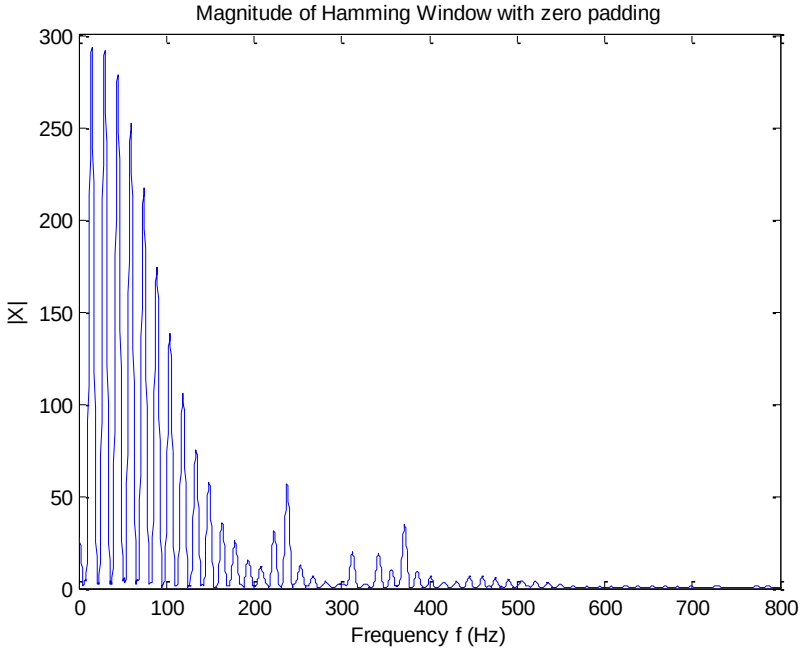

Figure 5.24: Magnitude of FFT amplitudes of perpendicular distance for middle node

In Figure 5.25, the average ground reaction force is 366.4078 daN. In Figure 5.26, the peak amplitudes occur at frequencies 373 and 742 Hz. The RMS of the FFT amplitude for ground reaction force is 479. The vibration amplitudes for ground force interaction much larger for this material property in the ring. Recall for this material with reduced shear modulus, the slope of the vertical load versus displacement was reduced indicating a soft stiffness.

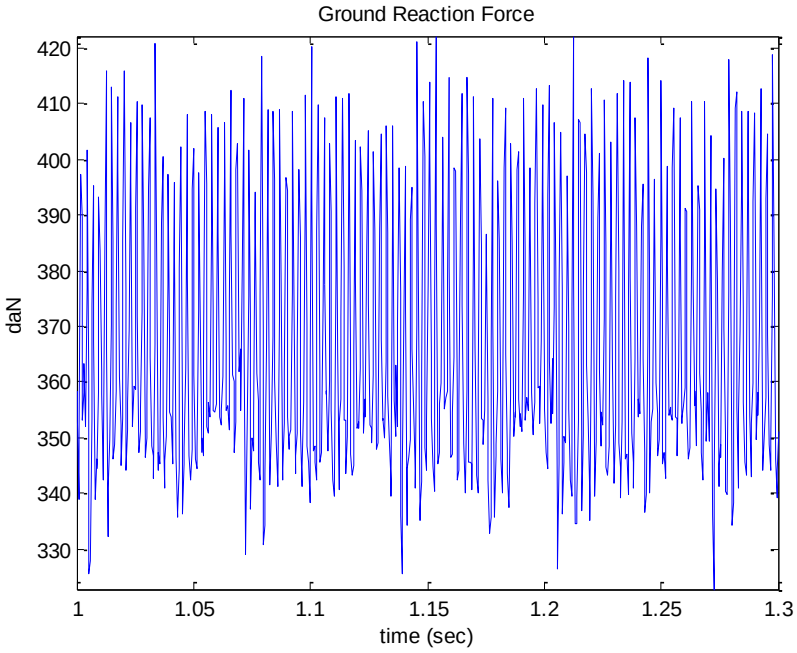

Figure 5.25: Reaction force exerted by the ground on the Tweel

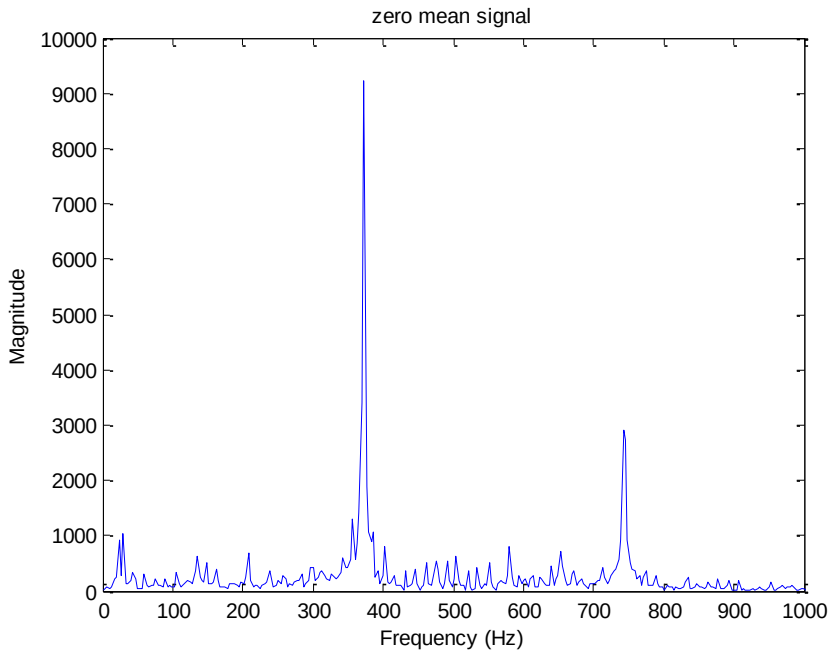

Figure 5.26: Magnitude of FFT amplitudes for ground reaction force

5.3.6 Shear modulus of Neo Hookean material model for the ring is increased by 25%

From Figure 5.27 and Figure 5.28, the average length of the spoke is 84.0784 mm. The peak amplitude occurs at a frequency of 326 Hz. The RMS of FFT amplitudes of perpendicular distance for middle node is 1.8513.

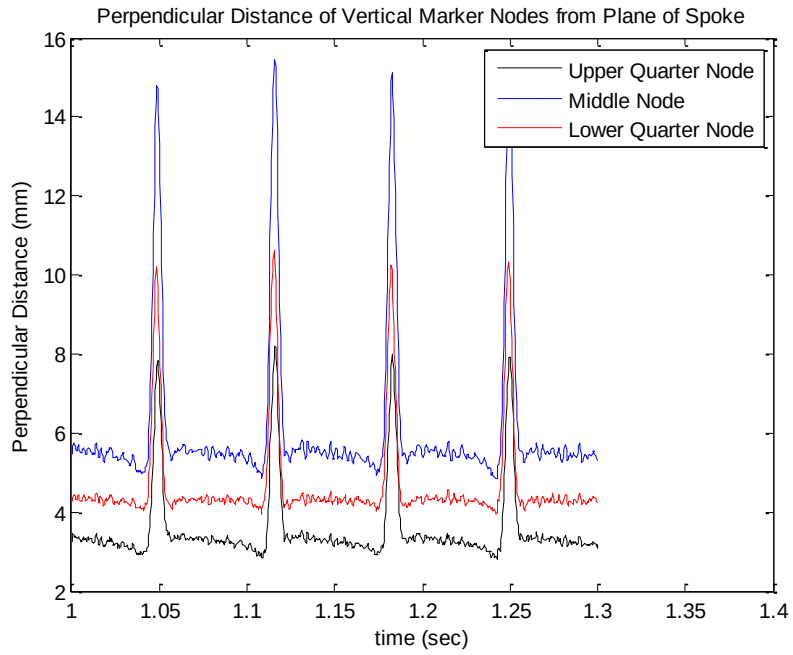

Figure 5.27: Perpendicular distance of spoke marker nodes from plane of spoke

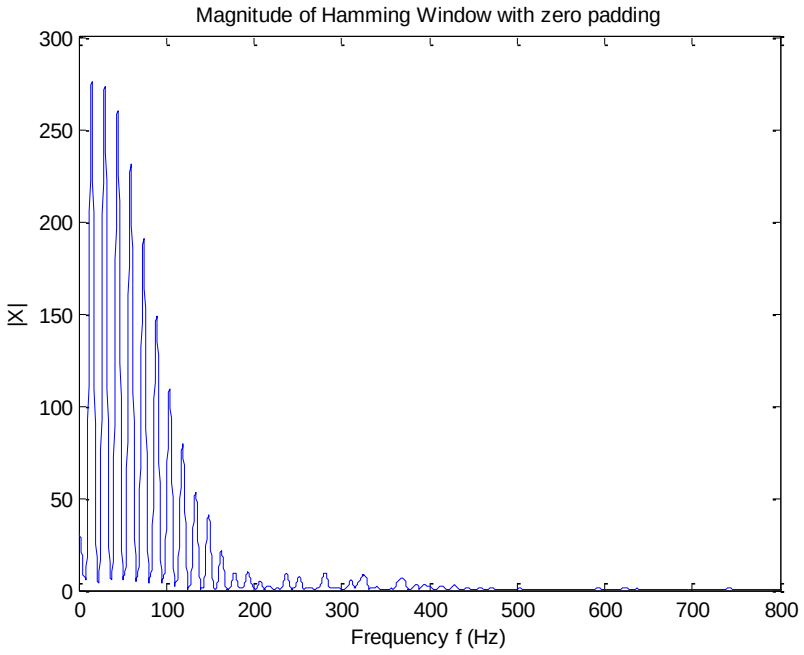

Figure 5.28: Magnitude of FFT amplitudes of perpendicular distance for middle node

In Figure 5.29, the average reaction force exerted by the ground on the Tweel is 366.2465 daN. In Figure 5.30 the peak FFT amplitudes occur at frequencies 371 and 741 Hz. The RMS of FFT amplitudes for the ground reaction force is computed as 288.

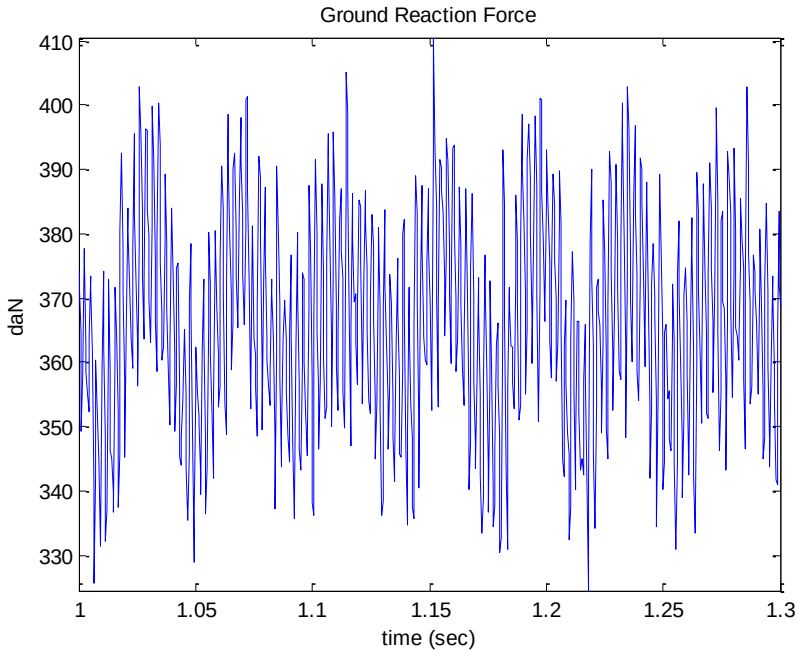

Figure 5.29: Ground reaction force

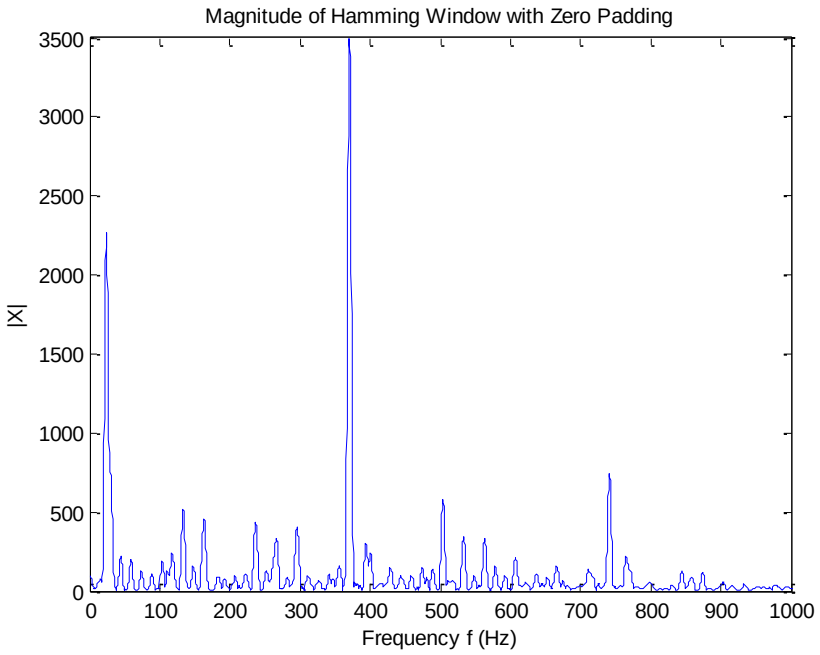

Figure 5.30: Magnitude of FFT amplitudes for ground reaction force

5.3.7 Shear modulus of the Mooney Rivlin model for the spokes remains unchanged

From Figure 5.31and Figure 5.32, the average length of the spoke is 83.9053 mm. The peak amplitude occurs at a frequency of 326 Hz. The RMS of the FFT amplitudes of perpendicular distance for the middle node is 2.2387.

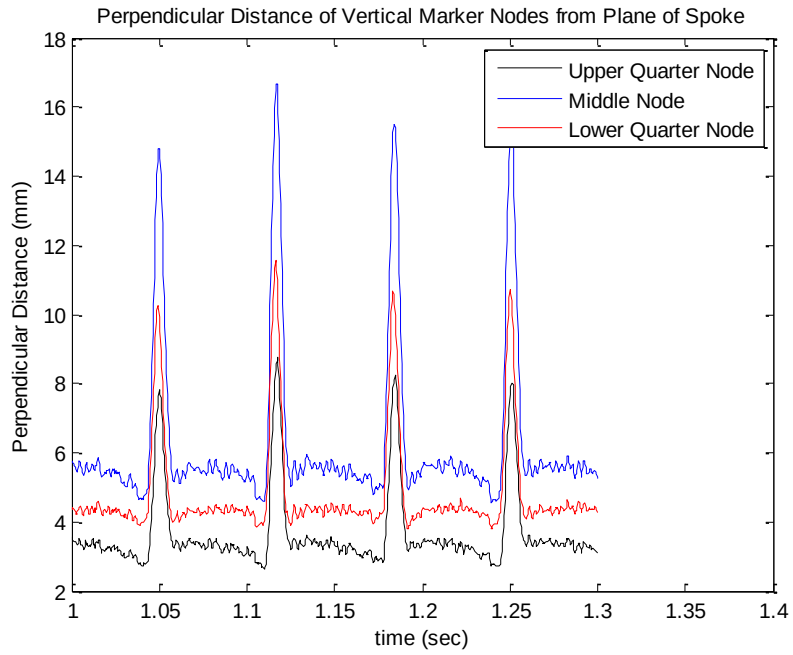

Figure 5.31: Perpendicular distance of vertical marker nodes from plane of spoke

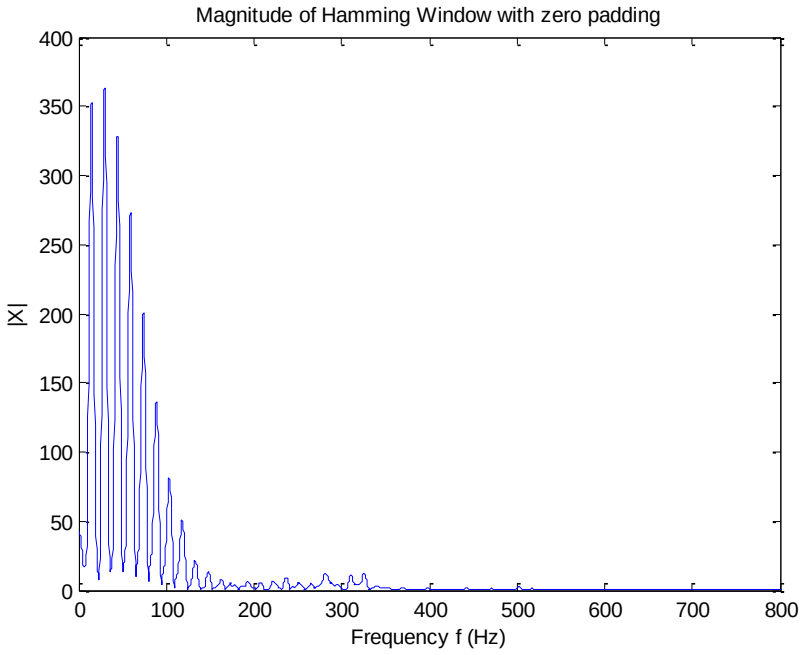

Figure 5.32: Magnitude of FFT amplitudes of perpendicular distance for the middle node

In Figure 5.33, the average ground reaction force is 365.6147 daN. In Figure 5.34, the peak amplitudes occur at frequencies of 370, 544 and 740 Hz. The RMS of FFT amplitudes for ground reaction force is 94.

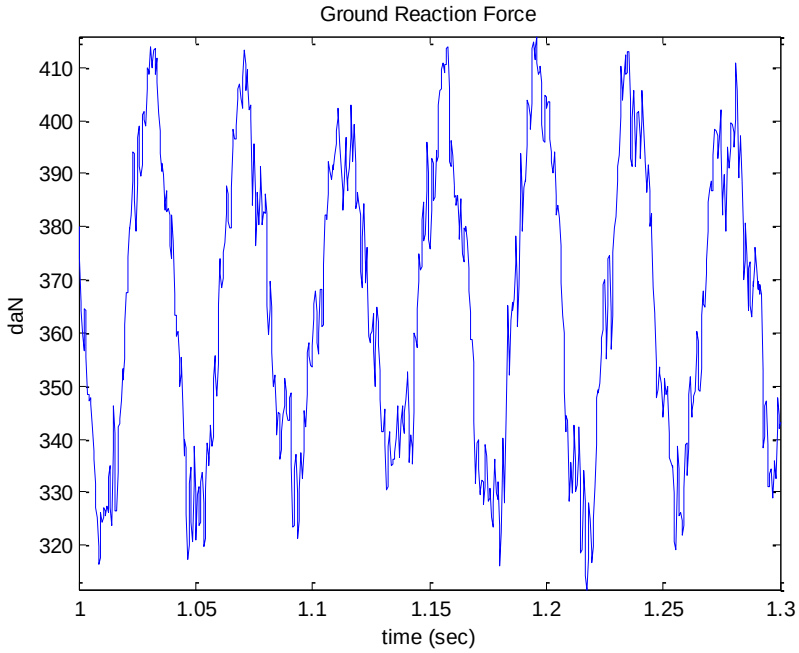

Figure 5.33: Ground reaction force

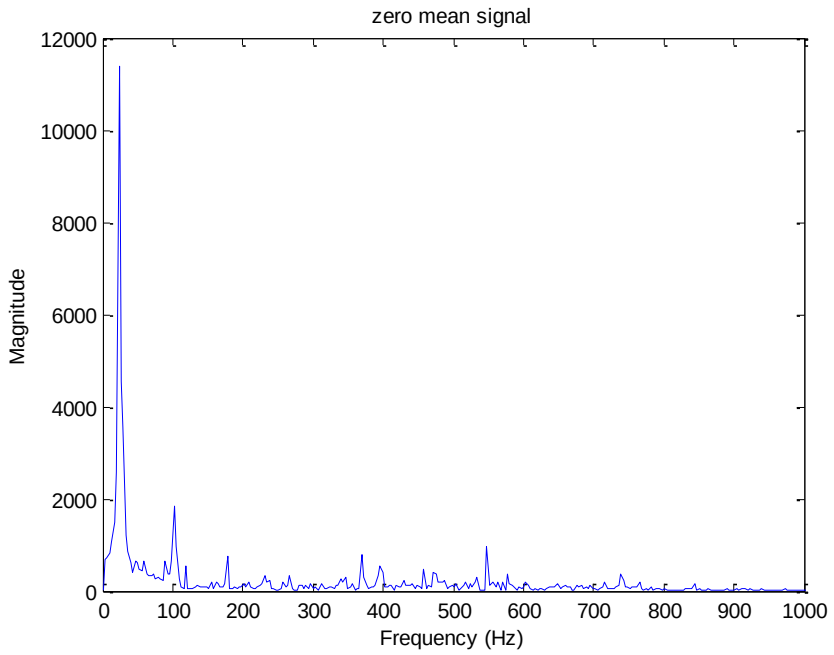

Figure 5.34: Magnitude of FFT amplitude for ground reaction force

5.3.8 Shear modulus of Mooney Rivlin material model for the spokes is reduced by 25%

From Figure 5.35 and Figure 5.36, the average length of the spoke is 83.8640 mm. The peak amplitude occurs at a frequency of 223 Hz. The RMS of FFT amplitude of perpendicular distance for middle node is 2.4583.

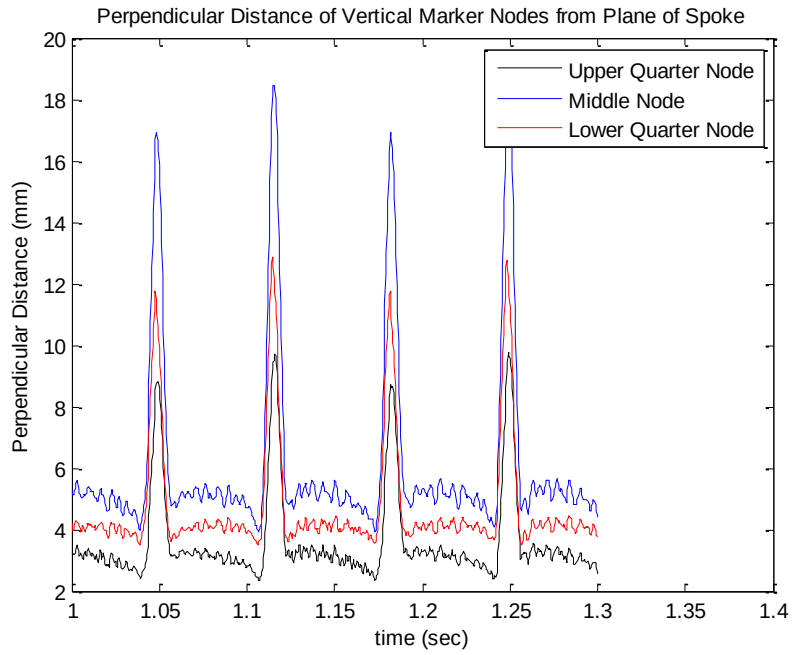

Figure 5.35: Perpendicular distance for vertical spoke marker nodes from plane of spoke

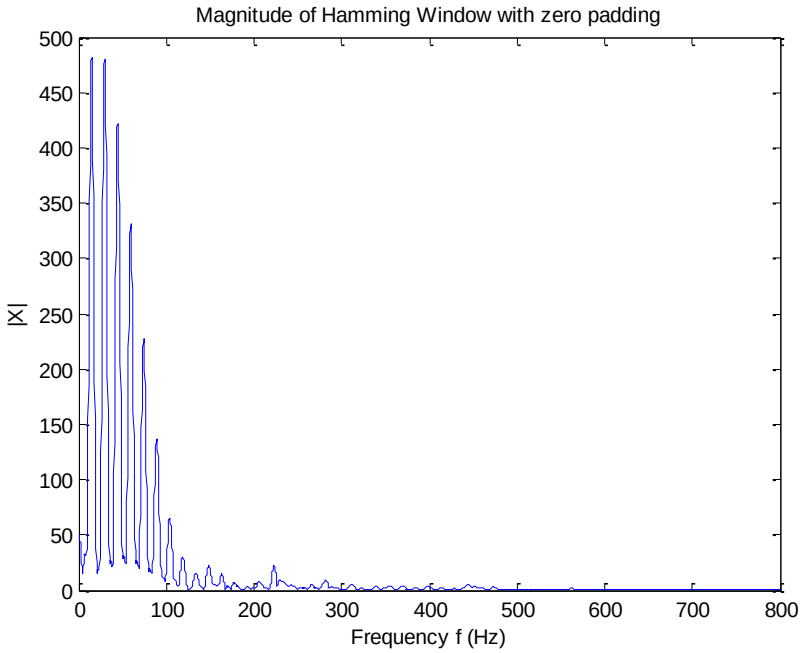

Figure 5.36: Magnitude of FFT amplitudes of perpendicular distance for middle node

In Figure 5.37, the average ground reaction force is 366.7383 daN. In Figure 5.38, the peak amplitudes occur at frequencies of 369, 534 and 772 Hz. The RMS of FFT amplitudes for ground reaction force is 141.

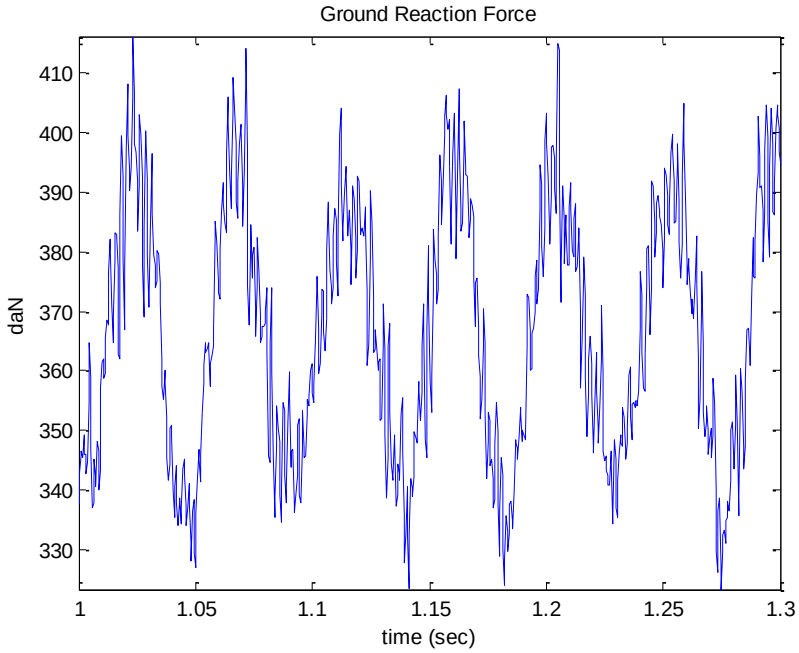

Figure 5.37: Reaction force exerted by the ground on the Tweel

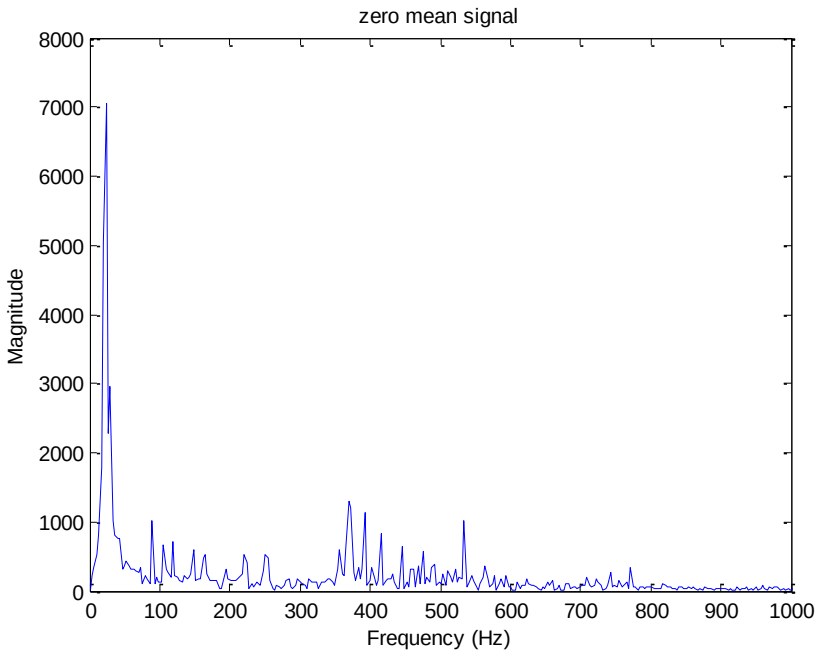

Figure 5.38: Magnitude of FFT amplitudes for ground reaction force

5.3.9 Shear modulus of Mooney Rivlin material model for the spoke is increased by 25%

From Figure 5.39 and Figure 5.40, the average length of the spokes is 83.8862 mm. The peak amplitudes occur at frequencies of 206 and 389 Hz. The RMS of FFT amplitudes of perpendicular distance for the middle node is 1.3502.

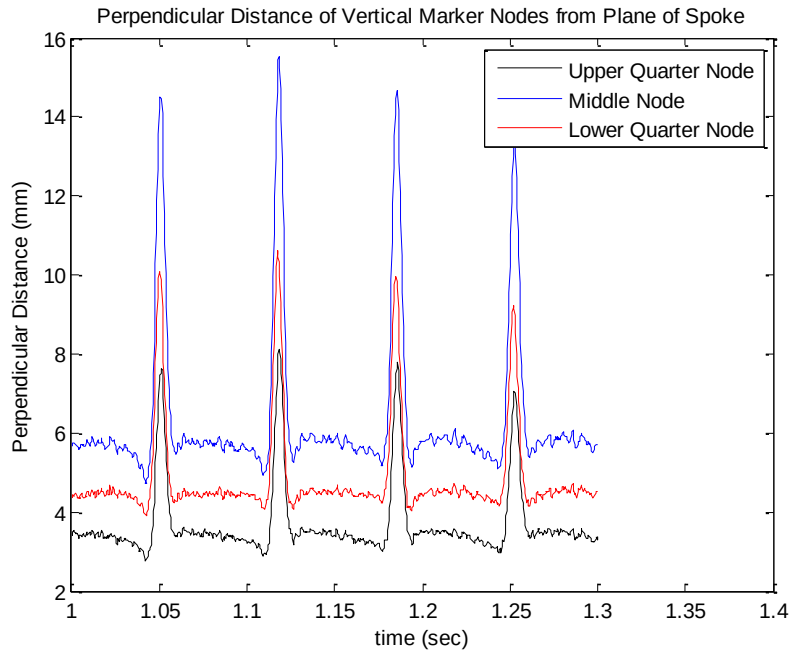

Figure 5.39: Perpendicular distance of the vertical spoke marker nodes from the plane of spoke

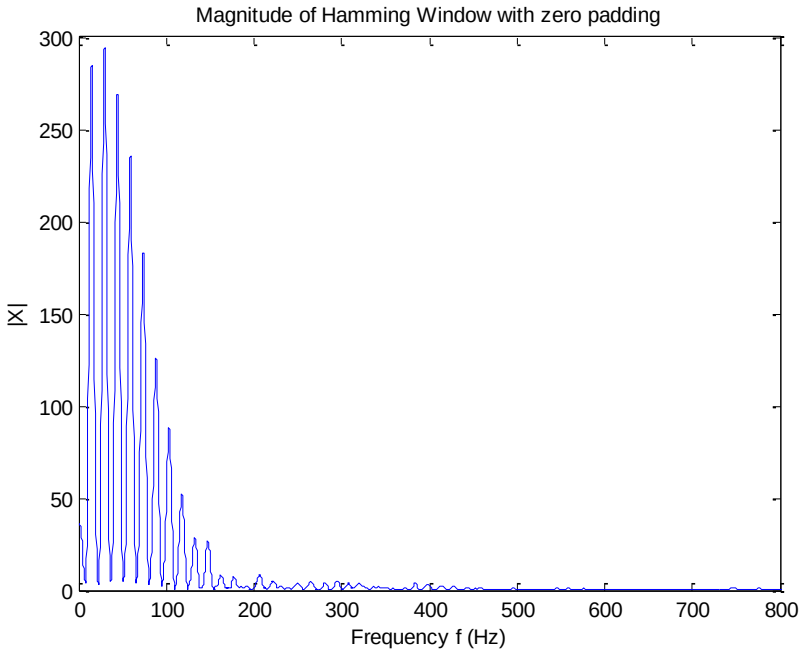

Figure 5.40: Magnitude of FFT amplitudes of perpendicular distance for the middle node

In Figure 5.41, the average ground reaction force is 366.3405 daN. In Figure 5.42the peak amplitudes occur at frequencies of 369, 561 and 712 Hz. The RMS of FFT amplitudes for ground reaction force is 101.

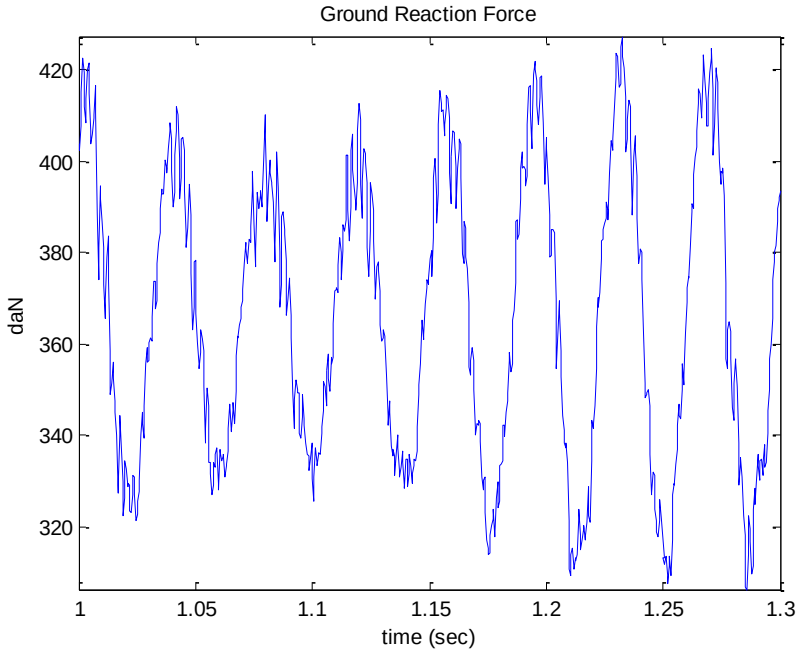

Figure 5.41: Ground reaction force

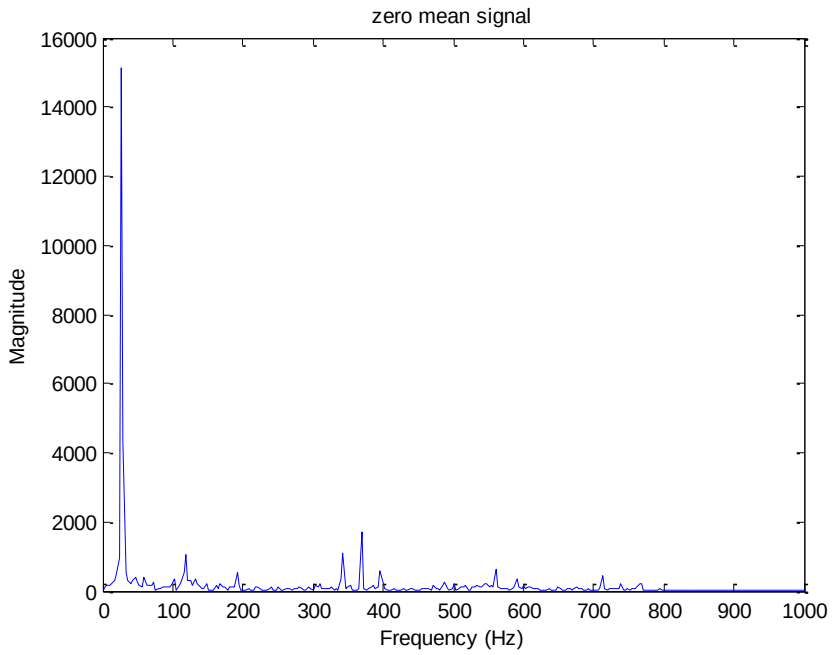

Figure 5.42: Magnitude of FFT amplitudes for ground reaction force

5.3.10 Shear modulus of Neo Hookean material model for the spokes remains unchanged

In Figure 5.43, the average length of the spokes is 83.8297 mm. From Figure 5.44, the peak amplitudes occur at frequencies of 208 and 402 Hz. The RMS of FFT amplitudes of perpendicular distance for the middle node is 16.0285.

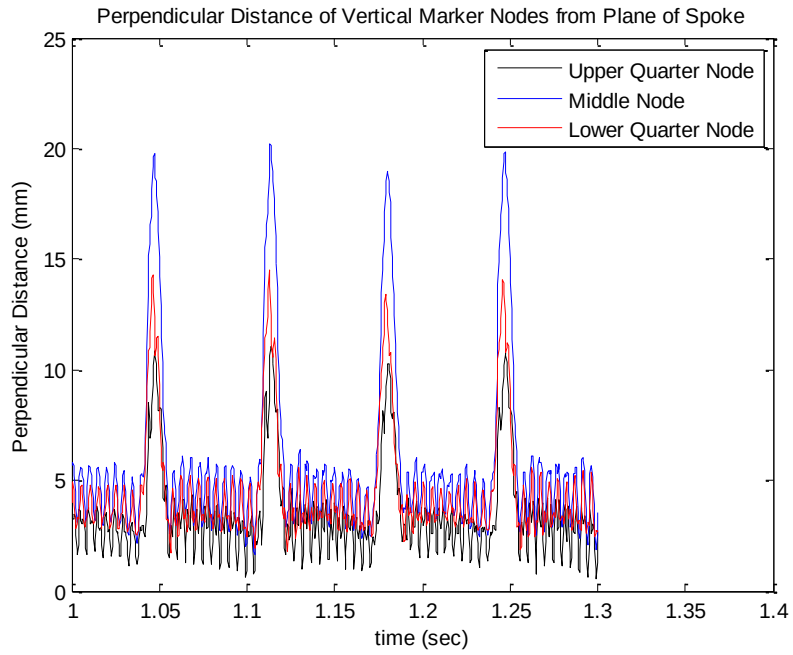

Figure 5.43: Perpendicular distance of vertical spoke marker nodes from the plane of spoke

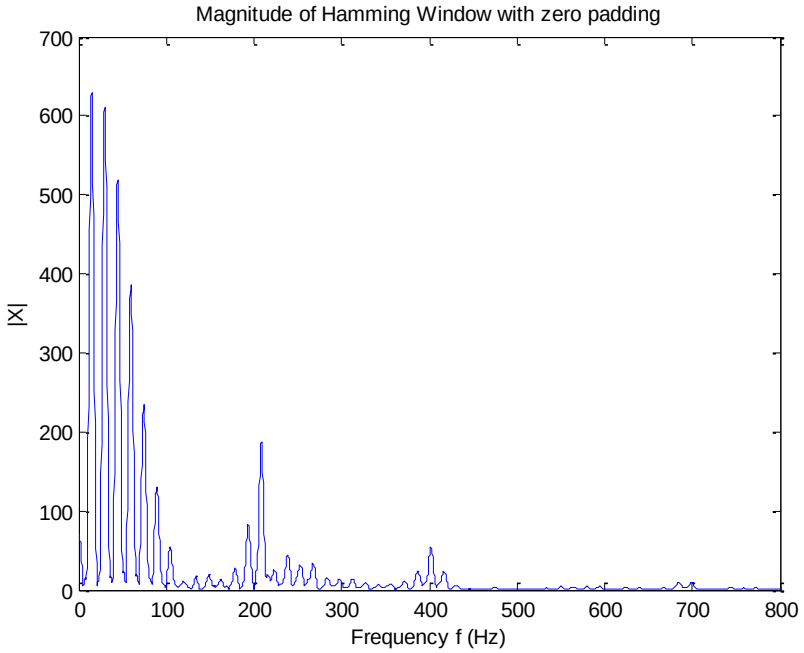

Figure 5.44: Magnitude of FFT amplitudes of the perpendicular distance for the middle spoke

For ground interaction, from Figure 5.45, the average ground reaction force is 366.6618 daN. In Figure 5.46, the peak amplitudes occur at frequencies of 372 and 764 Hz. The RMS of FFT amplitudes for ground reaction force is 801.

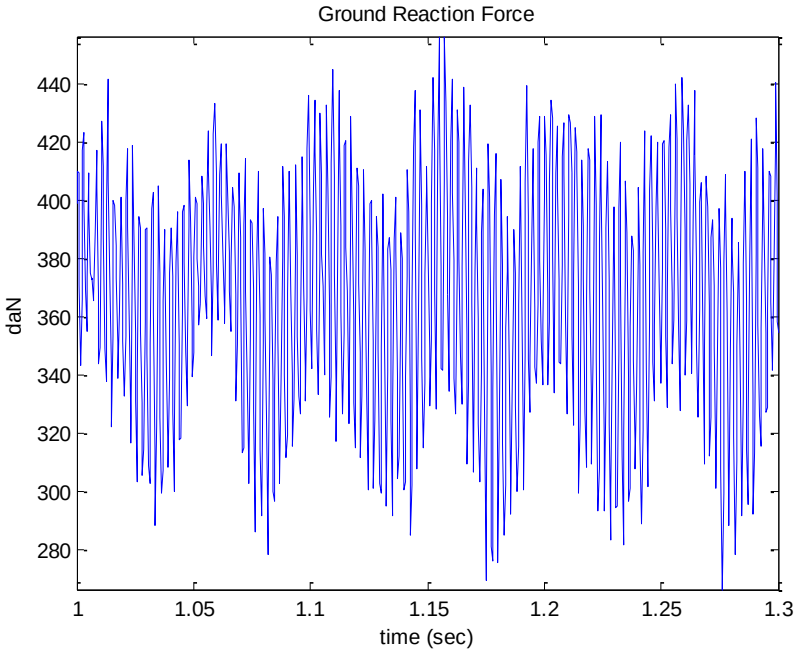

Figure 5.45: Reaction force exerted by the ground on the Tweel

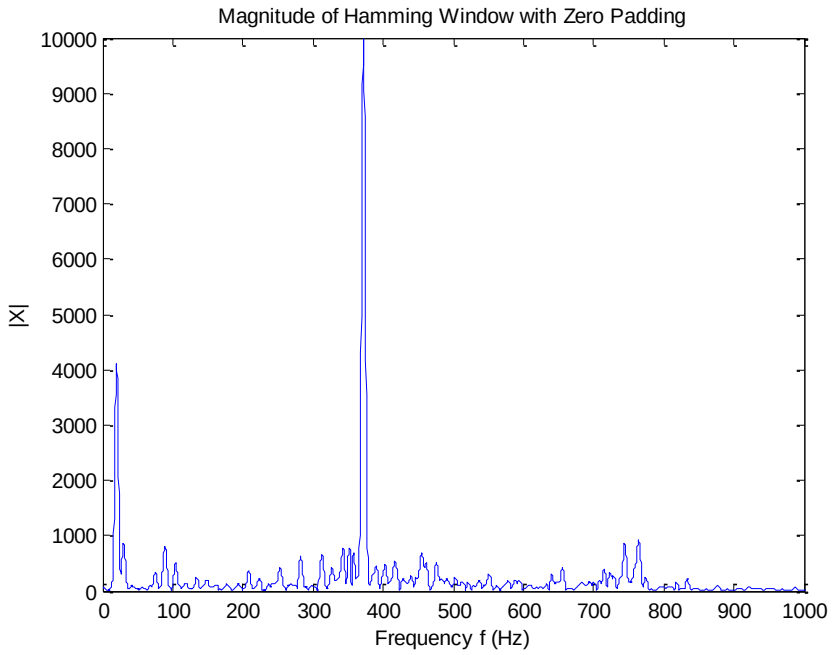

Figure 5.46: Magnitude of FFT amplitudes for ground reaction force

5.3.11 Shear modulus of the Neo Hookean model for the spokes is reduced by 25%

From Figure 5.47 and Figure 5.48, the average length of the spoke is 83.7442 mm. The RMS of FFT amplitudes of perpendicular distance for the middle node is 5.9097. The peak amplitude occurs at a frequency of 360 Hz.

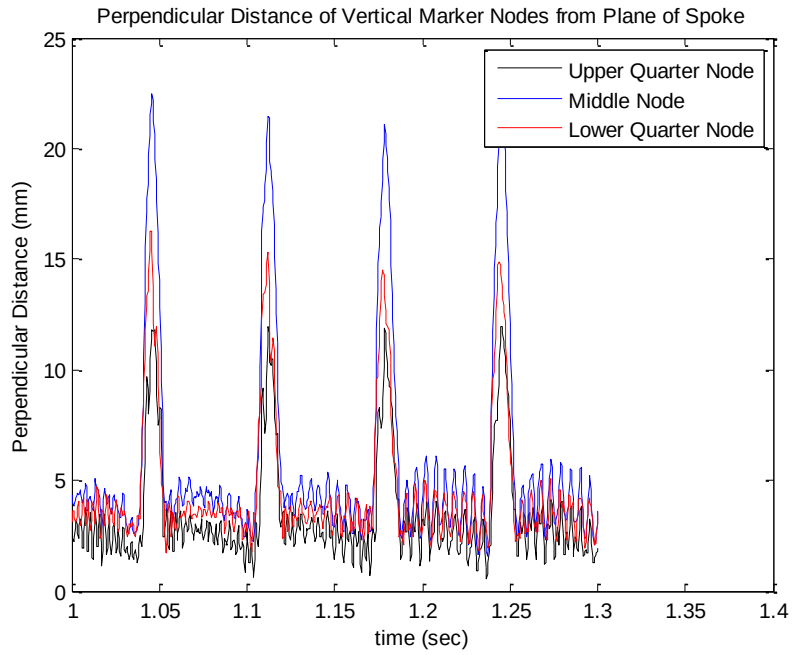

Figure 5.47: Perpendicular distance of the vertical marker nodes from plane of spoke

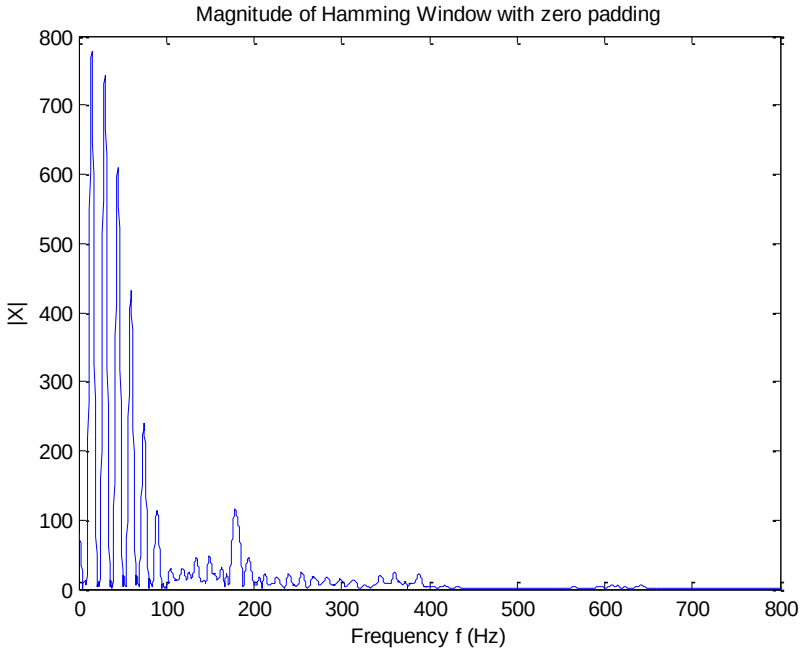

Figure 5.48: Magnitude of FFT amplitudes of perpendicular distance for the middle node

For the ground interaction, in Figure 5.49, the average ground reaction force is 365.0709 daN. In Figure 5.50, the peak amplitudes occur at frequencies of 374 and 746 Hz. The RMS of FFT amplitudes for ground reaction force is 472.

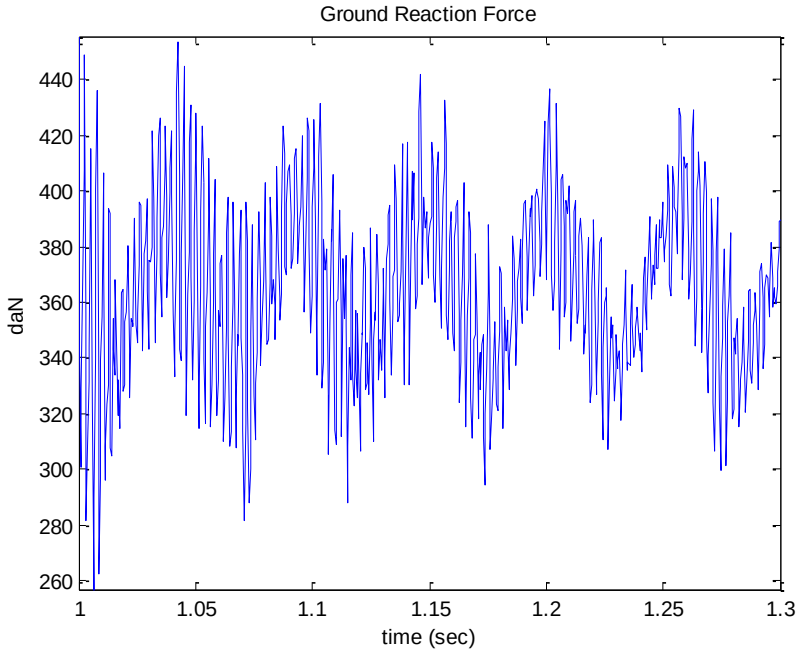

Figure 5.49: Ground reaction force

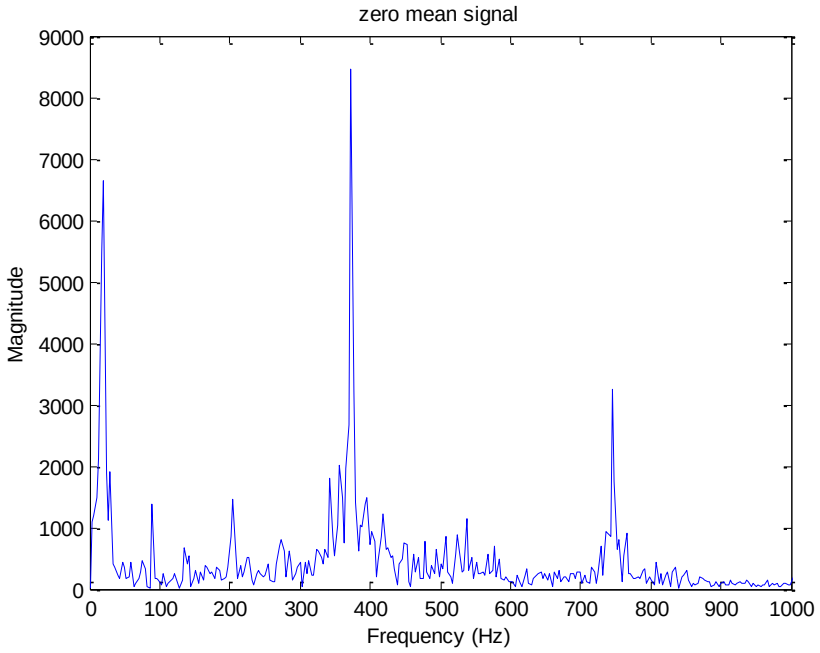

Figure 5.50: Magnitude of FFT amplitudes for ground reaction force

5.3.12 Shear modulus of Neo Hookean model for the spokes is increased by 25%

In Figure 5.51 and Figure 5.52, for spoke vibration, the average length of the spokes is 83.9044 mm. The peak amplitudes occur at frequencies of 238 and 282 Hz. The RMS of the FFT amplitudes of perpendicular distance for the middle node is 3.757.

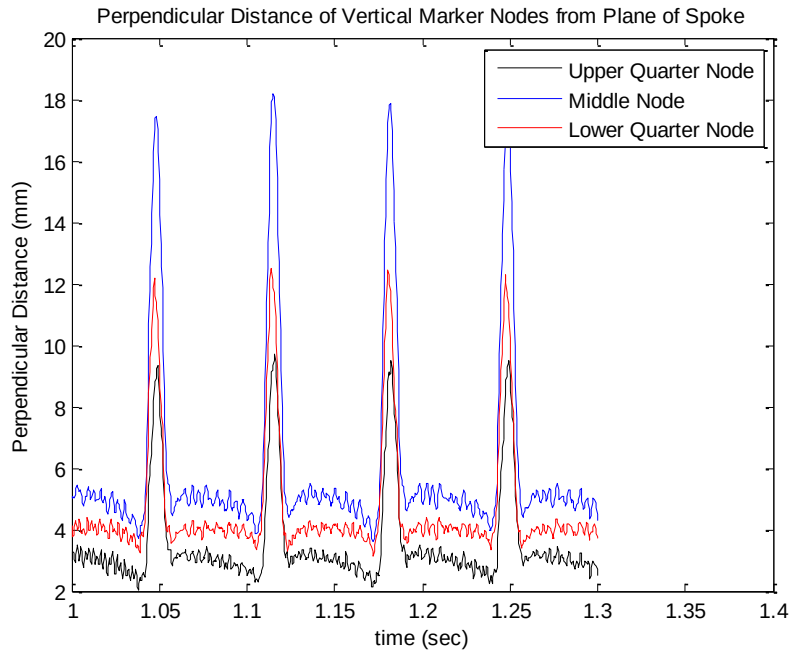

Figure 5.51: Perpendicular distance of the vertical spoke marker nodes

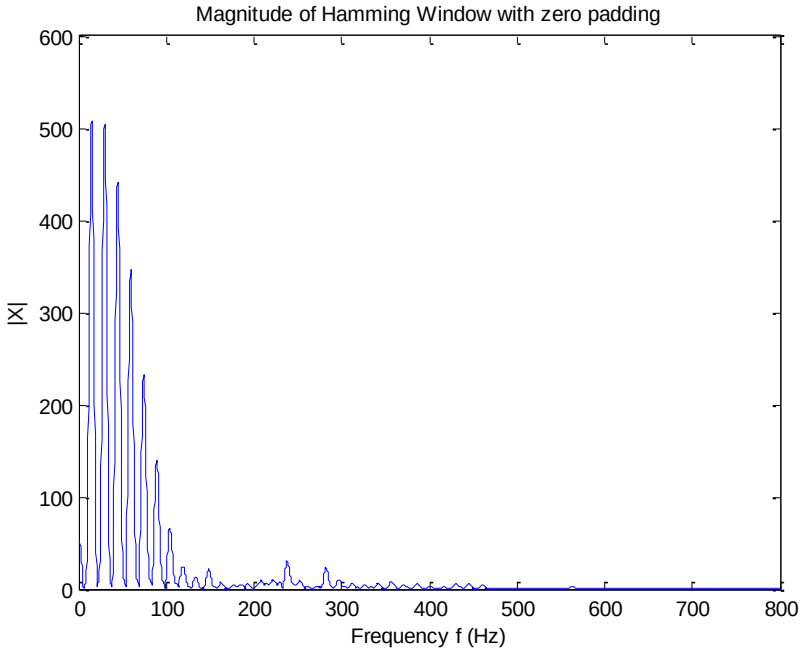

Figure 5.52: magnitude of FFT amplitudes of perpendicular distance for the middle node on the spoke edge

For ground interaction, in Figure 5.53, the average ground reaction force is 365.7203 daN. In Figure 5.54, the peak amplitudes occur at frequencies of 371, 484 and 764 Hz. The RMS of FFT amplitudes for the ground reaction force is 204.

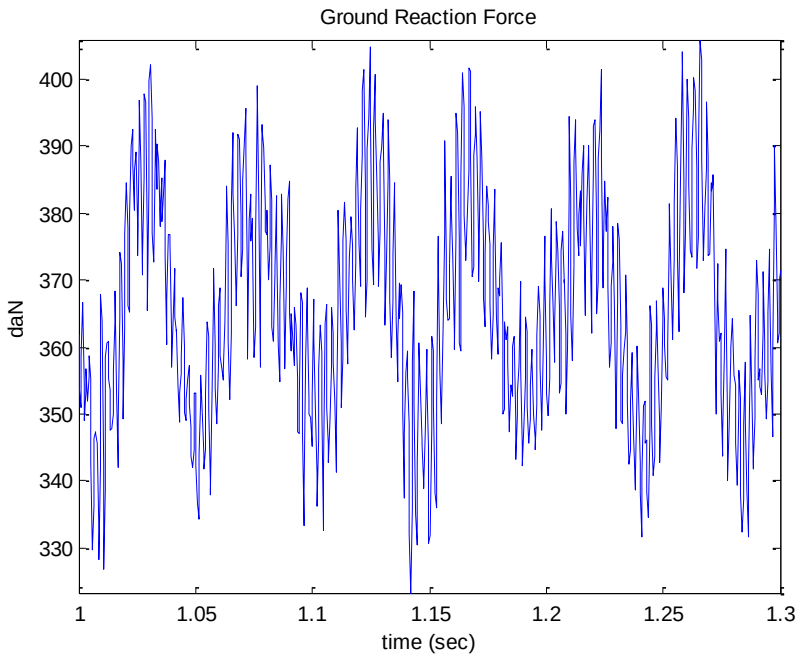

Figure 5.53: Reaction force exerted by the ground on the Tweel

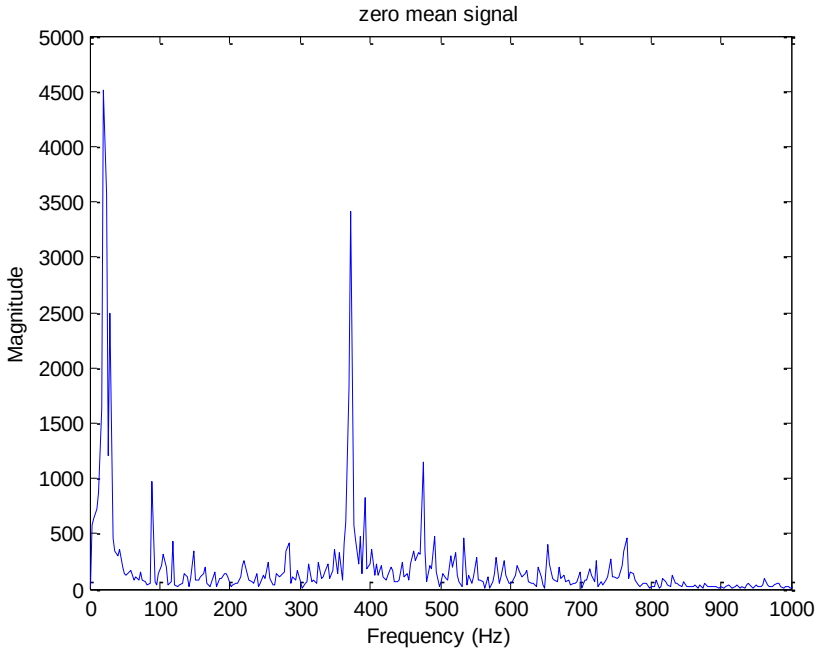

Figure 5.54: Magnitude of FFT amplitudes for ground reaction force.

5.4 Observations

In this section, the RMS values of the FFT amplitudes for spoke vibration and ground interaction vibration summarized and compared in this section. Four bar charts have been provided for both spoke vibration and ground vibration.

5.4.1 Comparison of RMS values of FFT amplitudes for Spoke Vibration

In Figure 5.55, there are two sets of RMS values. The first set 'Ring' refers to the Tweel models with unchanged Mooney Rivlin and unchanged Neo Hookean models for the ring. Likewise, 'Spoke' refers to the Tweel models with unchanged Mooney Rivlin and unchanged Neo Hookean models for the spokes.

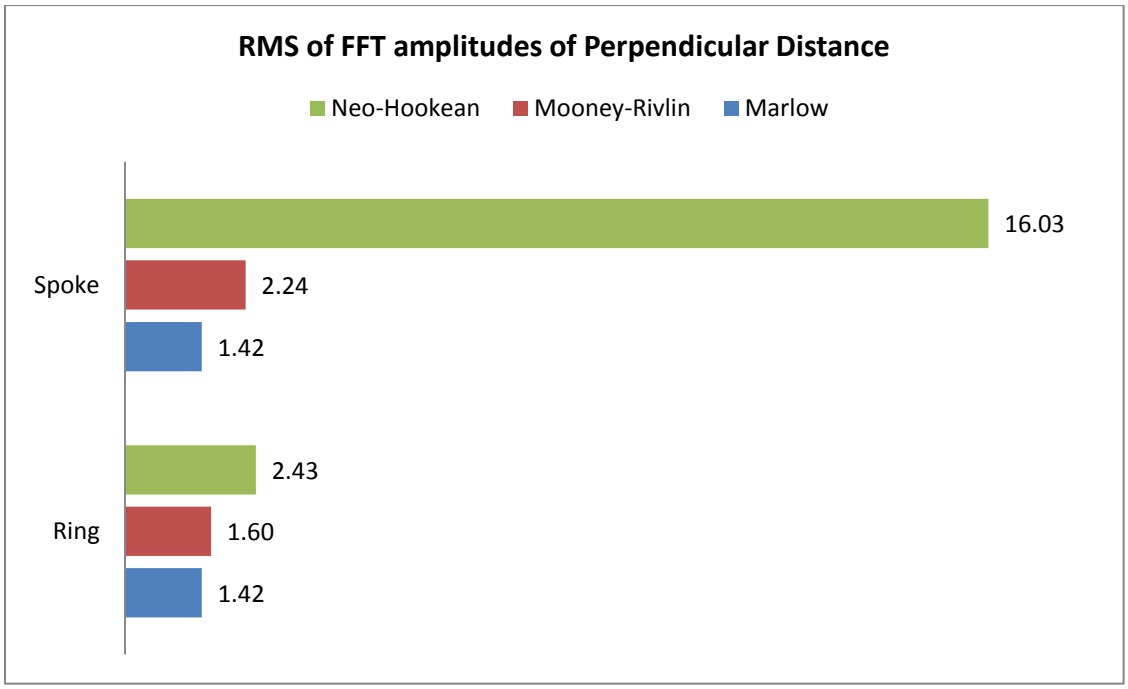

Figure 5.55: RMS of FFT amplitudes of perpendicular distance from virtual spoke plane for reference and unchanged models

The RMS of FFT amplitude for the reference Marlow model is 1.42. When an unchanged Mooney Rivlin material model was used for the ring instead of Marlow, the RMS value increased to 1.60. The RMS of FFT amplitude further increased to 2.43 when an unchanged Neo Hookean material model was used for the ring instead of Marlow.

Similarly, when an unchanged Mooney Rivlin material model was used for the spokes, the RMS value increased from 1.42 to 2.24. There was a drastic increase in the RMS value when an unchanged Neo Hookean material model was used for the spokes. The RMS value increased to 16.03.

The general trend shown is that the vibration amplitude in the spokes increases when the Marlow properties are changed to either the fitted Mooney Rivlin or Neo Hookean models, with the Neo Hookean model giving the largest vibration amplitudes, especially in the case of changes in spoke properties. It also appears from these results that changes to spoke material properties have a more significant influence on spoke vibration when compared to changes in ring properties.

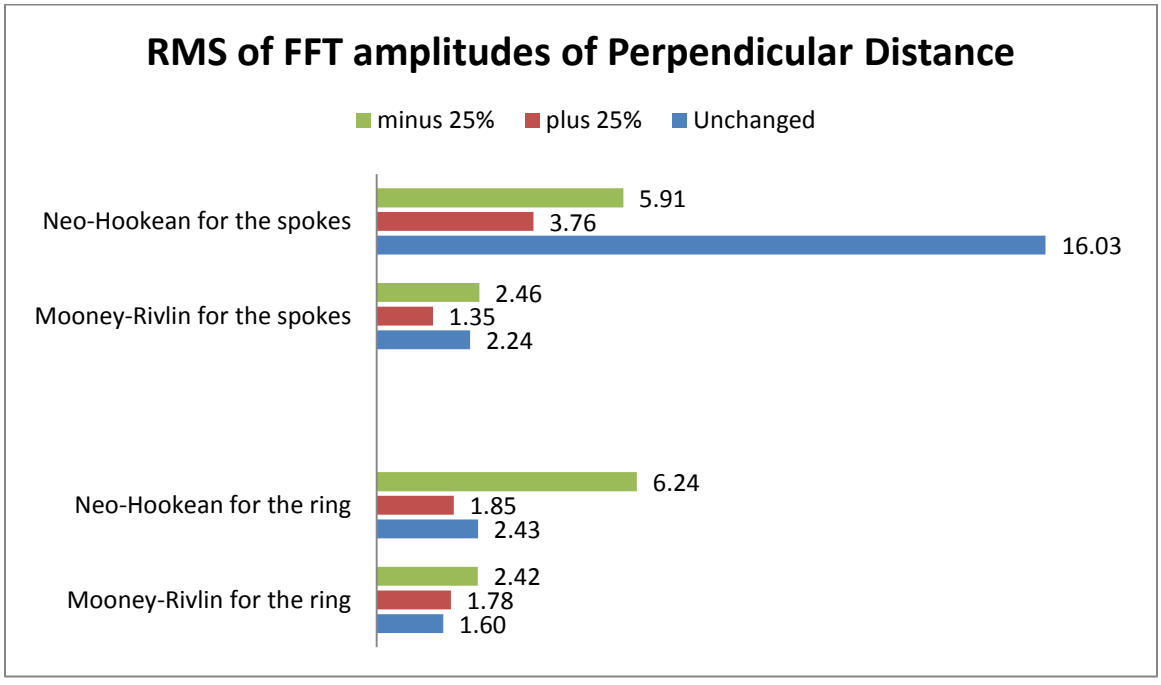

Figure 5.56: RMS of FFT amplitudes for different Mooney Rivlin and Neo Hookean models

In Figure 5.56, four sets of RMS values have been provided. ‘Mooney Rivlin for the ring’ refers to all the Tweel models with different Mooney Rivlin models for the ring. A similar explanation can be given for the rest of the 3 sets of RMS values.

When a Mooney Rivlin model with reduced shear modulus for the ring was used, the RMS value increased to 2.42 from 1.60. The RMS value increased to 1.78 from 1.60 when a Mooney Rivlin with increased shear modulus for the ring was used.

When Neo Hookean material models were used for the ring, the RMS value for the Tweel model with an unchanged Neo Hookean model was 2.43. When the shear modulus was increased by 25%, the RMS value reduced to 1.85. But when the shear modulus was reduced to 25%, the RMS value increased to 6.24.

On changing the spoke material models to Mooney Rivlin, the Tweel model with an unchanged Mooney Rivlin model for the spokes had a RMS value of 2.24. When the shear modulus was reduced by 25%, the RMS value increased to 2.46. When the shear modulus was increased by 25%, the RMS value reduced to 1.35 from 2.43.

Finally, when Neo Hookean material models were used for the spoke, the Tweel model with an unchanged Neo Hookean material model had a RMS value of 16.03. But when the shear modulus was reduced by 25%, the RMS value decreased 5.91. The RMS value dropped further down to 3.75 when the shear modulus was increased by 25%.

A general trend found in these results when comparing the extreme limits of plus and minus 25% change, is that when the shear modulus is decreased, the spoke vibration increases. Conversely, when the shear modulus is increased from -25% to +25%, the spoke vibration decreases. However, it should be noted that in the case of the unchanged

Mooney Rivlin model for the ring, the unchanged gave the smallest amplitude when compared to both the plus and minus extreme limits tested, thus implying that there is an optimal value somewhere between the limits. Another instance where an optimal value occurs can be seen in the Neo Hookean model for the spokes, where the unchanged spoke vibration amplitude was higher than both the plus and minus stiffness limits. Note also that the unchanged Neo Hookean model for the spokes had the largest amplitude when compared to all models. However, it should be noted that in the case of the unchanged Mooney Rivlin model for the ring, the unchanged gave the smallest amplitude when compared to both the plus and minus extreme limits tested, thus implying that there is an optimal value somewhere between the limits. Another instance where an optimal value occurs can be seen in the Neo Hookean model for the spokes, where the unchanged spoke vibration amplitude was higher than both the plus and minus stiffness limits. Note also that the unchanged Neo Hookean model for the spokes had the largest amplitude when compared to all models.

5.4.2 Comparison of RMS values of FFT amplitudes for Ground Interaction Vibration

In Figure 5.57, two sets of RMS values have been provided. Similar to the spoke vibration, ‘Ring’ refers to all the Tweel models with unchanged Mooney Rivlin and Neo Hookean models for the ring instead of Marlow. A similar explanation can be given for the second set named ‘Spoke’.

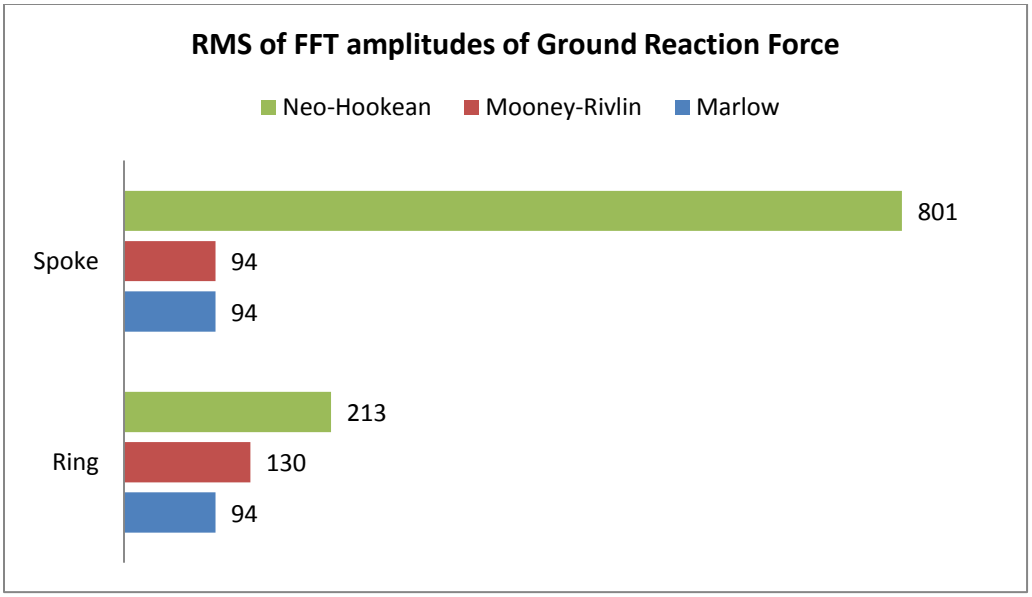

Figure 5.57: RMS of FFT amplitudes of ground reaction force for reference and unchanged models

For the reference Tweel model, the RMS value of the FFT amplitude for ground reaction force was recorded to be 94. The RMS value of FFT amplitude increased to 130 when the material for the ring was changed to an unchanged Mooney Rivlin material model. The RMS value further increased to 213 when the material was changed to an unchanged Neo Hookean material model.

When an unchanged Mooney Rivlin material model was used for the spokes, the RMS value remained at 94. But when an unchanged Neo Hookean model was used for the spokes, the RMS value increased to 801 from 94.

These results show changing the material model to Neo-Hookean from Marlow increases the ground force vibration amplitude. The Moony Rivlin model increases vibration amplitude compared to Marlow but is less than Neo Hookean.

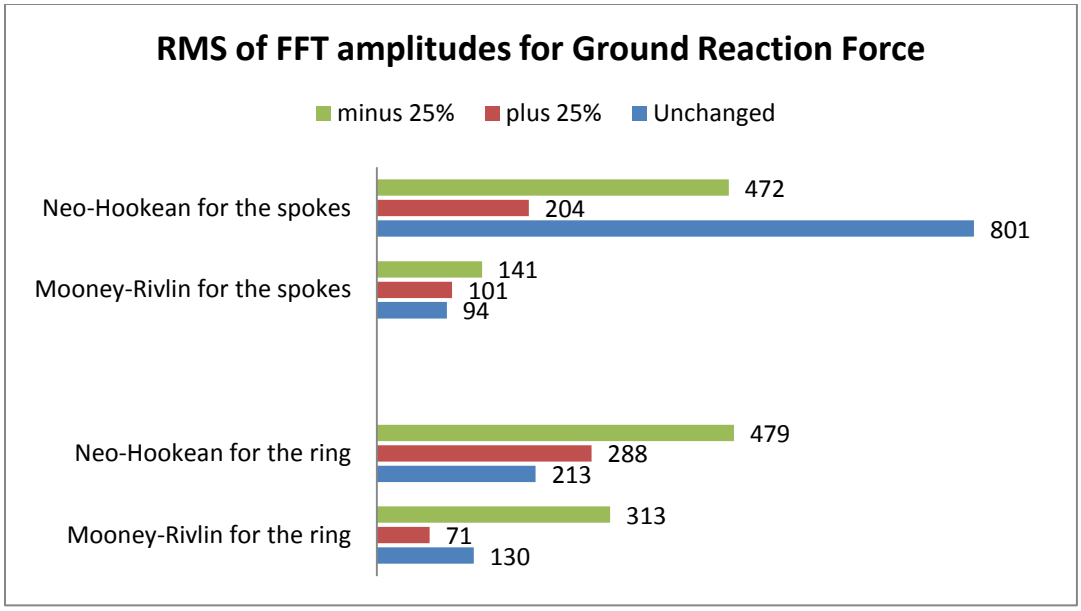

Figure 5.58: RMS of FFT amplitudes for different Mooney Rivlin and Neo Hookean models

In Figure 5.58, four sets of RMS values have been provided. In the first set, the material for the ring is changed to an unchanged, reduced and an increased Mooney Rivlin model. A similar explanation is valid for the other three sets.

When Mooney Rivlin is used for the ring, the RMS for the unchanged model was 130. The RMS value for the Tweel with a Mooney Rivlin model whose shear modulus is reduced by 25% increased to 313 from 130. But when the shear modulus is increased by 25%, the RMS value of the FFT amplitudes decreased to 71.

Considering Neo Hookean for the ring, the unchanged model had a RMS value of 213. When the shear modulus is reduced by 25%, the RMS value increased to 479. The RMS value increased to 288 when the shear modulus was increased by 25%.

When Mooney Rivlin was used for the spokes, the RMS value for the unchanged model was recorded to be 94. When the shear modulus was reduced by 25%, the RMS

value increased to 141 from 94. But when the shear modulus was increased by 25%, the RMS value increased to 101 from 94.

Considering Neo Hookean for the spokes, the unchanged model's RMS value was 801. When the shear modulus was reduced by 25%, the RMS value decreased to 472 from 801. The RMS value further decreased to 204 from 801 when the shear modulus was increased by 25%.

The results show that decreasing the shear modulus to -25% increased ground force vibration compared to unchanged and increased modulus. Increasing the shear modulus increased the ground force vibration when compared to unchanged Mooney-Rivlin for the spokes and Neo-Hookean for the ring but decreased vibration in the other cases. Similar to the spoke vibration, the Neo Hookean unchanged for the spokes gives the largest vibration amplitude.

CHAPTER SIX- EFFECTS OF CHANGING MATERIAL PROPERTIES ON ENERGY LOSS FROM IMPACT ROLLING OVER OBSTACLES

In Chapter One, the four critical characteristics of the pneumatic tire identified in [1] have been explained. A major advantage of the pneumatic tire over a rigid wheel comes from its behavior when traversing obstacles. In [1], it was shown that a pneumatic tire gave less Kinetic energy loss when compared with a rigid wheel with the same mass and moment of inertia properties when rolled over an obstacle. In [1], a particular Tweel™ model with the same secant stiffness at the applied load, mass, moment of inertia and initial velocity as a typical pneumatic wheel model was constructed. Upon rolling the Tweel and the pneumatic tire over an obstacle, it was seen that the reduction in hub velocity of the Tweel after impacting the obstacle was lesser than the pneumatic tire. For this study, the radius used was 0.1 m and the height of the obstacle was 0.0125 m, resulting in an obstacle height of 12.5% of the radius. This set-up is represented in **Error! Reference source not found.**.

For this configuration, the theoretical reduction in hub velocity for a rigid cylinder is 16% as shown in Figure 6.2. It was found that the reduction in velocity for the pneumatic tire and the Tweel simulations were 6% and 3.2% respectively as shown in Figure 6.3. The horizontal velocity corresponds to the proportion of energy lost due to impact. The analysis was completely an elastic simulation which explains the bouncing seen on the graphs after the Tweel impacts the ground after traversing the obstacle. In the study presented in [1], details of the Tweel model such as type of spokes used, curvature

of spokes, number of spokes, thickness of ring, and material properties were not cited. In addition, the particular geometric dimensions of the obstacle, other than the height, were not reported.

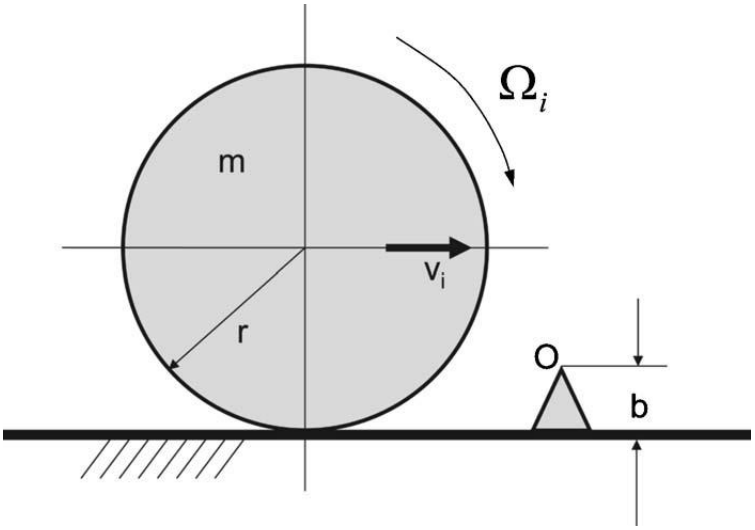

Figure 6.1: Rigid Wheel traversing an obstacle.

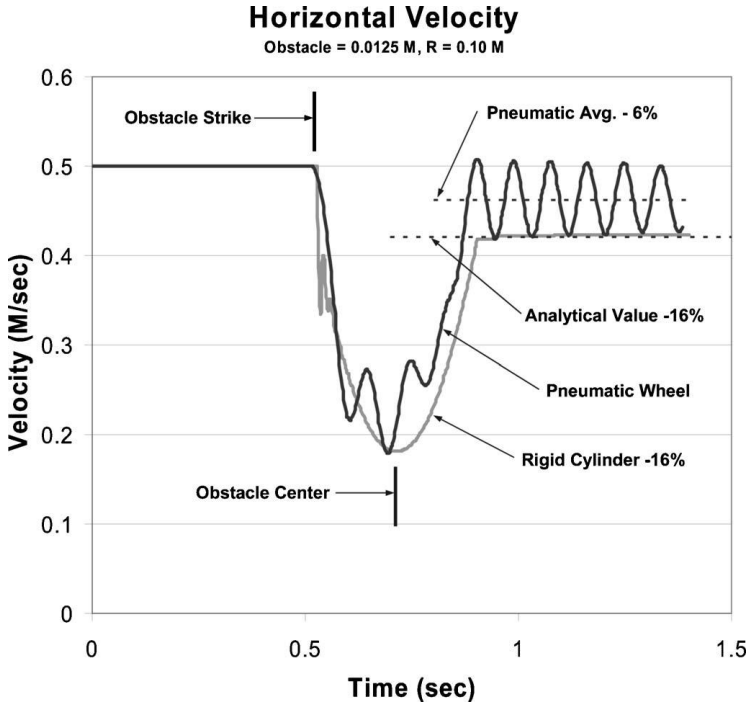

Figure 6.2: Horizontal velocity profile for the rigid wheel and the pneumatic wheel from [1, 14]

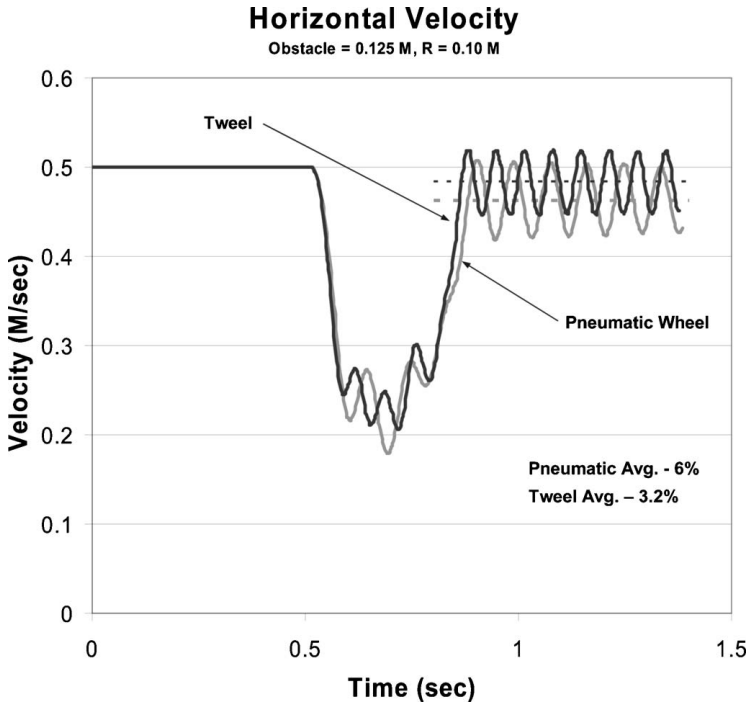

Figure 6.3: Horizontal velocity profile for the pneumatic wheel and the Tweel from [1, 14]

In this Chapter, the objective is to compute energy loss of the current 3D Tweel finite element model by rolling it over an obstacle with specified height on the ground. This is done by studying and comparing the reduction in axial hub velocities and the proportion of kinetic energy loss of the 3D Tweel model compared with an analytical rigid cylinder with the same mass, moment of inertia, and initial velocity. Proportion of Kinetic energy loss and percentage reduction in velocity after traversing the obstacle gives less change in linear momentum, implying reduced linear impulse, which in turn leads to reduced harshness over rough surfaces. Results of the 3D Tweel model are compared with a rigid wheel finite element model having the same mass, outside radius, and moment of inertia as that of the Tweel. An analytical model of the rigid wheel with a simplified analysis of

the obstacle is also developed and is compared with FEA models of both the Tweel and rigid wheel.

In order to study the effects of changes in Tweel stiffness on the amount of energy loss, changes in hyperelastic material models with increase and decrease in shear modulus described in earlier Chapters is presented. A material study is performed to compare these parameters for the Tweel model with changing materials for the ring and the spoke. For this study, rolling resistance is not of interest, thus viscoelastic properties for the rubber tread are not included in the model.

6.1 Theoretical Speed Reduction and Energy Loss for a Rigid Wheel Traversing an Obstacle

In theory, the kinematics and kinetics of a rigid wheel rolling over an obstacle is considered for evaluating the loss of energy and reduction in axial velocity when the wheel hits and overcomes the obstacle of specified height. The following analysis follows the discussion in [1] and [18].

Consider a rigid cylinder of mass *m*, rolling across the ground with a constant initial velocity V_i. When a rigid wheel of mass 'm' and radius 'R' is rolling over an obstacle of height 'b', it is assumed that the ground is rough, i.e. no slip takes place, and no rebound occurs at impact. In other words, the coefficient of restitution is zero which makes the type of impact to be inelastic. Another important assumption is that the time of impact is considered to be small so that non-impulsive forces can be neglected. This conserves the angular momentum of the rigid wheel about point the point of initial

impact, denoted pt. O in Figure 6.1. Taking these assumptions into consideration, and using conservation of angular momentum about the contact point, the speed just after the initial impact is obtained. Using work energy principles, and conservation of angular momentum about the second impact when the wheel impacts the ground after pivoting over the obstacle, an expression can be derived for the final velocity of the rigid wheel after completely transversing the obstacle (see Appendix).

$$V_f = \left[1 - C\left(\frac{b}{R}\right)\right]^2 V_i$$

where, $C = 1/((k_G / R)^2 + 1)$, and $k_G = \sqrt{I_z / m}$, V_f is the final velocity after impact, V_i is the velocity before impact, b is the height of the obstacle and R is the radius of the wheel. This theoretical value for final velocity will be used to compare with the values which will be obtained in the numerical simulations. Given the initial velocity, the radius of the rigid wheel and the height of the obstacle, the final velocity after impact can be calculated. Using the expression for final velocity in terms of initial velocity, the expression for proportion of kinetic energy lost due to an impact of the rigid wheel over an obstacle is given as (see Appendix)

$$\frac{\Delta E}{E_i} = 1 - \left[1 - C\left(\frac{b}{R}\right)\right]^4$$

where E_i is the initial kinetic energy and $\Delta E = E_i - E_f$, is the energy loss. The different parameters used to calculate the proportion of energy lost due to impact and the final velocity of the rigid wheel after impact is given in the form of a table below.

Table 6-1: Parameters for analysis of energy loss rolling over the obstacle

Initial axial hub velocity, V_i	3000 mm/sec
Vertical Load	366.5 daN
Outer Radius, R	303.28 mm
Obstacle height, b	22.5 mm
Moment of Inertia, I_z	1.150345 kg-m^2
Mass, m	15.4814 kg
Ratio of height of obstacle to the radius of the rigid wheel, *b/R*	0.074

From these set of parameters, the theoretical final velocity for a rigid wheel is be calculated as 2758.8 mm/s. This results in a percentage relative reduction in axial hub velocity of 8.04%.

The theoretical kinetic energy of the rigid wheel is a sum of two components. The first component is the translational kinetic energy due to the axial hub velocity V_i and the second component is the rotational kinetic energy due to the rotational velocity ω and the moment of inertia I_z. The analytical equation for the theoretical total initial energy is

$$E_{initial} = E_{translational} + E_{rotational} = \frac{1}{2} m V_i^2 + \frac{1}{2} I_z \omega^2$$

With no slip between the wheel and ground, the initial angular speed can be expressed by the kinematic relation, $\omega = V_i / R$. Using the parameters in the setup, the initial angular velocity is calculated to be 9.891 rad/sec. From the parameters listed above in Table 6-1, the total initial kinetic energy is $E_{initial}$ = 12593.7 dN-mm, and the energy lost due to impact over the obstacle is estimated to be $\Delta E / E_i$ = 15.43%. The final kinetic energy based on the proportion of energy lost is calculated as,

$$E_{final} = (1 - .1543) E_{initial} = 10651 \;\; dN - mm$$

6.2 Finite element model of the Rigid wheel

A finite element model which approximates a rigid wheel is created based on the parameters listed in Table 6-1. The model is constructed of a steel ring of the same dimensions as the ring in the Tweel model. The steel is modeled with an elastic modulus of $210000\ N/mm^2$ with a Poisson's Ratio of 0.3. The moment of inertia about the rotating axis I_z and the mass of the rigid wheel is the same as that of the TWEEL and analytical rigid wheel model. The density for the ring was adjusted so that the moment of inertia matched the Tweel, with an additional lumped mass added to the hub center to match the Tweel mass.

A kinematic coupling constraint is defined between the inner surfaces of the steel ring with a reference node at the center of the wheel such that the hub becomes rigid. The finite element model of the steel ring with rigid hub, denoted as "rigid wheel finite element model" is meshed such that it is discretized into 19200 elements with 8 elements across the thickness and 6 elements across the width of the wheel. The finite element model setup is shown below in Figure 6.4 and Figure 6.5.

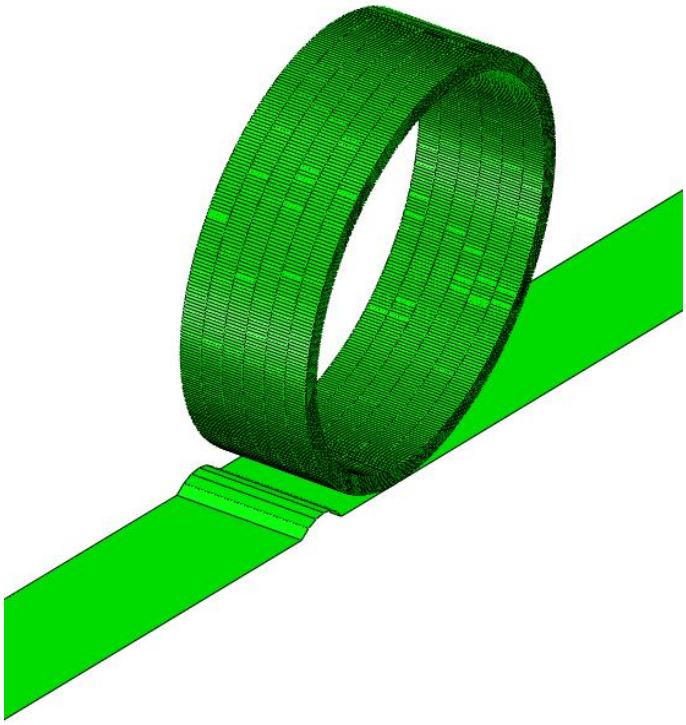

Figure 6.4: Finite element model of the rigid wheel

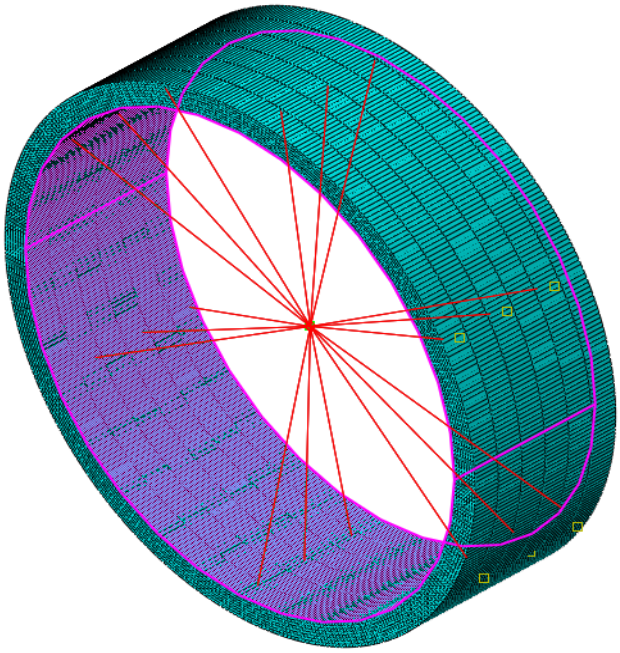

Figure 6.5: Enforcement of a kinematic coupling constraint to model rigid hub.

This simulation for the rigid wheel modeled a steel ring with rigid hub is performed in ABAQUS/Explicit. After applying the vertical load, and accelerating up to a speed of 3000 mm/sec, the wheel model is allowed to roll freely under its own momentum keeping the vertical load constant. The axial hub velocity time-history for the rigid model is shown in Figure 6.6. The drop in axial velocity is due to the rolling over the obstacle. On taking the average of the velocity values between t=1.27 and t=1.4, the final velocity after traversing the obstacle is calculated to be 2754.323 mm/s. When compared with the analytical rigid wheel final velocity of 2758.8 mm/s, the difference is only 0.16%, showing good agreement.

The kinetic energy of the finite element model of the rigid wheel is shown in Figure 6.7. On taking the average of the kinetic energy values between t=1.27 and t=1.4, the value is calculated to be 10661 dN-mm. When compared with the analytical rigid wheel model with value of 10651dN-mm, the difference in final kinetic energy is calculated as 0.09%.

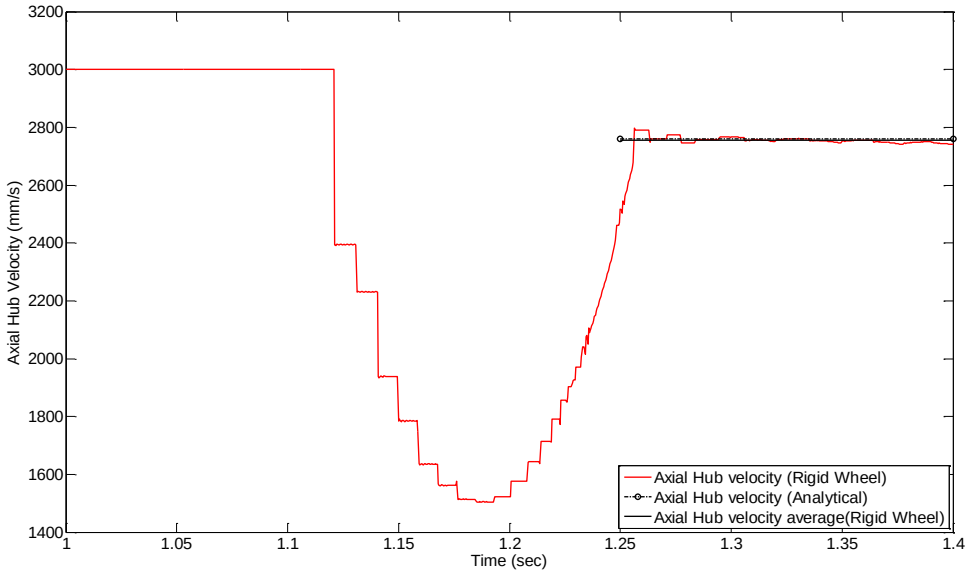

Figure 6.6: Comparison of the axial hub velocity of the finite element rigid wheel model based on a steel ring with the analytical model.

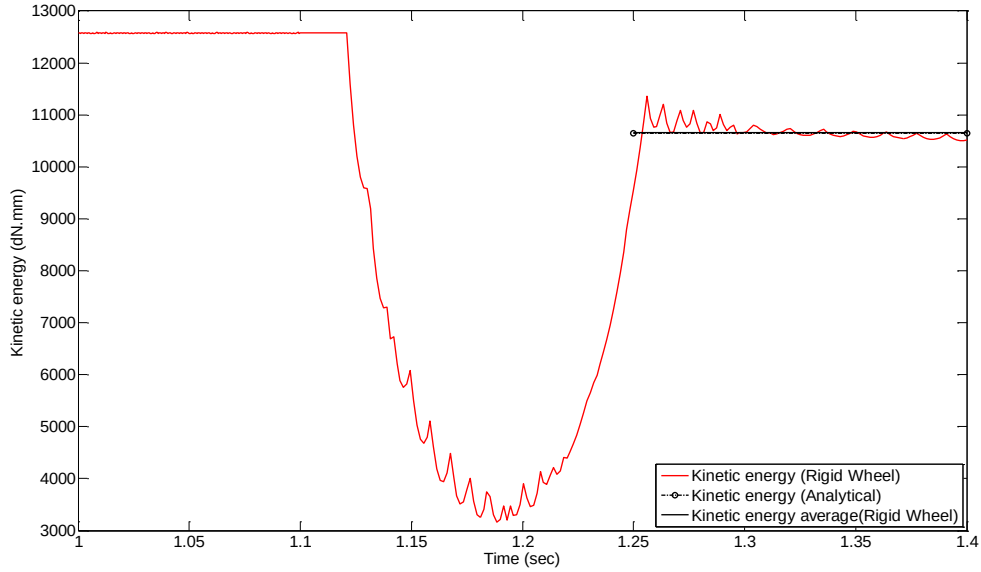

Figure 6.7: Comparison of the kinetic energy of the finite element rigid wheel model with the analytical model.

The conservation of energy states that time rate of change of kinetic energy and internal energy of a body of material is equal to the sum of the rate of work done by the surface and body forces [19]. This can be expressed as,

$$\frac{d}{dt}(E_K + E_U) = \dot{E}_{WF}$$

where E_K = kinetic energy, and E_U = internal energy, and E_{WF} = external work. The total internal energy can be split into an internal energy from for the material and viscous dissipation energy, such that $E_U = E_I + E_V$. The rate of change in external work can be defined in terms of the rate of change of work done by external forces, and the rate of energy dissipated by contact frictional forces between the contact surfaces, such that $E_{WF} = E_W - E_F$. An energy balance for the entire model can then be obtained by integrating the above equation:

$$E_{Total} = E_K + E_I + E_V + E_F - E_W = \text{constant}$$

From Figure 6.8, it is seen that the kinetic energy and external work of the rigid wheel finite element model increases during the acceleration step between 0 and 1.1 sec. After traversing the obstacle, the Kinetic Energy is reduced by 15%. To maintain a constant zero total energy as defined in the above equation, the loss in kinetic energy is accounted for by a corresponding increase in internal energy and to a lesser degree, frictional energy dissipation (minus work due to friction). This increase in the internal energy can be accounted for by the constrained elastic vibrations developed in the steel ring after impacting the obstacle and ground. Also, when the wheel impacts the obstacle, the energy due to frictional dissipation also starts to increase.

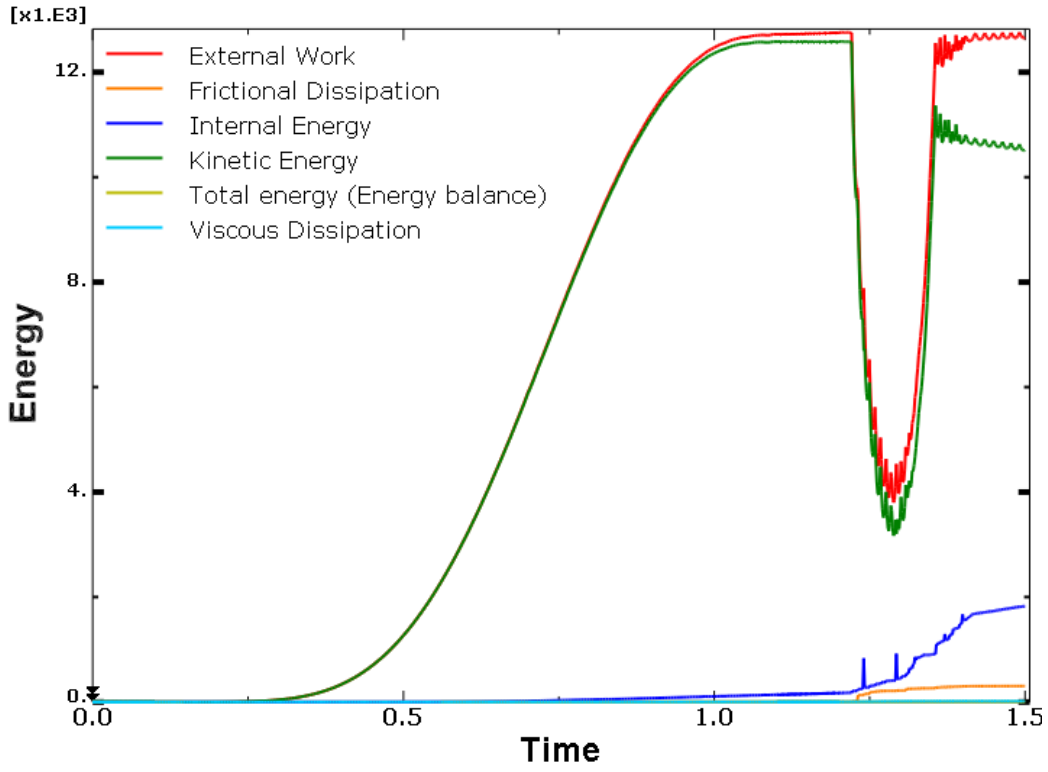

Figure 6.8: The different energies for the finite element steel ring with rigid hub model of the rigid wheel

6.3 Current 3D Finite Element Model of the TWEEL

From the rigid wheel analytical expressions for final velocity and change in energy, it is evident that these parameters depend only on the height of the obstacle and the radius of the wheel but not the shape of the obstacle. For the finite element analysis, an arc shaped obstacle is chosen over a sharp obstacle to avoid severe deformation of the Tweel and also to provide sufficient contact when traversing the obstacle. This can be related to a situation where the vehicle traverses over a bump on the road. This simulation is performed in ABAQUS/Explicit. Just before striking the obstacle, Tweel model is constrained only by the contact with the ground. This procedure can be related to a situation where the driver removes his/her foot from accelerator of the vehicle. This

makes the vehicle to cross the obstacle with the momentum gained from the previous step. The scenario created for a rigid wheel is replicated for the Tweel. The procedure and the boundary conditions used in this problem have been explained in Chapter Two. To set up the model, one should determine the distance travelled by the Tweel model during each analysis step. This distance can be calculated using fundamental equations of kinematics. Starting from rest during the constant acceleration during Step 1, the distance traveled is determined from

$$S_{step} = \frac{1}{2}(V_{final} - V_{initial})t_{step}$$

In the following, all dimensions are expressed in millimeters (mm). The velocity is defined in millimeters per second (mm/s).

In Step 1, the Tweel is accelerated to a final velocity of 3000 mm/s over a period of 1 second. The distance travelled in the first step is calculated to be 1500 mm. In Step 2, the Tweel is maintained at a constant velocity of 3000 mm/s (10.8 km/hr) for 0.1 seconds. The distance travelled in this step is 300 mm. In Step 3, the Tweel model is now free to roll with the momentum gained from the previous step for a time period of 0.4 seconds. Since the deceleration of the Tweel is not known a priori when it traverses the obstacle, the analytically rigid ground is created such that there is sufficient distance for the Tweel to travel. A safe total of 5000 mm is estimated to be the length of the ground. This setup is shown in Figure 6.9, Figure 6.10 and Figure 6.11.

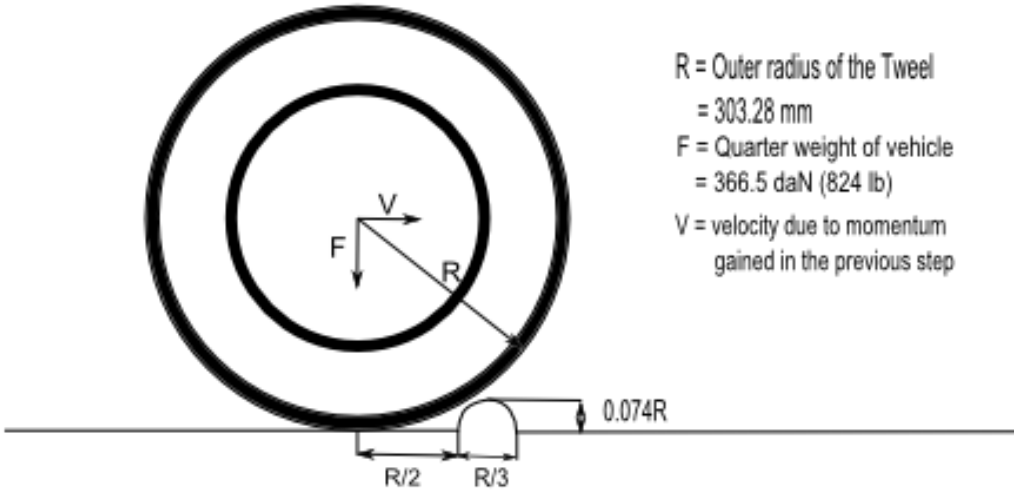

Figure 6.9: Analysis set up for Tweel rolling over rigid obstacle of height b = 0.074 R.

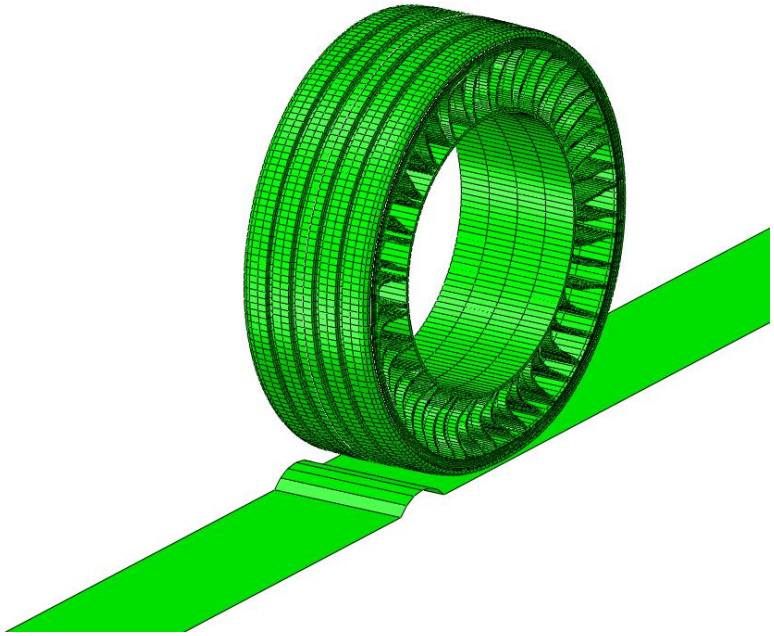

Figure 6.10: Analysis set up of the 3D Tweel finite element model rolling over an obstacle

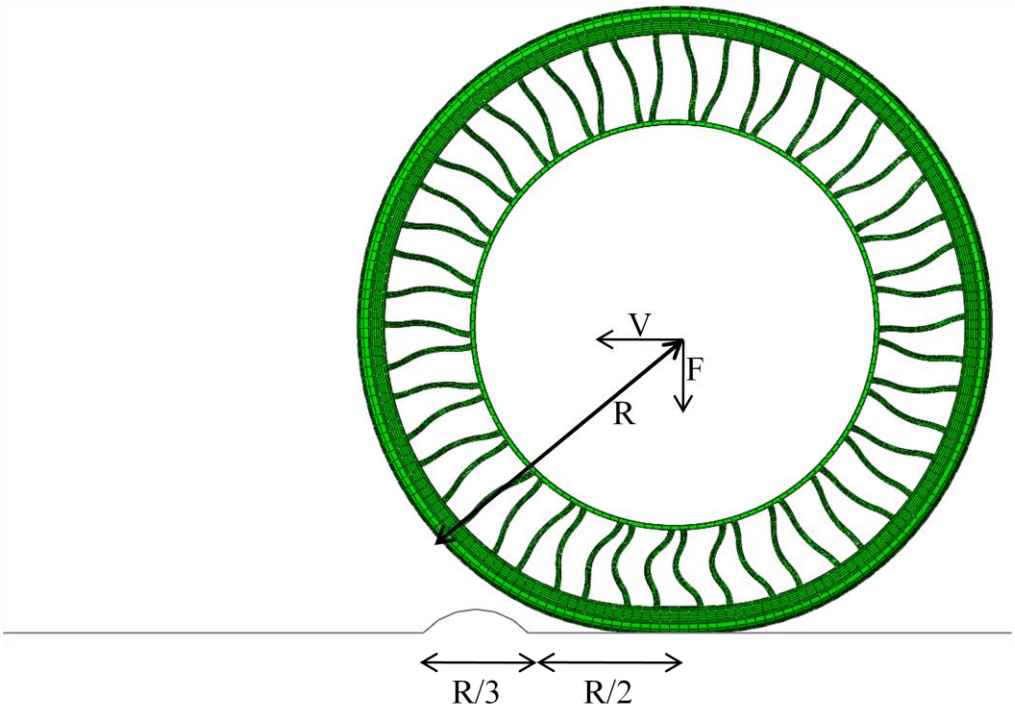

Figure 6.11: XY view of the Finite Element model setup

6.4 Results during obstacle impact

The Reference Tweel model considered for this analysis is a three dimensional Tweel with Marlow properties for both the ring and the spokes.

Figure 6.12 and Figure 6.13 show the Tweel model during initial impact with the obstacle.

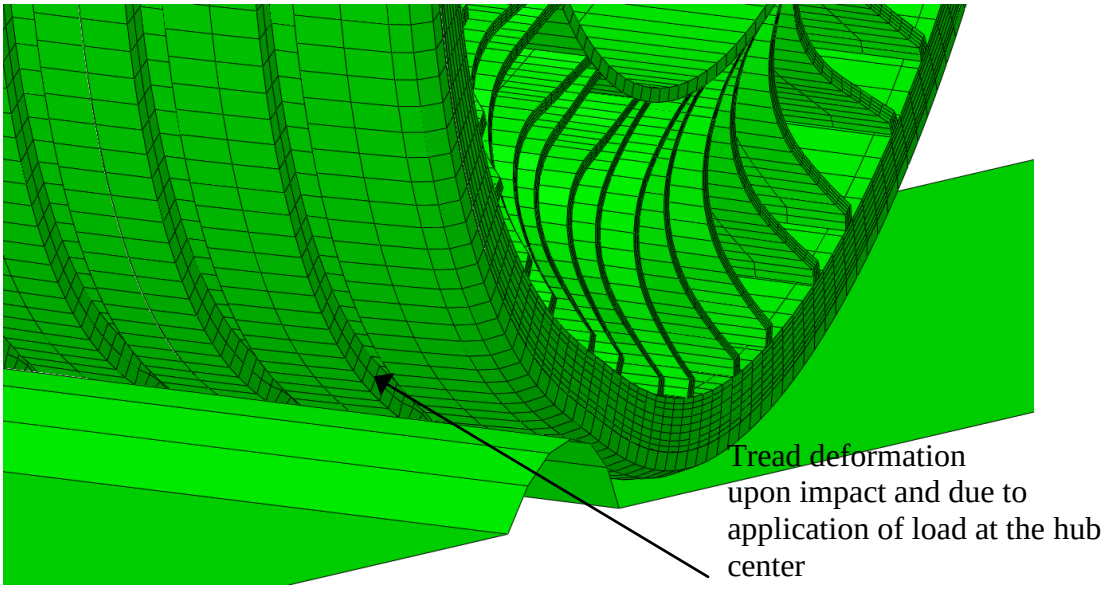

Figure 6.12: Deformation of the Tread upon impacting the obstacle

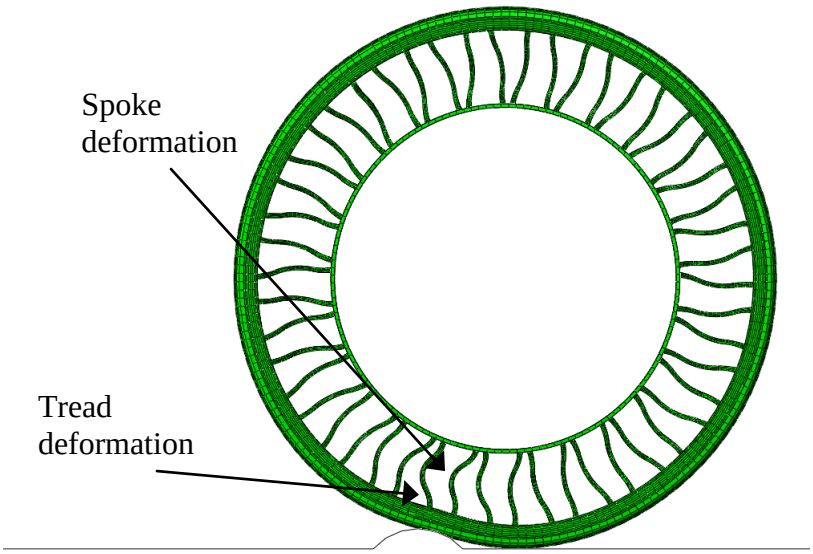

Figure 6.13: X-Y view of 3D Tweel impacting an obstacle

Spoke deformation

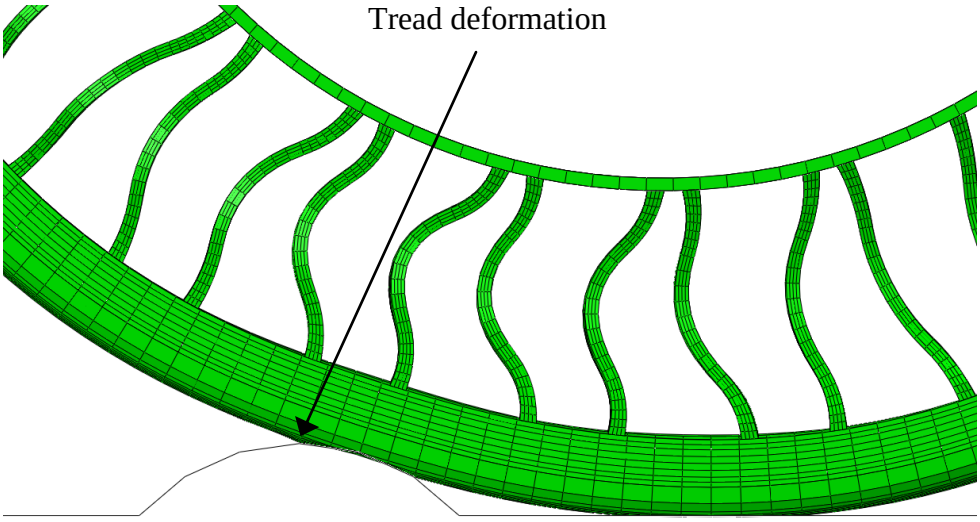

Figure 6.14: Deformation of the spokes and the tread upon first obstacle impact.

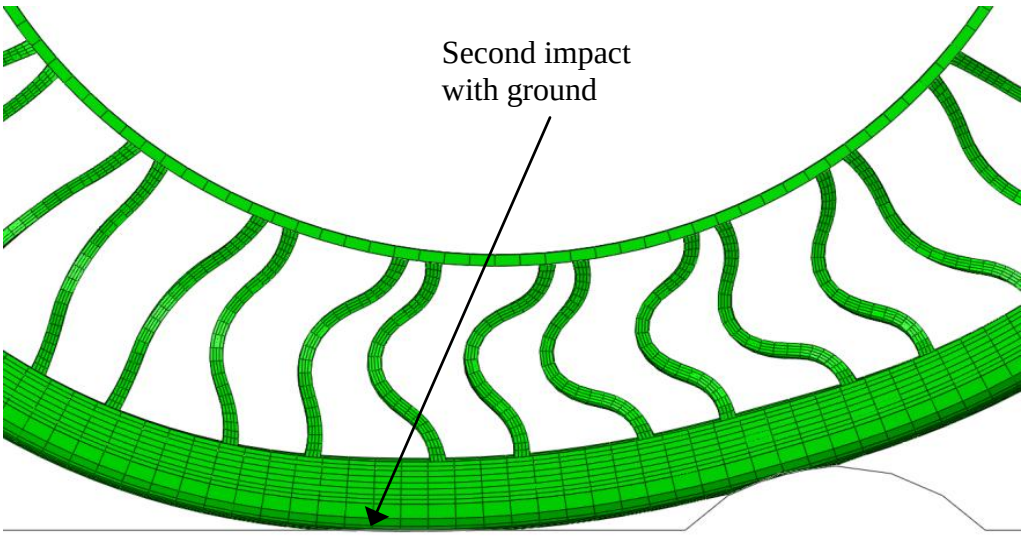

Figure 6.15: Deformation of the spokes and the tread upon impact with the ground after traversing the obstacle.

6.4.1 Reference Tweel Model

Upon dynamic explicit analysis of the Tweel with Marlow properties for the ring and spokes as described in Chapter Two, the axial hub velocity time-history for the reference model is shown in Figure 6.16.

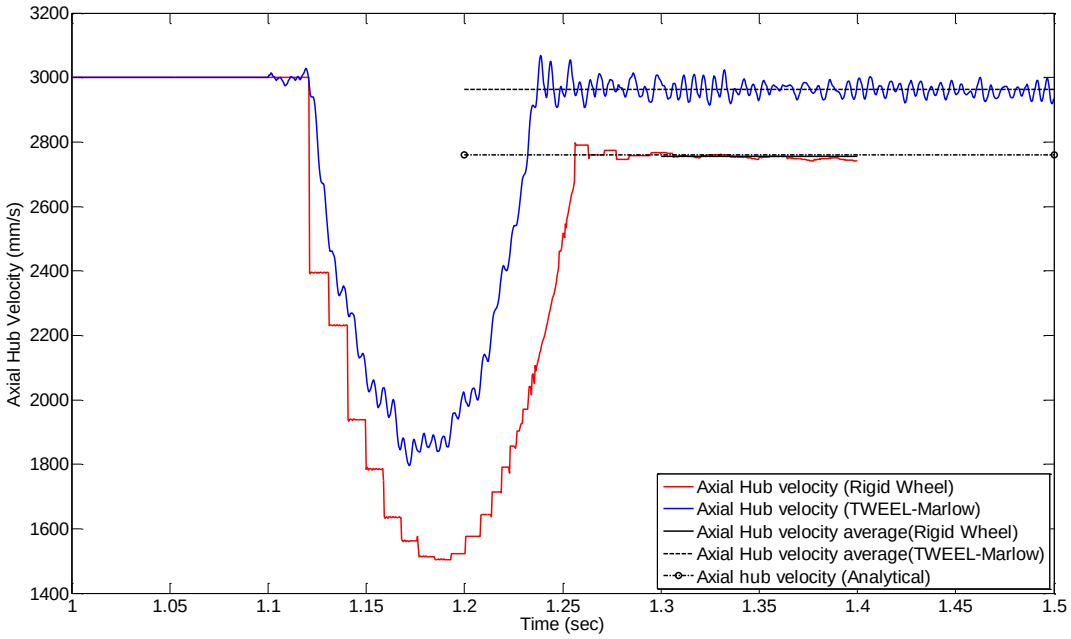

Figure 6.16: The axial hub velocity of the TWEEL in comparison with the rigid wheel.

From time 1 < t < 1.1, the Tweel is maintained at a constant velocity of 3000 mm/sec. From the next increment after t=1.1, as explained earlier, no kinematic constraints other than contact with the ground surface are enforced. After initial impact, the Tweel rolls up over the obstacle with height b = 22.5 mm, and the axial velocity drops to 1797 mm/s at t=1.172 sec. This drop is recorded at the maximum obstacle height. Once the Tweel rolls over from the obstacle, the velocity again increases to a peak value of 3068 mm/s at t=1.239. This is the point where the Tweel impacts the flat ground after traversing the obstacle. From 1.239 < t < 1.5, the vibration seen in the Figure is due to the hyperelastic response of the Tweel when it impacts the ground after traversing the obstacle. On taking the average of the velocity values between 1.3 < t < 1.5, the average velocity value is calculated to be 2962 mm/sec. This shows that the reduction in the axial

hub velocity is 1.265%. This is calculated by taking the initial hub velocity of 3000 mm/s and the final velocity to be the average value that was calculated, i.e.

$$\frac{\Delta V}{V_i} = \frac{V_i - V_f}{V_i} = \frac{3000 - 2962}{3000} = .01265$$

The Tweel hub velocity reduction of 1.265% is significantly lower than the approximately 8% velocity reduction found in the rigid wheel models. This result is consistent with the trend in values reported in [1]. As discussed earlier, a reduction in axial velocity corresponds to a reduction in linear momentum, which implies an increase in linear impulse, and harshness.

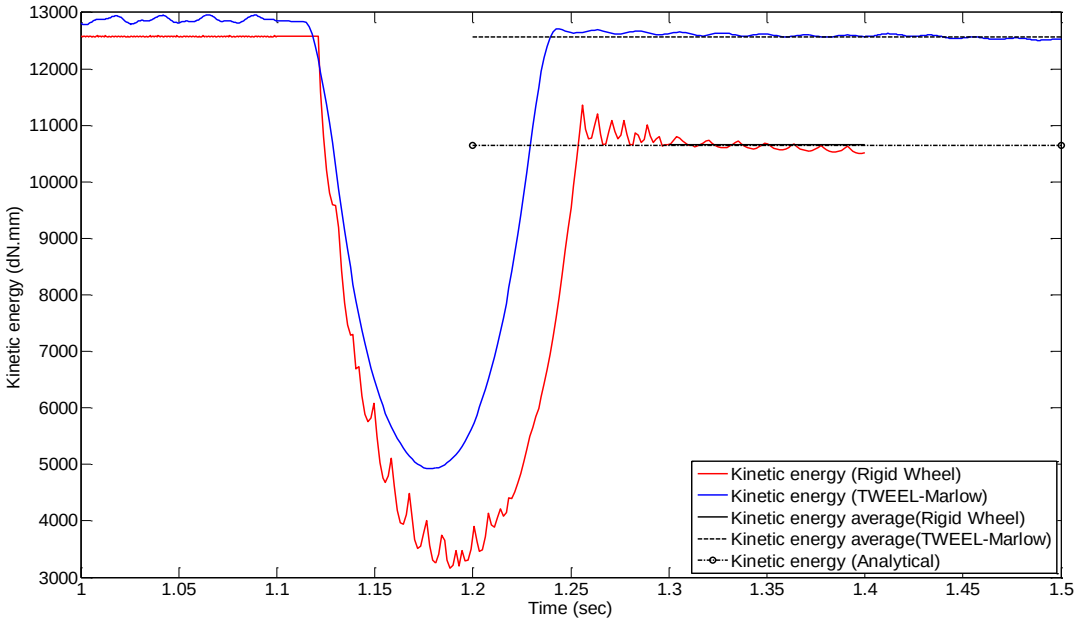

Figure 6.17: Kinetic energy of the TWEEL in comparison with the Rigid wheel.

Figure 6.17 shows the kinetic energy (KE) profile for the reference model. We observe that prior to impact, the average kinetic energy for the Tweel model is 12870.95 dN-mm, which is higher than the initial kinetic energy of 12593.7 dN-mm predicted by the rigid analytical model. The increase in the initial KE for the Tweel model can be

explained due to the local motion of the hyperelastic spokes and ring during rolling and also due to buckling and snapping back of spokes when entering and exiting the contact region, which is not accounted for in the analytical rigid model.

After impacting the obstacle, the average kinetic energy of the Tweel is 12569.1 dN-mm. The final kinetic energy in the Tweel model includes all sources of motion, including vertical motion due to the hyperelastic bouncing effect and internal vibrations after traversing the obstacle and impacting the rigid ground.

The velocity and the kinetic energy values for the analytical model of the rigid wheel, the finite element model of the rigid wheel modeled as a steel ring with rigid hub and the Tweel are summarized in Table 6-2.

Table 6-2: Summary of the velocity and K.E values of the analytical rigid wheel, finite element rigid wheel and the Tweel

	Initial velocity (mm/s)	Final velocity (mm/s)	Reduction in velocity	Initial K.E (dN-mm)	Final K.E (dN-mm)	Reduction in K.E
Analytical Rigid Wheel	3000	2758.8	8.04%	12593.7	10651	15.4%
Finite Element Rigid Wheel	3000	2754.32	8.2%	12570	10661	15.2%
Tweel	3000	2962	1.265%	12871	12569	2.34%

For reference, the vertical component of velocity and angular speed of the Tweel hub during the impact event from 1 sec to 1.5 sec is shown in Figure 6.18 and Figure 6.19.

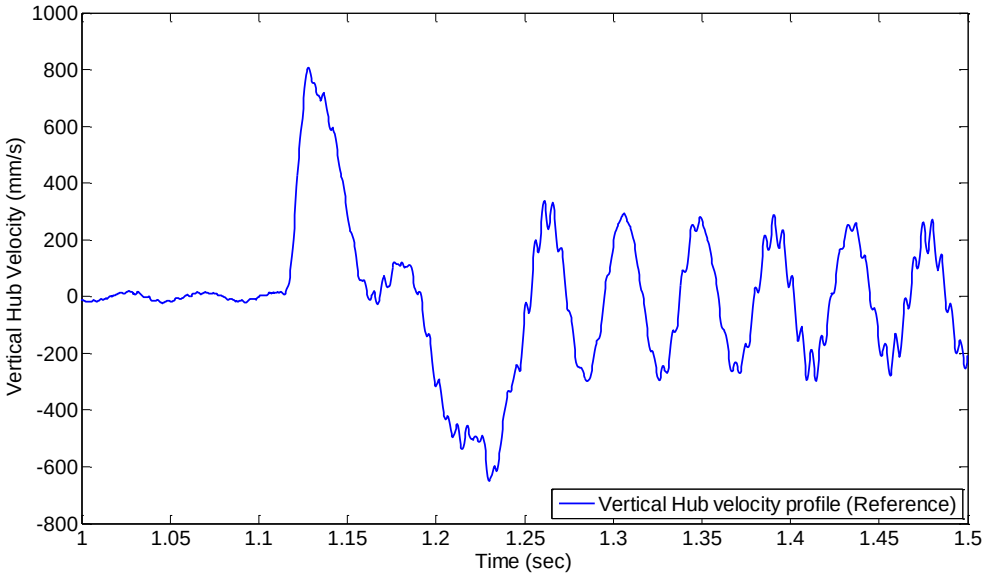

Figure 6.18: Vertical hub velocity profile of the Reference Marlow model

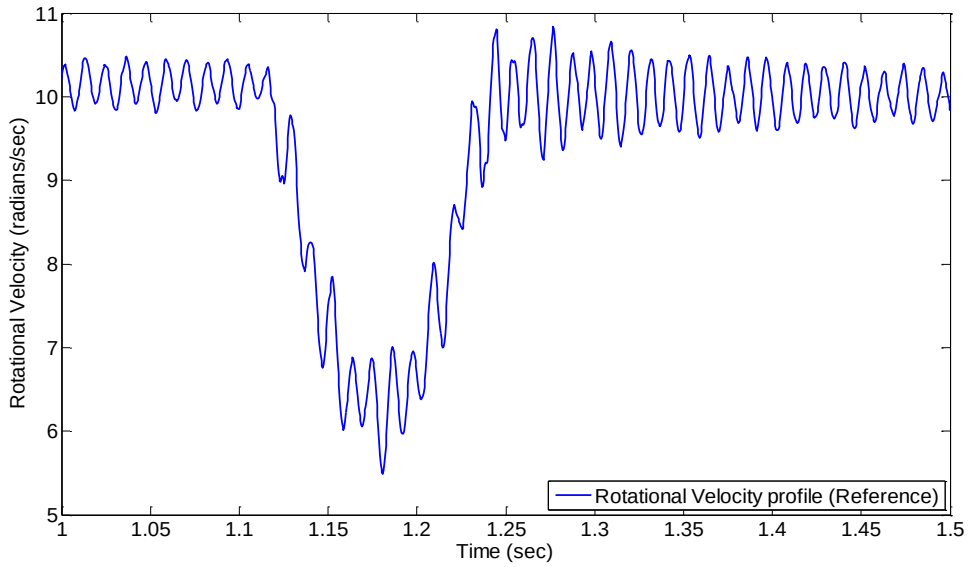

Figure 6.19: Rotational velocity profile of the Reference Marlow model.

Comparing the average initial kinetic energy to the average final kinetic energy, the energy loss is 2.3457%. From the results in Figure 6.16 and Figure 6.17, it can be concluded that the Tweel loses significantly less energy than the analytical rigid wheel

and steel ring with rigid hub finite element rigid wheel when traversing the obstacle. The reduction in velocities and the proportion of energy lost for different material models are compared in the following sections of this chapter.

6.4.2 Shear modulus of the Mooney Rivlin model for the ring remains unchanged

From Figure 6.20, the reduction in velocity for the Tweel model with a Mooney Rivlin unchanged model for the ring is 1.22% corresponding to an average final velocity of 2963.26 mm/s. Recall that the Tweel model with Marlow properties for the ring recorded a reduction in average velocity of 1.265% (2962 mm/s).

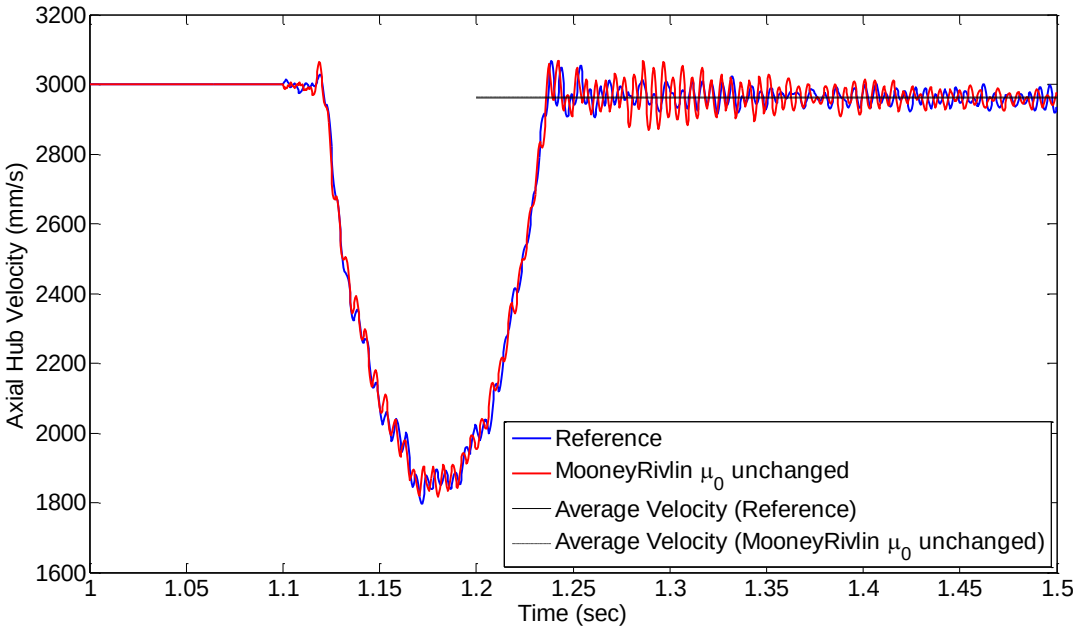

Figure 6.20: Axial hub velocity profiles of the Tweel with Marlow properties (1.265%) and an unchanged Mooney Rivlin material model for the ring (1.22%)

In Figure 6.21 the average initial kinetic energy for the unchanged Mooney Rivlin model for the ring is 12890.59064 daN - mm. The average kinetic energy for the same

model after traversing the obstacle is 12589.2653 daN – mm. The percentage proportion of energy loss is estimated as 2.3375%. The percentage proportion of energy loss for the reference model is 2.3457%. These results show that the original Mooney-Rivlin model which was least-squares fit to the reference Marlow stress-strain properties does not change significantly the final speed of the Tweel after traversing the obstacle, and thus the energy loss is predicted to be about the same amount.

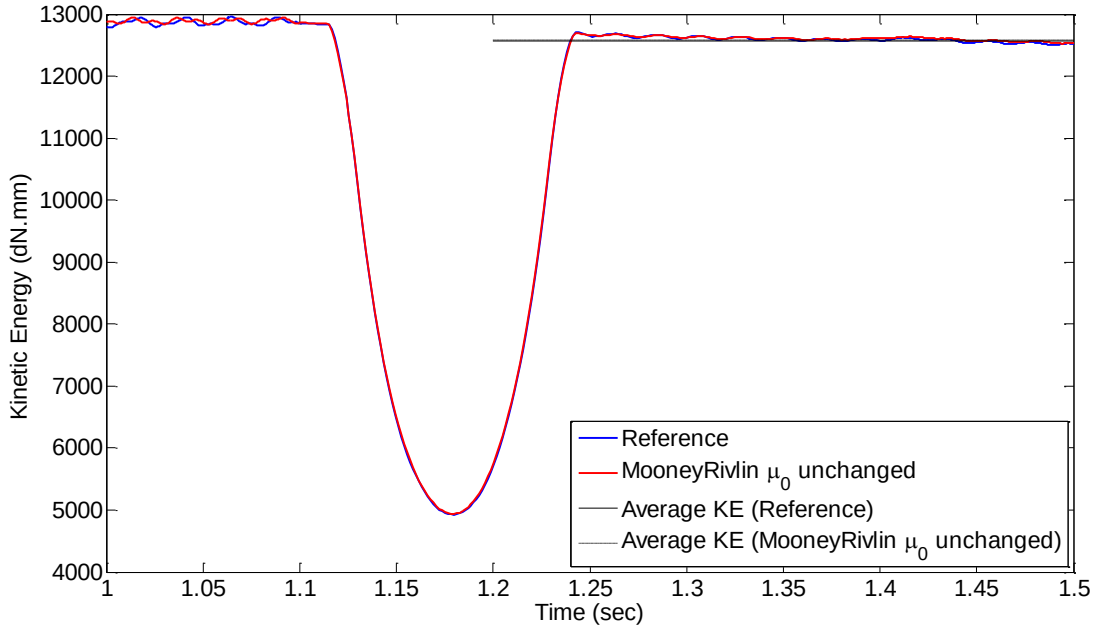

Figure 6.21: Kinetic Energy profiles for the Tweel with Marlow properties (2.345%) and an unchanged Mooney Rivlin material model for the ring (2.337%)

6.4.3 Shear modulus of the Mooney Rivlin material model for the ring is reduced by 25%

In Figure 6.22, the reduction in velocity for the Tweel model with a Mooney Rivlin reduced model for the ring is 1.093% (2967.209174 mm/s). The Tweel model with a Mooney Rivlin unchanged model for the ring recorded a reduction in velocity of 1.22%

(2963.25843 mm/s). In Figure 6.23, the initial kinetic energy of the reduced model is 12917.13448 daN – mm. The kinetic energy of the reduced model after traversing the obstacle is 12644.89813 daN – mm. The percentage proportion of energy loss for the reduced model is 2.1075%. Recall that the unchanged Mooney Rivlin model for the ring had a percentage proportion of energy loss of 2.3375%. When the shear modulus is reduced, the model loses less energy than the unchanged model.

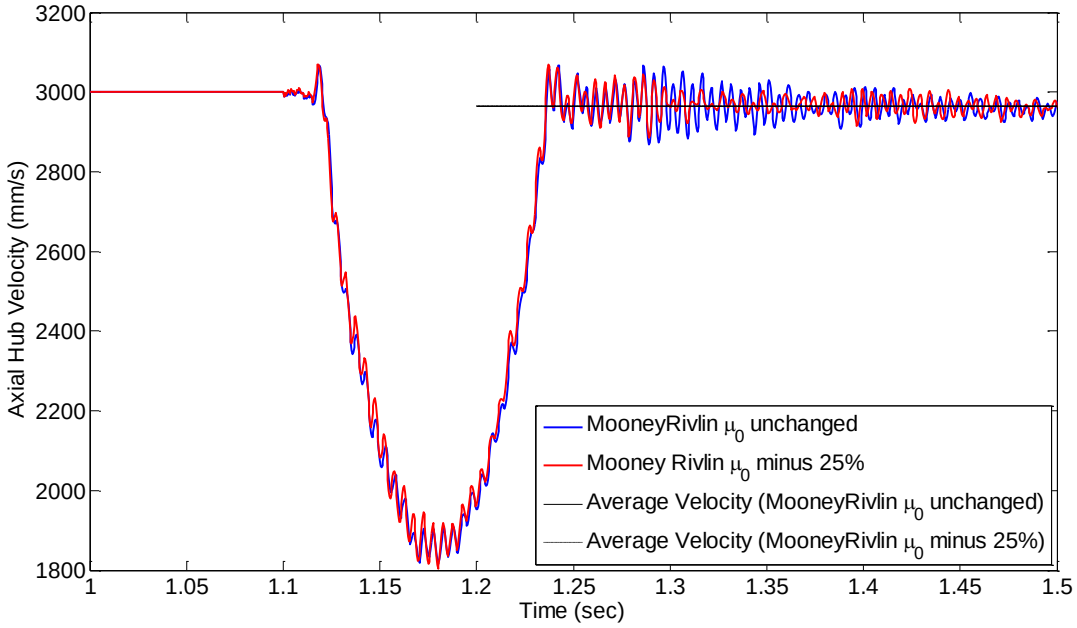

Figure 6.22: Axial hub velocity profiles of the Tweel with a reduced Mooney Rivlin model for the ring (1.093%) and an unchanged Mooney Rivlin material model for the ring (1.22%)

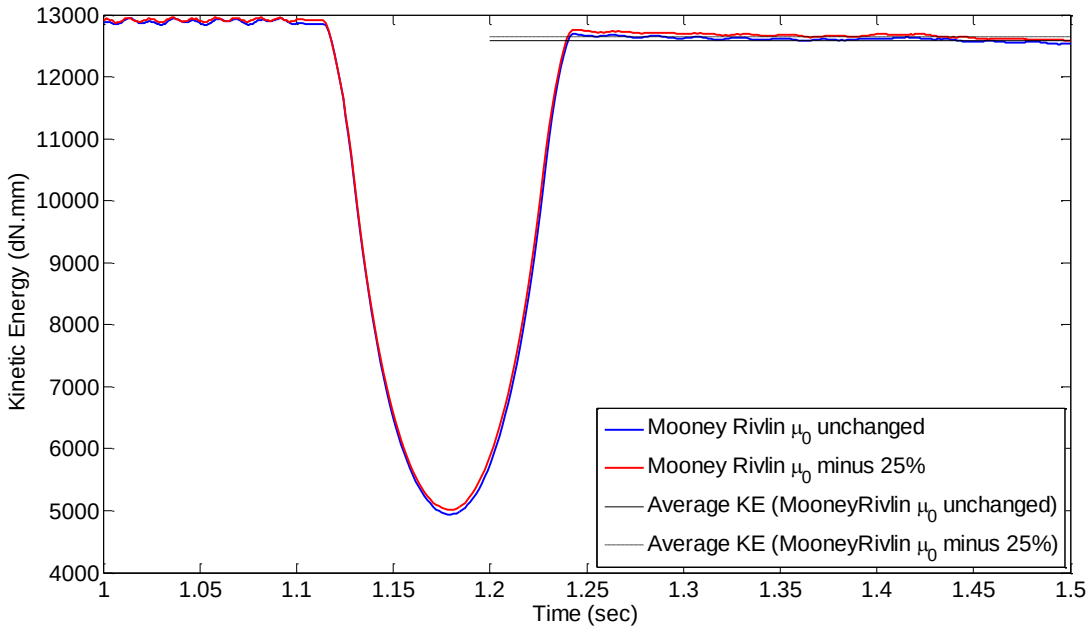

Figure 6.23: Kinetic Energy profiles for the Tweel with a reduced Mooney Rivlin material model (2.1075%) and an unchanged Mooney Rivlin material model for the ring (2.3375%)

6.4.4 Shear modulus of the Mooney Rivlin model for the ring is increased by 25%

In Figure 6.24, the reduction in velocity for the Tweel model with a Mooney Rivlin increased model for the ring is 1.368% (2958.930537 mm/s). The Tweel model with a Mooney Rivlin unchanged model for the ring recorded a reduction in velocity of 1.22% (2963.25843 mm/s). In Figure 6.25, the initial kinetic energy of the Mooney Rivlin model with an increased shear modulus is 12870.36355 daN – mm. The final kinetic energy after traversing the obstacle is 12551.00858 daN – mm. The percentage proportion of energy lost for the Mooney Rivlin model with increased shear modulus is 2.4813%. Recall that the percentage proportion of energy lost for a Mooney Rivlin model

with an unchanged shear modulus is 2.3375%. When the shear modulus is increased, the proportion of energy lost is more than the unchanged model.

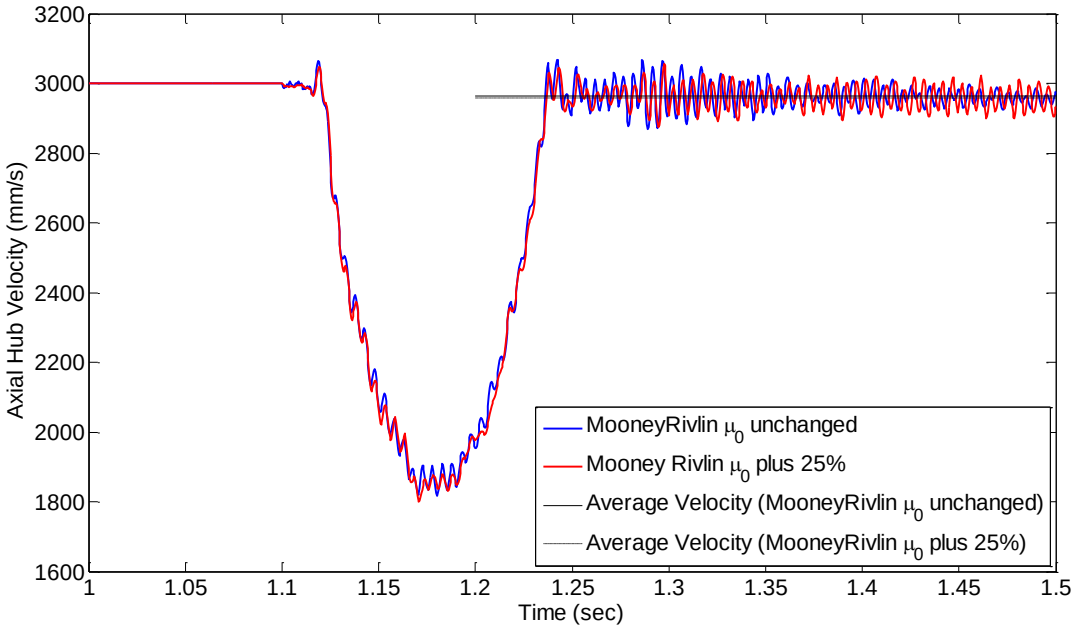

Figure 6.24: Axial hub velocity profiles of the Tweel with an increased Mooney Rivlin model for the ring (1.368%) and an unchanged Mooney Rivlin material model for the ring (1.22%)

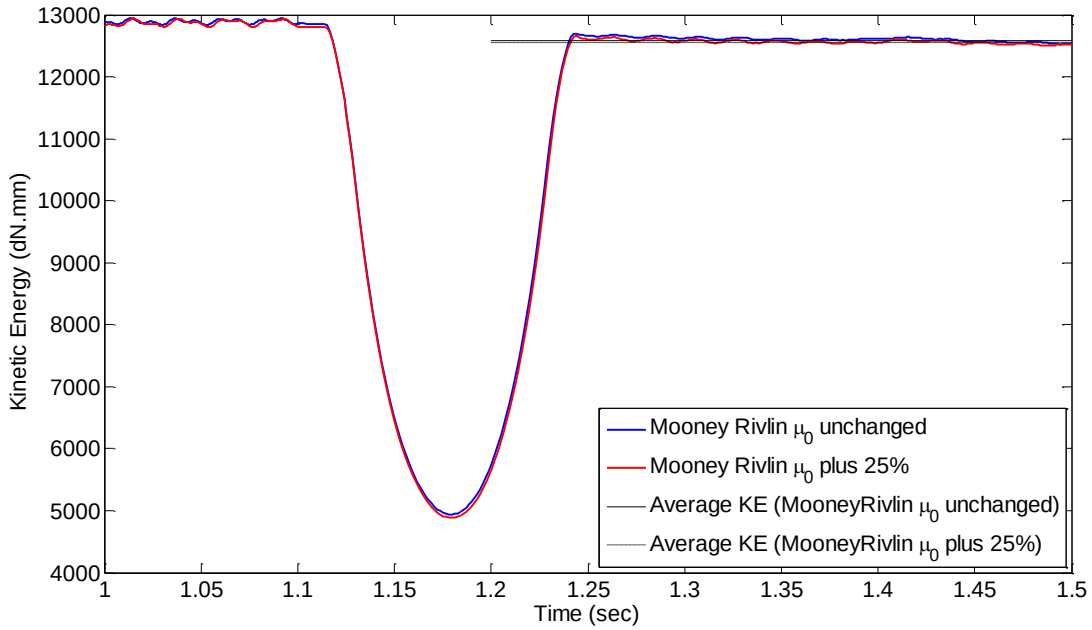

Figure 6.25: Kinetic Energy profiles for the Tweel with a reduced Mooney Rivlin material model (2.4813%) and an unchanged Mooney Rivlin material model for the ring (2.3375%)

6.4.5 Shear modulus of the Neo Hookean material model for the ring remains unchanged

From Figure 6.26, the reduction in velocity for the Tweel model with a Neo Hookean unchanged model for the ring is 1.314% (2960.560868 mm/s). The Tweel model with Marlow properties for the ring recorded a reduction in velocity of 1.265% (2962.052025 mm/s). In Figure 6.27, the initial kinetic energy of the unchanged Neo Hookean model for the ring is 12941.90394 daN – mm. The final kinetic energy after traversing the obstacle is 12612.87425 daN – mm. The percentage proportion of energy loss is calculated to be 2.5423%. Recall that the percentage proportion of energy lost for the reference Marlow model is 2.3457%. From these results show that the Tweel with an unchanged Neo Hookean model for the ring loses more energy upon impact than the Marlow model.

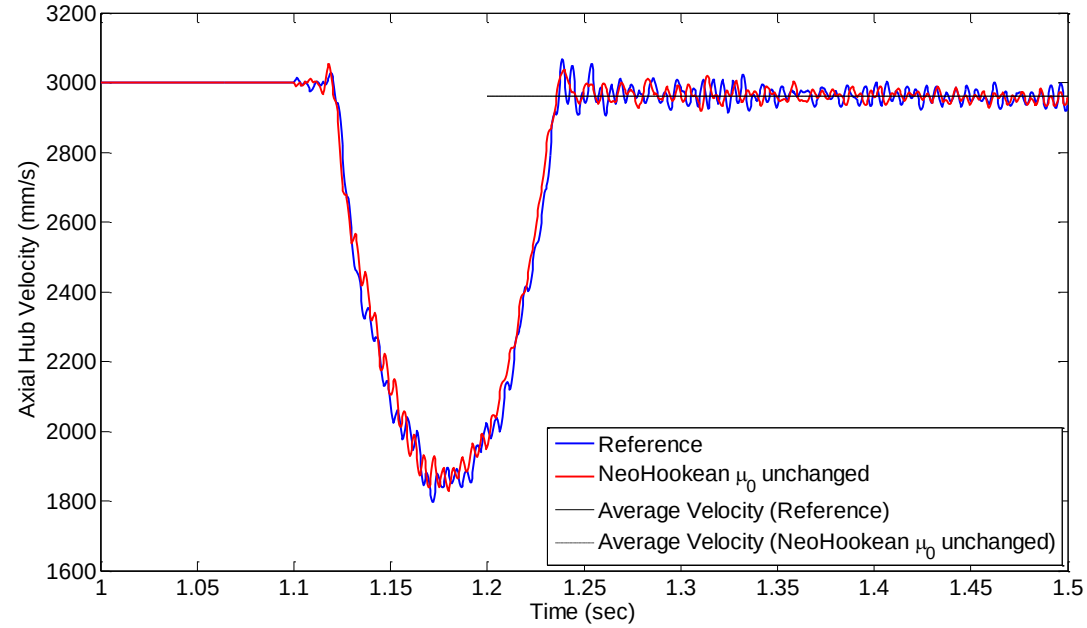

Figure 6.26: Axial hub velocity profiles of the Tweel with an unchanged Neo Hookean model for the ring (1.314%) and the reference model (1.265%)

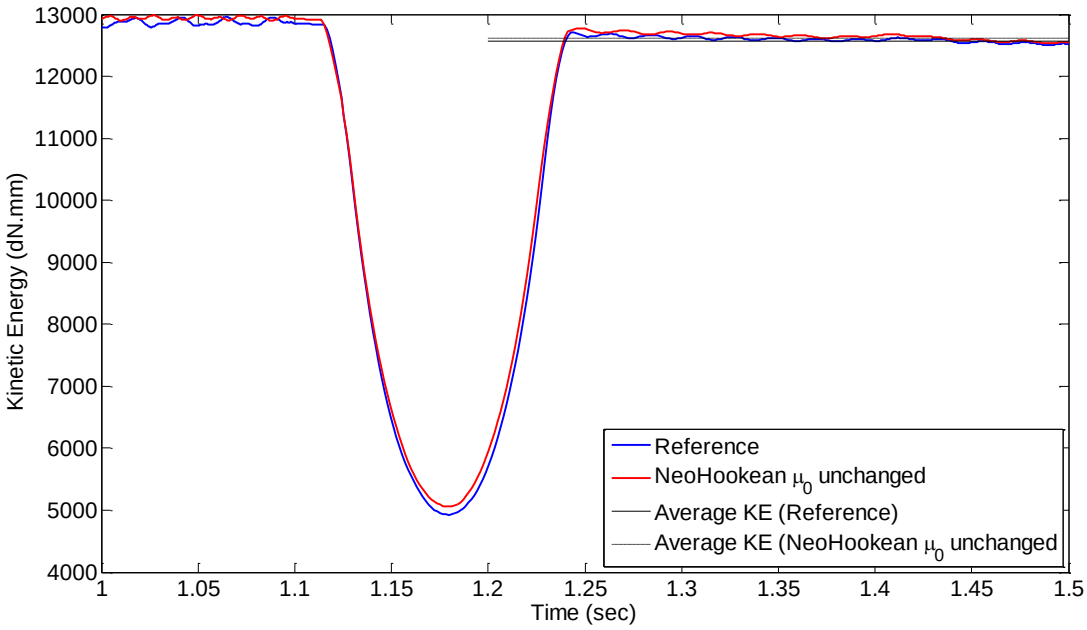

Figure 6.27: Kinetic Energy profiles for the Tweel with an unchanged Neo Hookean material model (2.5423%) and the reference model (2.3457%)

6.4.6 Shear modulus of the Neo Hookean material model for the ring is reduced by 25%

In Figure 6.28, the reduction in velocity for the Tweel model with a Neo Hookean unchanged model for the ring is 1.314% (2960.560868 mm/s). The Tweel model with a Neo Hookean reduced model recorded a reduction in velocity of 1.87% (2943.875393 mm/s). In Figure 6.29, the initial kinetic energy of the Neo Hookean model with a reduced shear modulus is 12962.68621 daN – mm. The final kinetic energy of the model after traversing the obstacle is 12531.30485 daN – mm. The percentage proportion of energy lost upon impact is 3.3278%. Recall that the percentage proportion of energy lost upon impact for the unchanged Neo Hookean model is 2.5423%. Hence, from these results, it can be said that the Neo Hookean reduced model for the ring loses more energy than the Neo Hookean unchanged model.

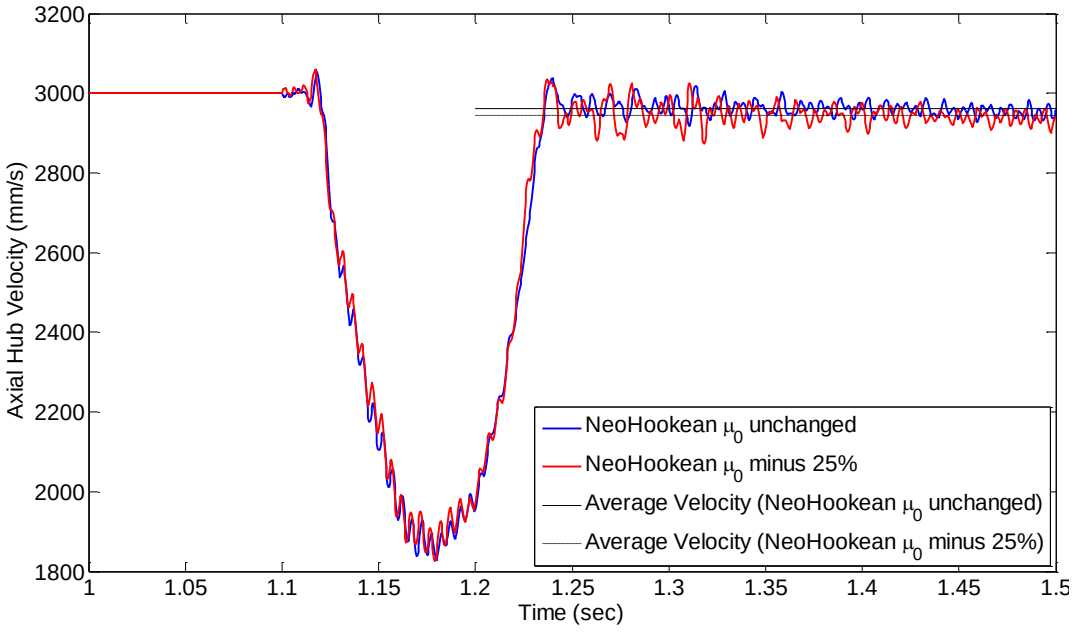

Figure 6.28: Axial hub velocity profiles of the Tweel with an unchanged Neo Hookean model for the ring (1.314%) and a reduced Neo Hookean model (1.87%)

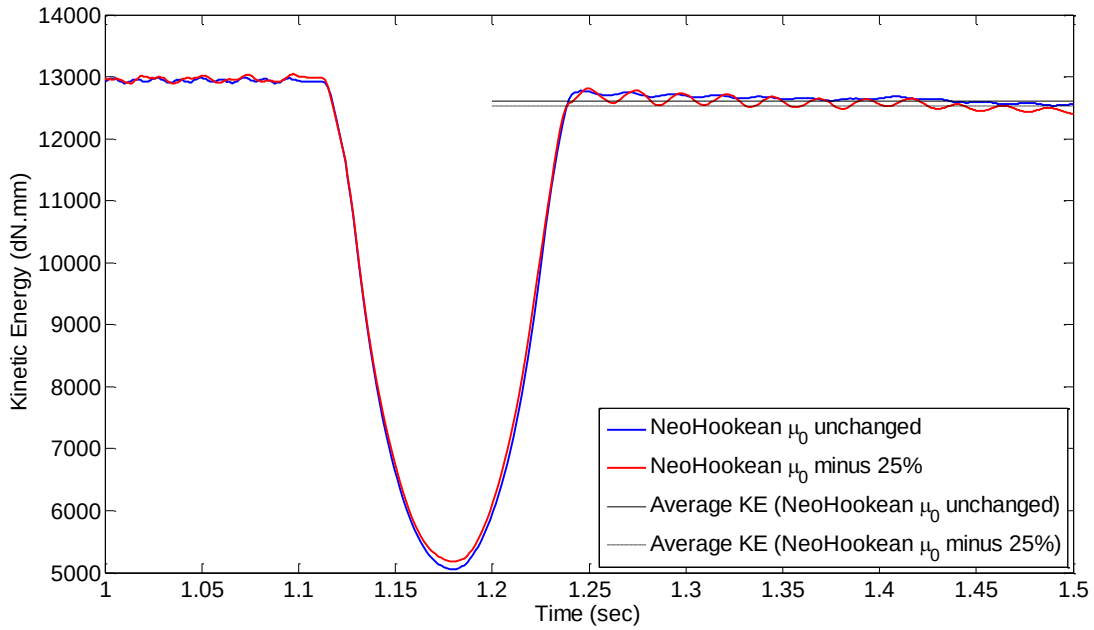

Figure 6.29: Kinetic Energy profiles for the Tweel with an unchanged Neo Hookean material model (2.5423%) and a reduced Neo Hookean model (3.3278%)

6.4.7 Shear modulus of the Neo Hookean model for the ring is increased by 25%

In Figure 6.30, the reduction in velocity for the Tweel model with a Neo Hookean unchanged model for the ring is 1.314% (2960.560868 mm/s). The Tweel model with a Neo Hookean increased model recorded a reduction in velocity of 1.139% (2965.820165 mm/s). From Figure 6.31, the initial kinetic energy of the Neo Hookean with increased shear modulus is 12923.47783 daN – mm. The final kinetic energy of the model after traversing the obstacle is 12633.3694 daN – mm. The percentage proportion of energy lost is 2.2448%. On comparing with the unchanged Neo Hookean model, the increased model loses less energy.

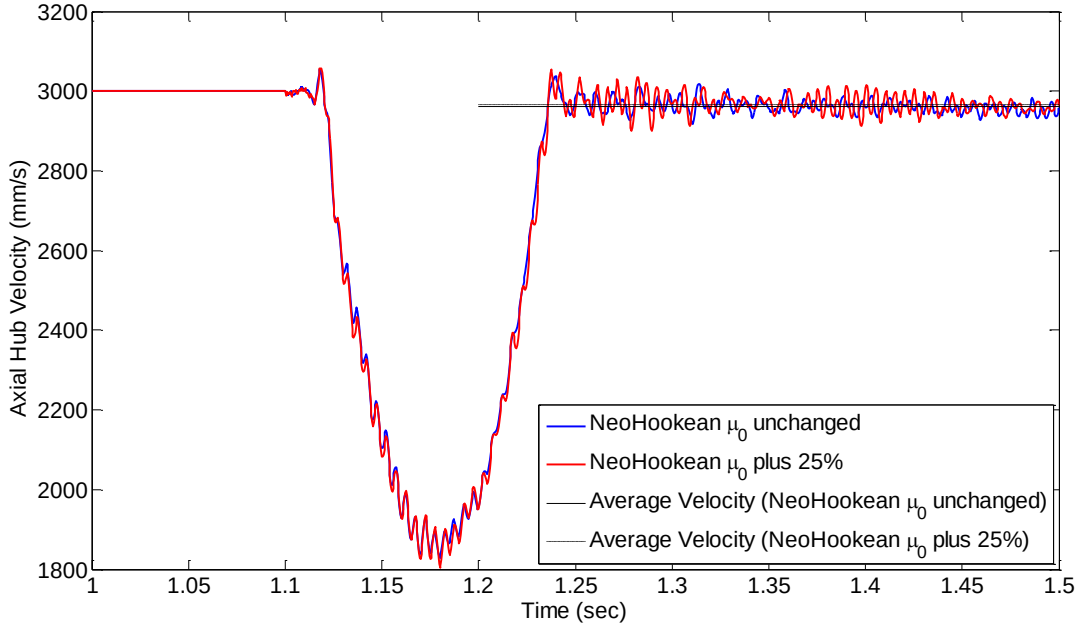

Figure 6.30: Axial hub velocity profiles of the Tweel with an unchanged Neo Hookean model for the ring (1.314%) and an increased Neo Hookean model (1.139%)

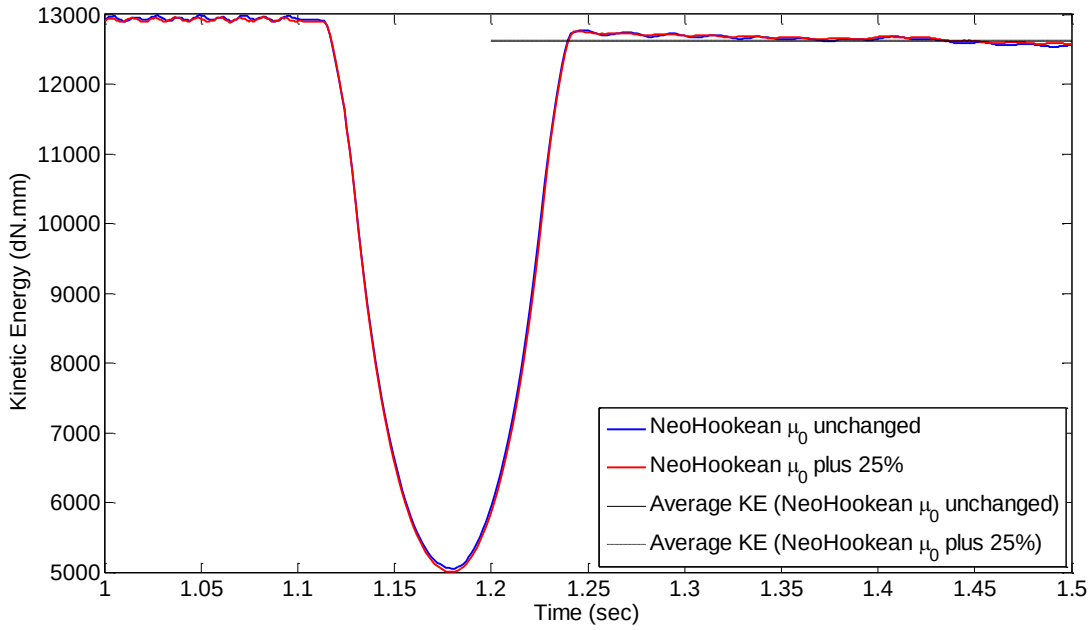

Figure 6.31: Kinetic Energy profiles for the Tweel with an unchanged Neo Hookean material model (2.5423%) and an increased Neo Hookean model (2.2448%)

6.4.8 Shear modulus of the Mooney Rivlin model for the spokes remains unchanged

In Figure 6.32, the reduction in velocity for the Tweel model with a Mooney Rivlin unchanged model for the spoke is 1.32% (2960.30396 mm/s). The Tweel model with Marlow properties recorded a reduction in velocity of 1.265% (2962.052025 mm/s).

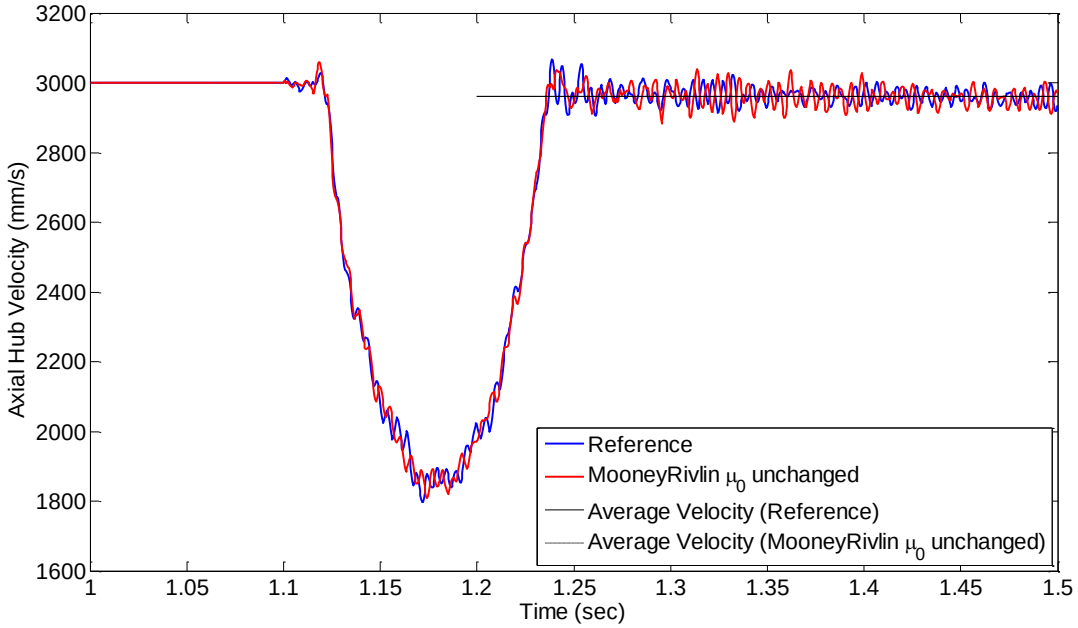

Figure 6.32: Axial hub velocity profile of the Tweel with Mooney Rivlin unchanged model on the spokes (1.32%) and with Marlow properties (1.265%)

From Figure 6.33, the initial kinetic energy for the unchanged Mooney Rivlin model for the spokes is 12899.21232 daN – mm. The final kinetic energy after traversing the obstacle is 12573.40336 daN – mm. The percentage proportion of energy loss is 2.5258%. On comparing with the reference Marlow model, the Mooney Rivlin unchanged model for the spokes loses more energy.

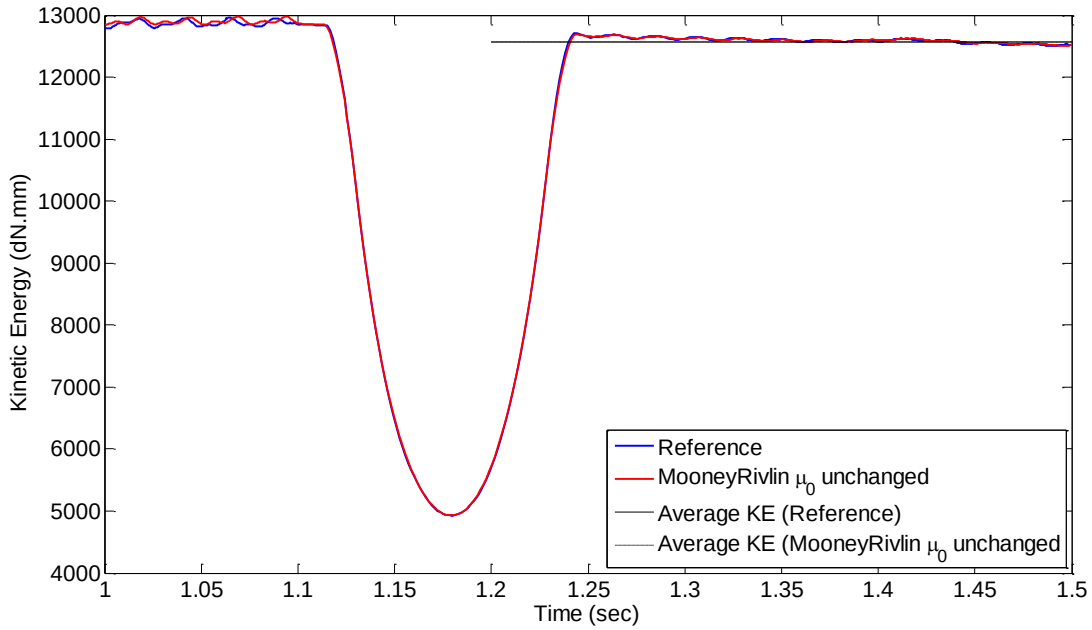

Figure 6.33: Kinetic energy profiles for the Tweel with Mooney Rivlin for the spokes (2.5258%) and with Marlow properties (2.3457%)

6.4.9 Shear modulus of the Mooney Rivlin material for the spokes is reduced by 25%

In Figure 6.34, the reduction in velocity for the Tweel model with a Mooney Rivlin unchanged model for the spoke is 1.32% (2960.30396 mm/s). The Tweel model with a Mooney Rivlin reduced model for the spokes recorded a reduction in velocity of 1.034% (2968.964607 mm/s). In Figure 6.35, the initial kinetic energy of the Mooney Rivlin model with reduced shear modulus is 12940.29507 daN – mm. The final kinetic energy after traversing the obstacle is 12686.73396 daN – mm. The percentage proportion of energy lost is 1.9594%. On comparing with the unchanged Mooney Rivlin model, the reduced Mooney Rivlin model for the spokes loses less energy.

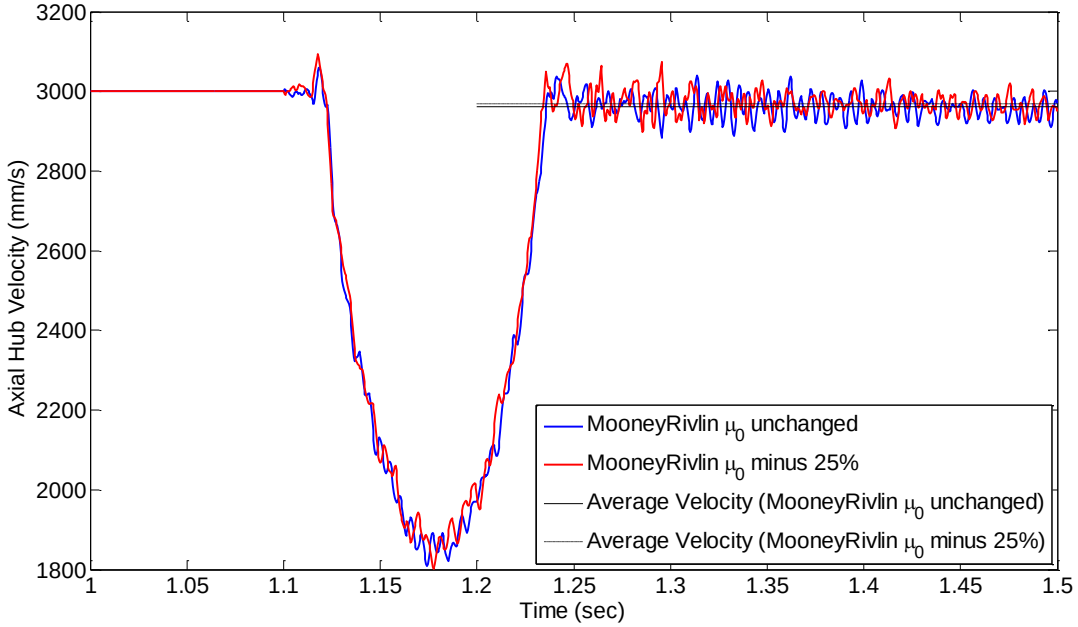

Figure 6.34: Axial hub velocity profile for the Tweel with a Mooney Rivlin unchanged model (1.32%) and a Mooney Rivlin reduced model (1.034%)

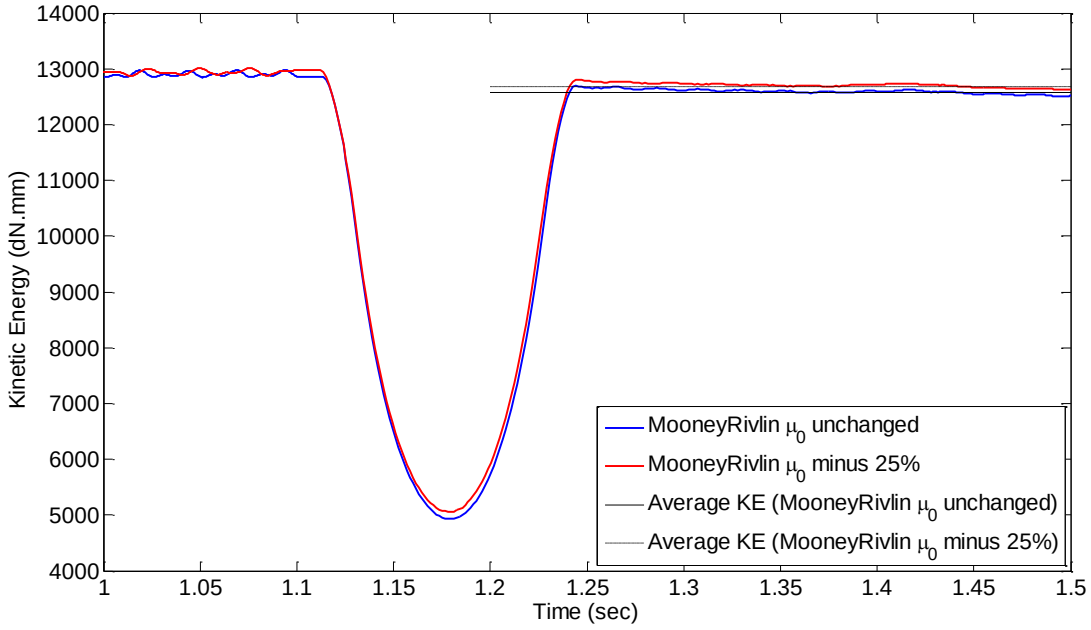

Figure 6.35: Kinetic energy profile for the Tweel with a Mooney Rivlin unchanged model (2.5258%) and a Mooney Rivlin reduced model (1.9594%)

6.4.10 Shear modulus of the Mooney Rivlin material for the spokes is increased by 25%

In Figure 6.36, the reduction in velocity for the Tweel model with a Mooney Rivlin unchanged model for the spoke is 1.32% (2960.30396 mm/s). The Tweel model with a Mooney Rivlin increased model for the spokes recorded a reduction in velocity of 1.338% (2959.856281 mm/s).

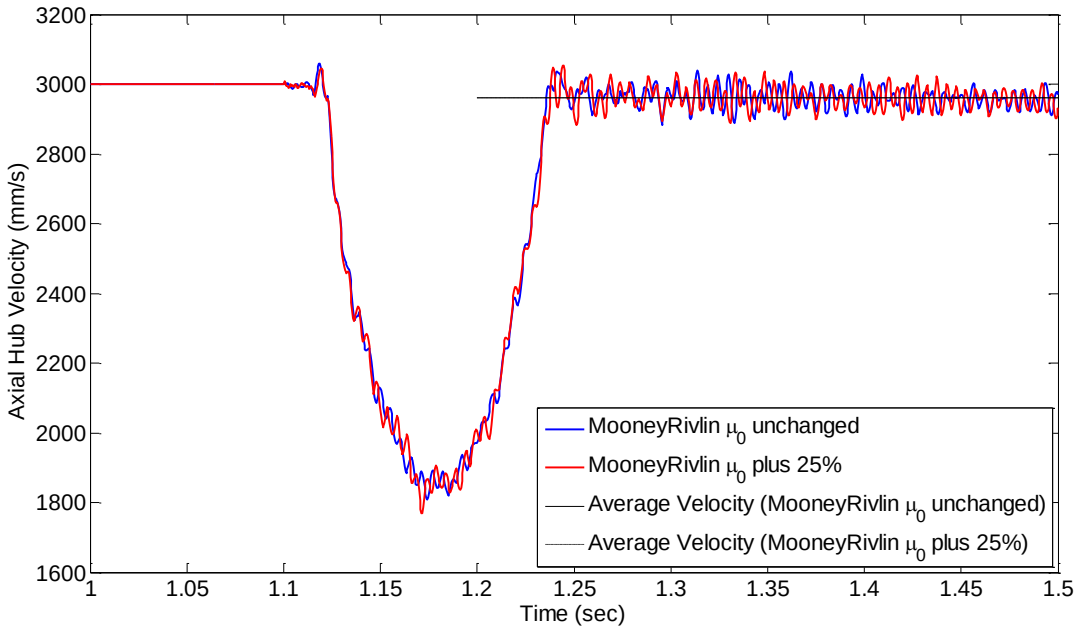

Figure 6.36: Axial hub velocity profiles for the Tweel with a Mooney Rivlin unchanged model (1.32%) and a Mooney Rivlin increased model (1.338%)

In Figure 6.37, the initial kinetic energy of the Mooney Rivlin model with increased shear modulus is 12867.65616 dN – mm. The final kinetic energy of the model is 12548.58134 dN – mm. The percentage proportion of energy lost is 2.4796%. On comparing with the unchanged Mooney Rivlin model, the Mooney Rivlin model with increased shear modulus loses less energy.

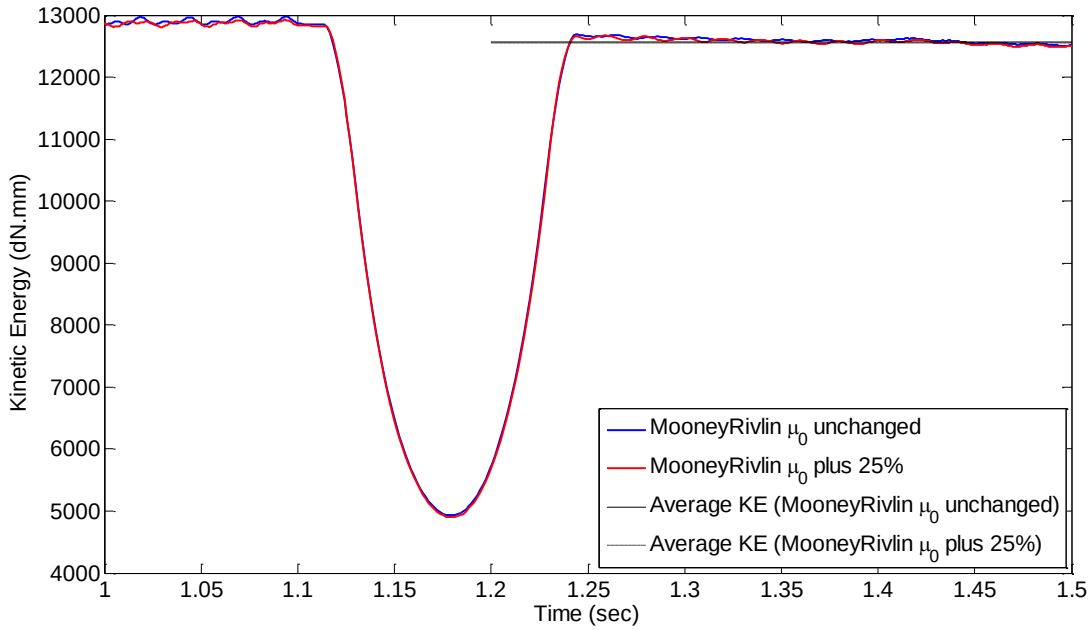

Figure 6.37: Kinetic energy profiles for the Tweel with a Mooney Rivlin unchanged model (2.5258%) and a Mooney Rivlin increased model (2.4796%) for the spokes

6.4.11 Shear modulus of the Neo Hookean material for the spokes remains unchanged

In Figure 6.38, the reduction in velocity for the Tweel model with a Neo Hookean unchanged model for the spoke is 1.28% (2961.582087 mm/s). The Tweel model with Marlow properties recorded a reduction in velocity of 1.265% (2959.856281 mm/s). In Figure 6.39, the initial kinetic energy of the unchanged Neo Hookean model is 12983.75172 daN – mm. The final kinetic energy after traversing the obstacle is 12678.47836 daN – mm. The percentage proportion of energy loss is 2.3511%. On comparing with the reference Marlow model, the unchanged Neo Hookean model loses slightly more energy.

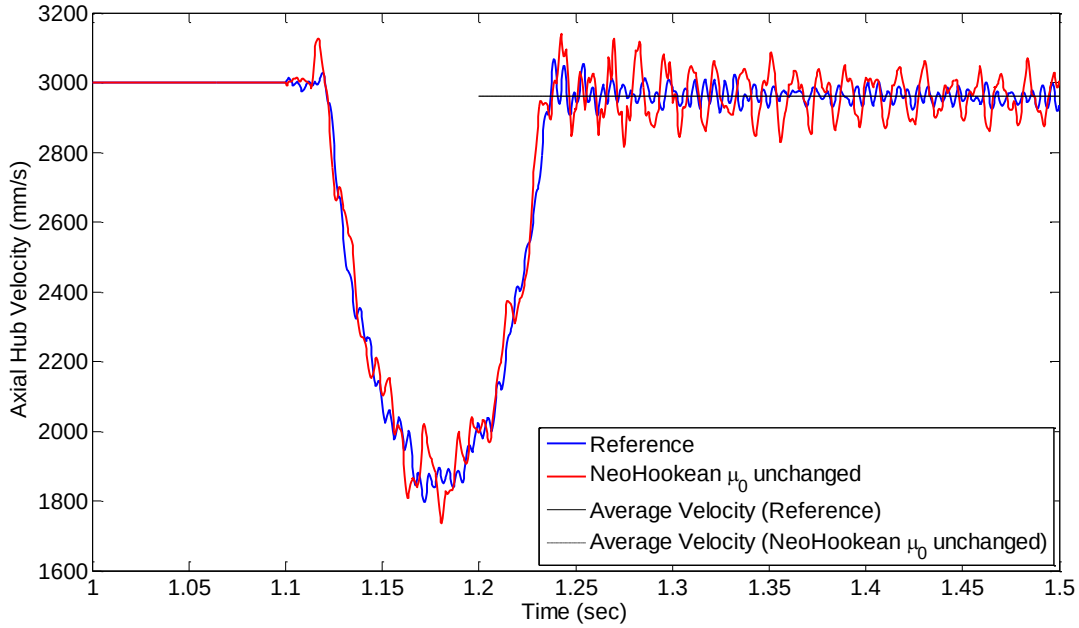

Figure 6.38: Axial hub velocity profile for the Tweel model with a Neo Hookean unchanged model (1.28%) and with Marlow properties (1.265%)

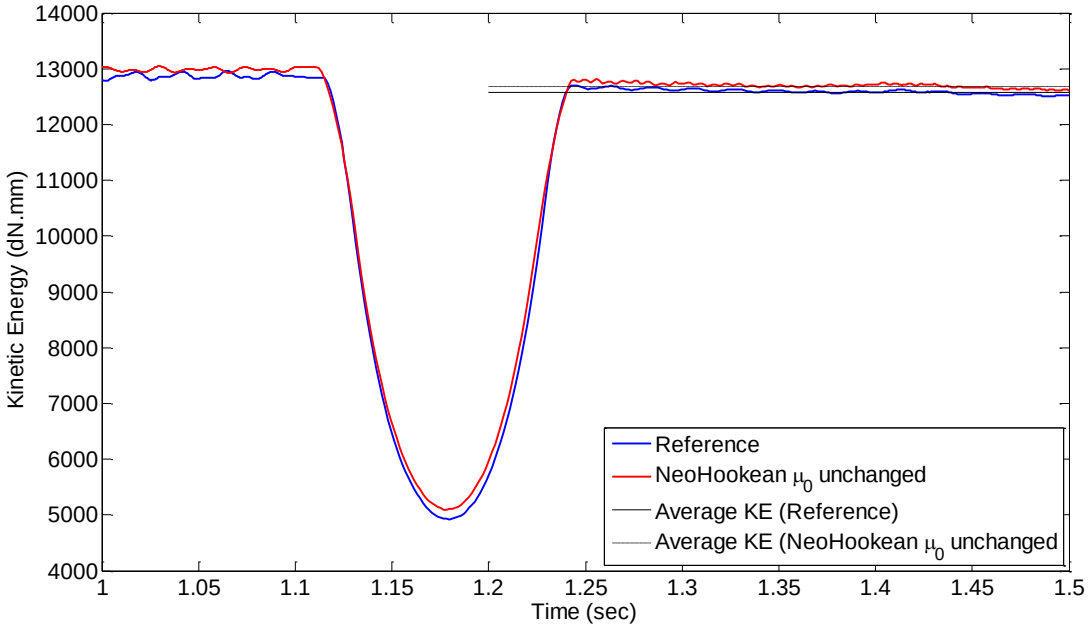

Figure 6.39: Kinetic energy profile for the Tweel with a Neo Hookean unchanged model (2.3511%) and Marlow properties (2.3457%)

6.4.12 Shear modulus of the Neo Hookean material for the spokes is reduced by 25%

In Figure 6.40, the reduction in velocity for the Tweel model with a Neo Hookean unchanged model for the spoke is 1.28% (2961.582087 mm/s). The Tweel model with a Neo Hookean reduced model recorded a reduction in velocity of 2% (2939.807149 mm/s).

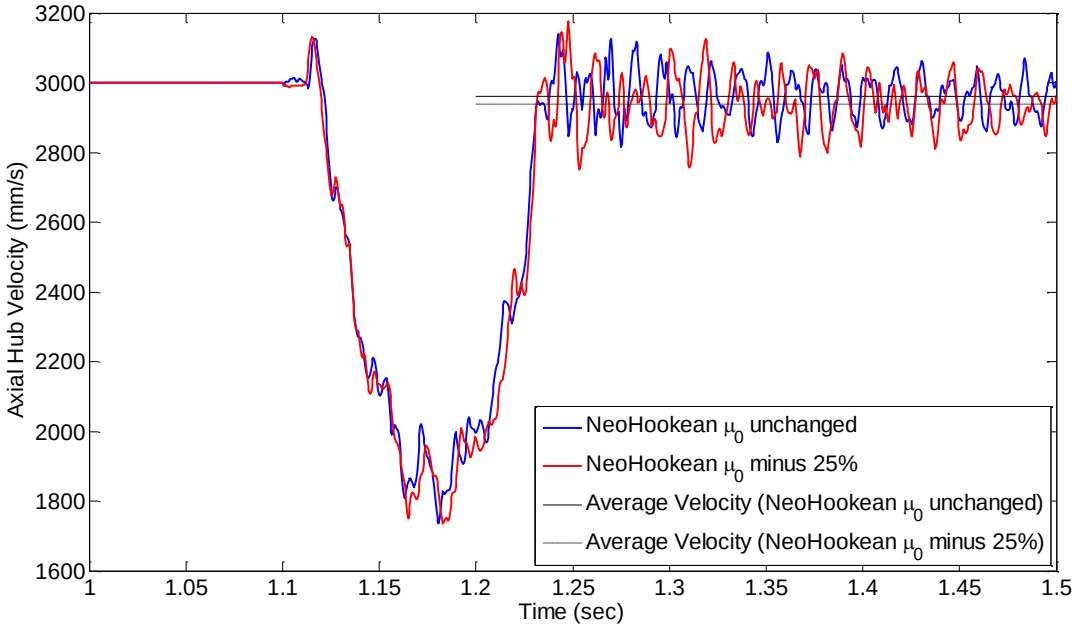

Figure 6.40: Axial hub velocity profile for the Tweel model with a Neo Hookean unchanged model (1.28%) and a Neo Hookean reduced model (2 %)

In Figure 6.41, the initial kinetic energy of the Neo Hookean model with a reduced shear modulus is 13021.66256 daN – mm. The final kinetic energy of the model after traversing the obstacle is 12546.92948 daN – mm. The percentage proportion of energy lost is 3.6457%. On comparing with the unchanged Neo Hookean model, the Neo Hookean model with reduced shear modulus loses a lot of energy.

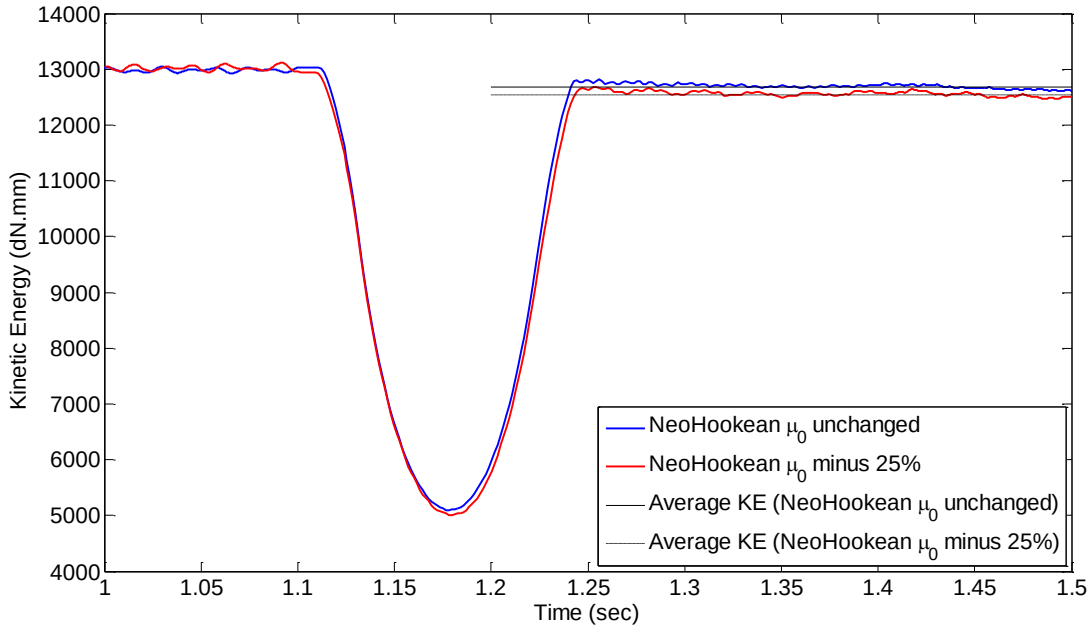

Figure 6.41: Kinetic energy profile for the Tweel with a Neo Hookean unchanged model (2.3511%) and Neo Hookean reduced model (3.6457%)

6.4.13 Shear modulus of the Neo Hookean material for the spokes is increased by 25%

In Figure 6.42, the reduction in velocity for the Tweel model with a Neo Hookean unchanged model for the spoke is 1.28% (2961.582087 mm/s). The Tweel model with a Neo Hookean increased model recorded a reduction in velocity of 0.958% (2971.256322 mm/s). In Figure 6.43, the initial kinetic energy of the Neo Hookean model with increased shear modulus is 12952.33596 daN – mm. The final kinetic energy of the model after traversing the obstacle is 12718.47425 daN – mm. The percentage proportion of energy lost is 1.8055%. On comparing with the Neo Hookean unchanged model, the Neo Hookean model with reduced shear modulus loses less energy.

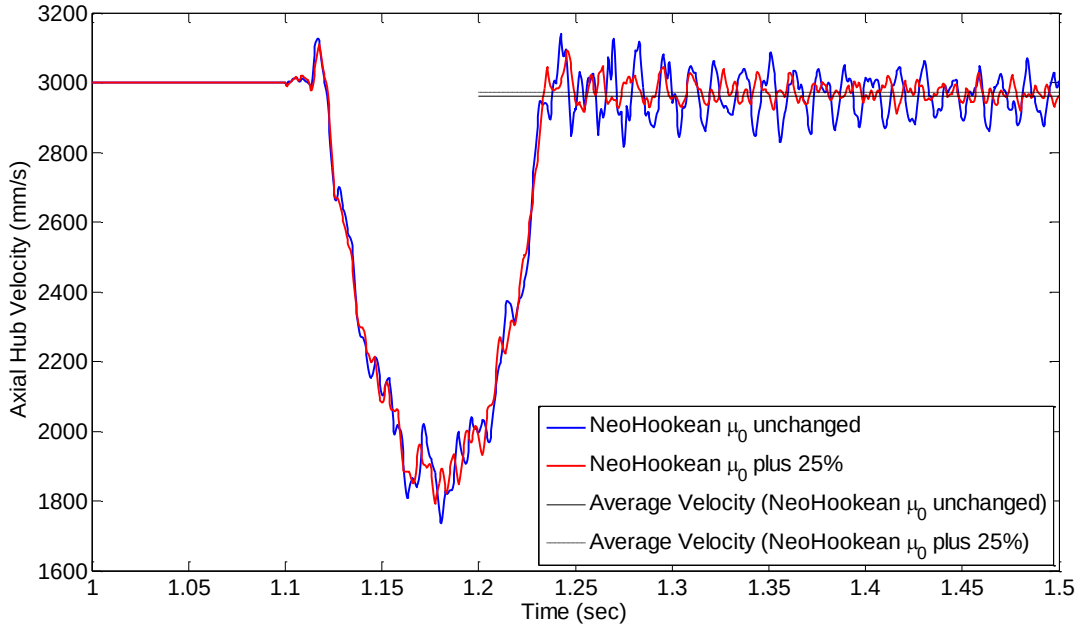

Figure 6.42: Axial hub velocity profile for the Tweel with a Neo Hookean unchanged model (1.28%) and a Neo Hookean increased model (0.958%)

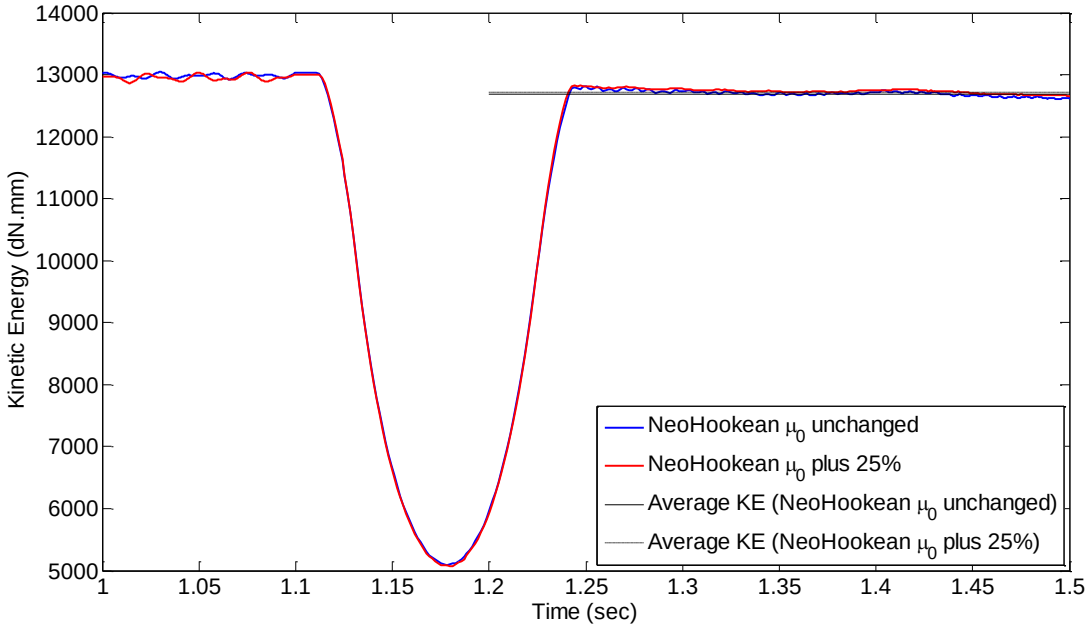

Figure 6.43: Kinetic energy profiles for the Tweel with a Neo Hookean unchanged model (23.3135%) and a Neo Hookean increased model (23.7025%)

6.5 Observations

6.5.1 Reduction in axial hub velocity profile after traversing the obstacle

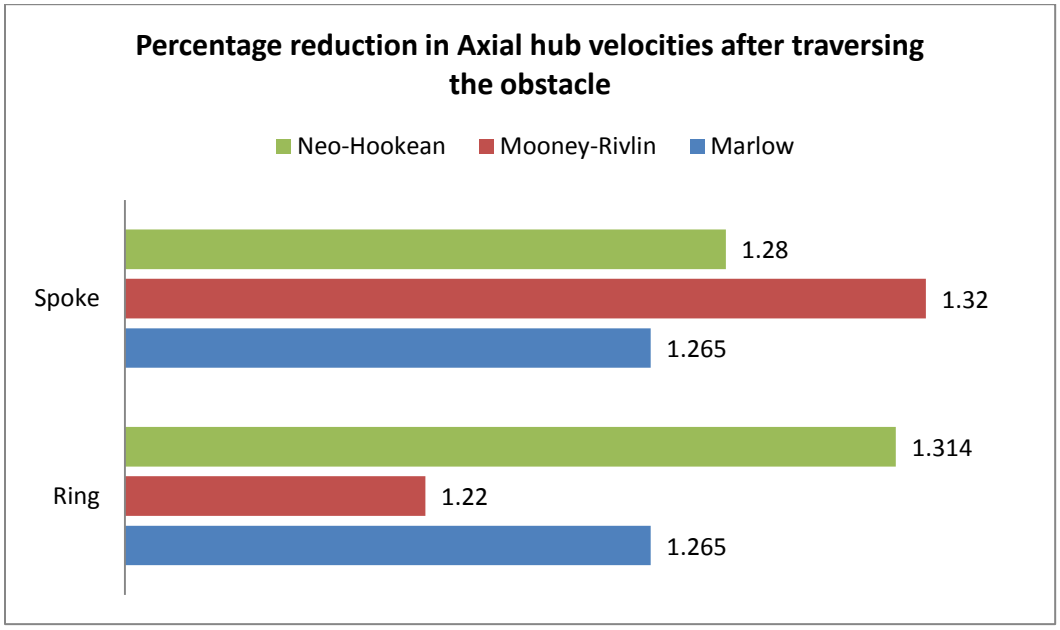

Figure 6.44: Reduction in axial hub velocity of the Tweel with a Mooney Rivlin unchanged model, Neo Hookean unchanged model and Marlow properties.

In Figure 6.44, two sets of values have been provided. One set named 'Ring' refers to the Tweel model with different material models for the ring. The other set 'Spoke' refers to the Tweel model with different material models for the spoke. Three materials have been used for both the ring and the spoke.

When Marlow properties are assigned for the ring and the spokes, it was seen that the reduction was velocity is 1.265%. On the other hand, the reduction in velocity for an analytical rigid wheel was 8.04%. This implies that the Tweel with hyperelastic

properties did not lose a lot of energy on impacting an obstacle when compared with an analytical rigid wheel.

When a Mooney Rivlin unchanged model was used for the ring, the reduction in velocity turned out to be 1.22%. The Tweel with an unchanged Mooney Rivlin model rolled with a slightly higher velocity than the Tweel with Marlow properties. On the other hand, when a Mooney Rivlin unchanged model was used for the spokes, the reduction in velocity was 1.32%. This signifies that the Tweel with the unchanged Mooney Rivlin model rolled with a slightly lower velocity than the Tweel with Marlow properties.

By replacing the Marlow properties for the ring to a Neo Hookean unchanged model, the reduction in velocity was 1.314%. The Tweel with an unchanged Neo Hookean model rolled with a lesser velocity than the Marlow Tweel. When an unchanged Neo Hookean model was used for the spokes, the reduction in velocity was recorded as 1.28%. This implies that the Tweel with an unchanged Neo Hookean model for the spokes rolled with a slightly higher velocity than the Marlow Tweel.

Results show that the reduction in velocity after impacting the obstacle is lower from the Marlow model when an unchanged Mooney Rivlin model is used for the ring. Similarly, the reduction in velocity after impacting the obstacle is higher from the Marlow model when an unchanged Neo Hookean model is used for the ring.

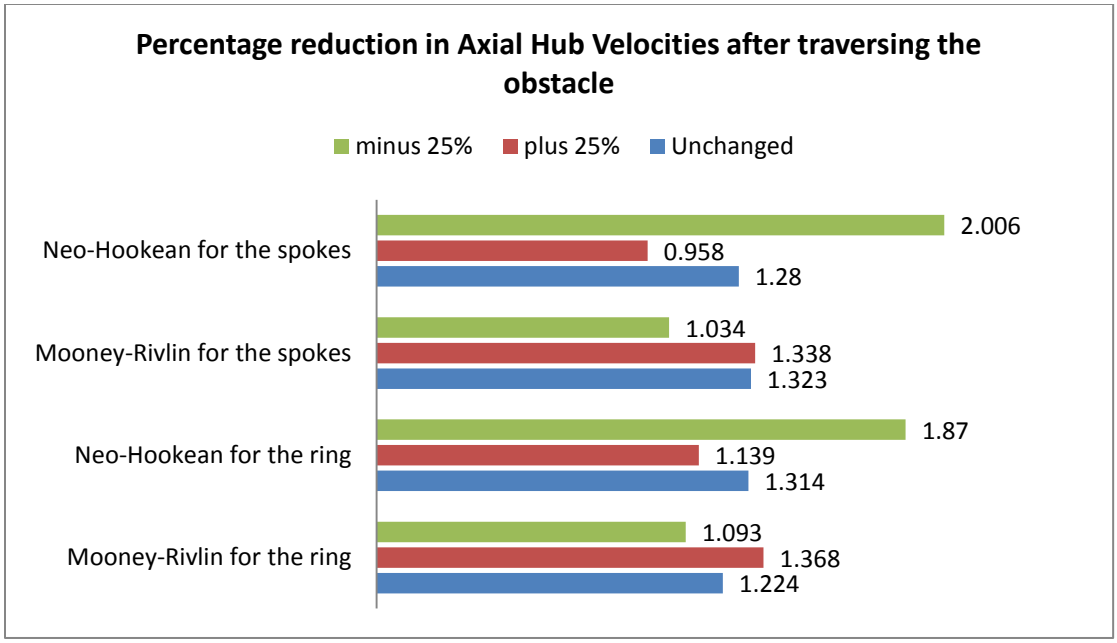

Figure 6.45: Comparison of reduction in axial hub velocities for different levels of Mooney Rivlin and Neo Hookean material models

In Figure 6.45, the reduction in axial hub velocity is compared for different material models. Four sets of values have been provided. The values in the first set are for the models of the Tweel with 3 levels of Mooney Rivlin material model for the ring. The other sets can be explained on similar lines.

When Mooney Rivlin model was used for the ring with three levels, the reduction in velocity of the Tweel with a Mooney Rivlin increased model for the ring is 1.368%. The Tweel with an unchanged Mooney Rivlin model had a reduction in velocity of 1.224%. The unchanged model rolled with a higher velocity than the increased model. On the other hand, the reduced model recorded a reduction in velocity of 1.093%. The

reduced model rolled with a higher velocity than both the increased and the unchanged model.

When Neo Hookean model was used for the ring with three levels, the reduction in velocity of the Tweel with a Neo Hookean increased model for the ring was 1.139%. The Tweel with an unchanged Neo Hookean model had a reduction in velocity of 1.314%. The increased model rolled with a higher velocity than the unchanged model. On the other hand, the reduced model recorded a reduction in velocity of 1.87%. The reduced model rolled with a lower velocity than both the increased and the unchanged model.

When Mooney Rivlin model was used for the spokes with three levels, the reduction in velocity of the Tweel with a Mooney Rivlin increased model for the spokes was 1.338%. The Tweel with an unchanged Mooney Rivlin model had a reduction in velocity of 1.323%. This shows that the unchanged model rolled with a slightly higher velocity than the increased model. On the other hand, the reduced model recorded a reduction in velocity of 1.034%. The reduced model rolled with a higher velocity than both the increased and the unchanged model.

When Neo Hookean model was used for the spokes with three levels, the reduction in velocity of the Tweel with a Neo Hookean increased model for the spokes was 0.958%. The Tweel with an unchanged Neo Hookean model has a reduction in velocity of 1.28%. This shows that the unchanged model rolled with a lower velocity than the increased model. On the other hand, the reduced model recorded a reduction in velocity of 2.006%. The reduced model rolled with a lower velocity than both the increased and the unchanged model.

Results show that the velocity reduced more when the stiffness of the Mooney Rivlin model for both the ring and the spokes was reduced. When the stiffness for the Mooney Rivlin model was increased by 25% for both ring and the spokes, the velocity after traversing the obstacle increased. However, the reduction in velocity was less when the stiffness of the Neo Hookean model was increased for both ring and the spokes. Conversely, the final velocity after traversing the obstacle decreased when a Neo Hookean model with increased shear modulus was used for both the ring and the spokes.

6.5.2 Relative Kinetic energy upon impacting an obstacle

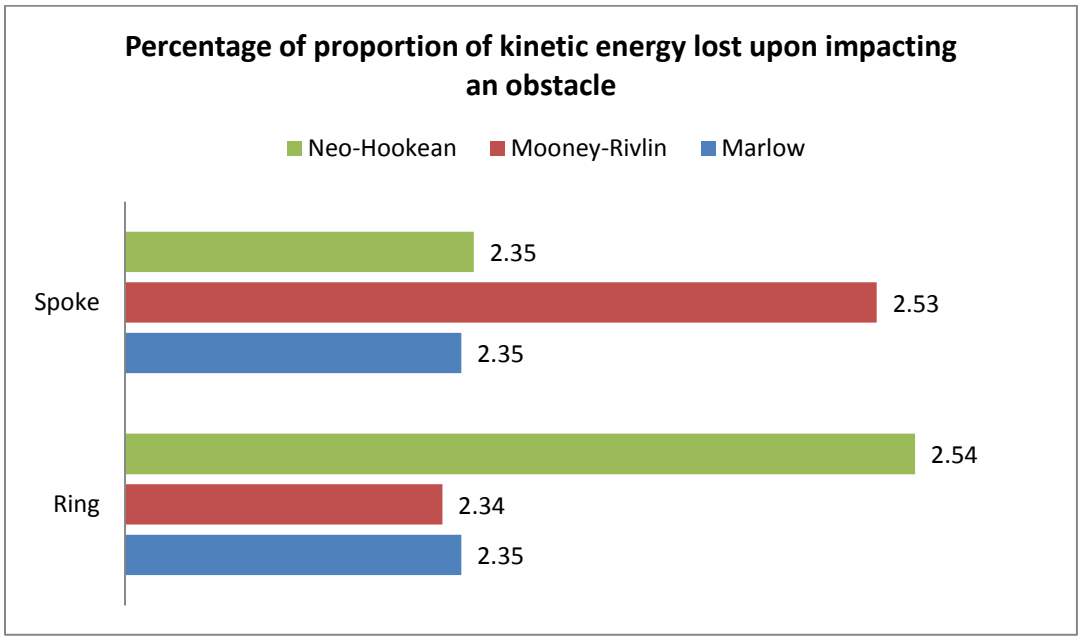

Figure 6.46: Percentage of proportion of energy lost for a Mooney Rivlin unchanged model, Neo Hookean unchanged model and Marlow properties

In Figure 6.46, two sets of results have been provided. 'Ring' denotes the changing material models for the ring. 'Spoke' denotes the changing material models for

the spoke. The proportion of energy loss for the reference model was recorded as 2.3457%.

When the material for the ring was changed to an unchanged Mooney Rivlin model, the proportion of energy loss was 2.3376%. When the same material was used for the spokes, the proportion of energy loss was recorded as 2.5258%.

When an unchanged Neo Hookean model is used for the ring, the proportion of energy lost was 2.5424%. Conversely, the proportion of energy loss was 2.3512% when the same material was used for the spokes.

On comparing with the reference Marlow model, the proportion of energy loss decreased when an unchanged Mooney Rivlin model was used for the ring. The proportion of energy lost increased when the same material was used for the spokes.

The amount of energy lost was higher when an unchanged Neo Hookean model was used for the ring. But when the same material was used for the spokes, the proportion of energy lost decreased.

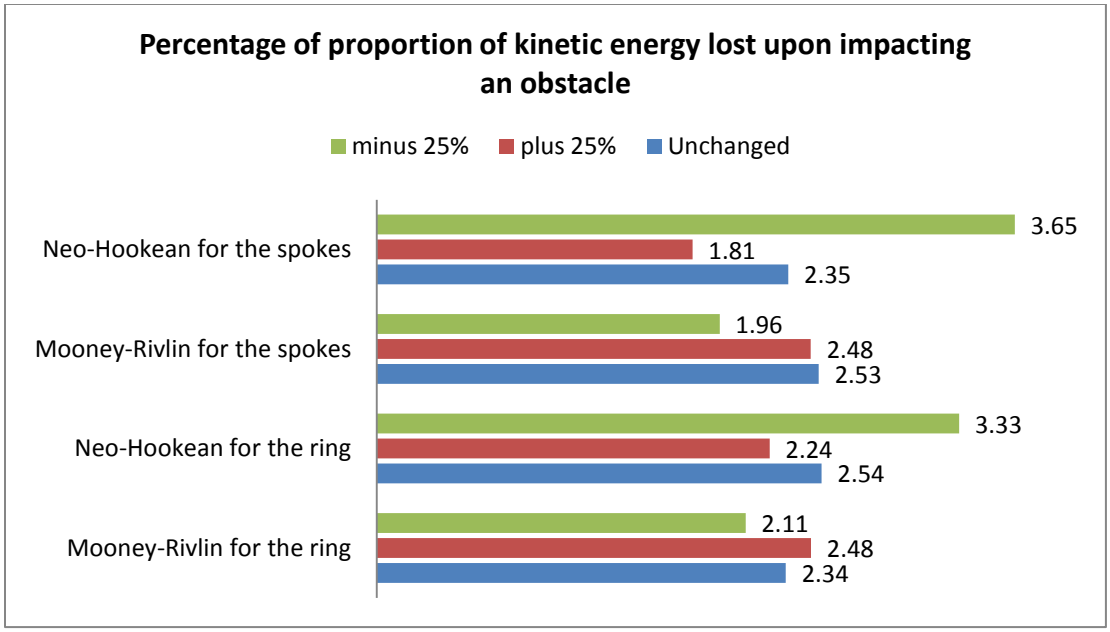

Figure 6.47: Percentage difference of the Kinetic energy values between the different Tweel models and the analytical rigid wheel

In Figure 6.47, there are four sets of values with three levels each. In the first set, Mooney Rivlin material model is considered for the ring. A similar explanation can be given for the remaining 3 sets.

In the first set, the proportion of energy lost for an unchanged Mooney Rivlin model for the ring was recorded as 2.34%. When the stiffness was increased, the proportion of energy loss increased to 2.48%. The proportion of energy loss reduced to 2.11% when the stiffness was reduced.

In the second set, the proportion of energy lost for an unchanged Neo Hookean model for the ring is 2.54%. When the stiffness was increased, the proportion of energy lost reduced to 2.24%. The amount of energy lost increased and the proportion of energy lost increased to 3.33% when the shear modulus was reduced by 25%.

In the third set, when the unchanged Mooney Rivlin model was used for the spokes, the proportion of energy lost was calculated to be 2.53%. This value decreased to 2.48% when the shear modulus was increased. The proportion of energy lost decreased to 1.96% when the shear modulus was reduced.

In the final set, when the unchanged Neo Hookean model was used for the spokes, the proportion of energy lost was recorded as 2.35%. It reduced to 1.81% when the shear modulus was increased by 25%. The proportion of energy lost increased to 3.65% when the stiffness of the Neo Hookean model was reduced by 25%.

Results show that for Mooney Rivlin, a decrease in shear modulus caused a decrease in energy loss. Conversely, for Neo Hookean, a decrease in shear modulus resulted in an increase in energy loss and an increase in shear modulus resulted in a decrease in energy loss.

CHAPTER SEVEN – CONCLUSIONS

7.1 Comparison of Stress-Strain Curves for Hyperelastic Material Models

To study the effect of changes in shear modulus for the ring and spokes while keeping the ratio of volumetric bulk modulus to shear modulus unchanged, the value of shear modulus is varied from Mooney-Rivlin and Neo-Hookean models obtained from a nonlinear least-squares fit of the uni-axial stress-strain data. Upon evaluation of the uni-axial stress-strain data, the results show that on increasing the shear modulus, the tangent slope of the normal stress-strain curve increases; whereas with decreasing shear modulus, the slope decreases. For tensile stresses and strains, the Mooney-Rivlin best matches the original Marlow material model, compared to the simpler Neo-Hookean model. However, for large compressive stresses, the Mooney-Rivlin model diverges significantly from the results obtained with Marlow properties. The simple Neo-Hookean model is able to fit the Marlow curve better for compression, but is less accurate in tension.

7.2 Study of Material Models on Tweel Load-Deflection

As a result of decreasing shear modulus in of the non-pneumatic tire, the vertical displacement in the static load-deflection curves increases upon loading. The stiffness is measured from the slope of the load deflection curve. The stiffness of the Tweel reduced significantly with the Neo Hookean model, while the stiffness with the Mooney Rivlin model only slightly decreased. As expected, when the shear modulus was increased, the stiffness of the Tweel increased and the stiffness decreased when the shear modulus was decreased. The Tweel models are arranged in the ascending order of their stiffness.

7.3 Study of Material Models on Vibration during Rolling

7.3.1 Spoke Vibration

From Figure 5.55, the general trend shown is that the vibration amplitude in the spokes increased when the Marlow properties are changed to either the fitted Mooney Rivlin or Neo Hookean models, with the Neo Hookean model giving the largest vibration amplitudes, especially when Neo Hookean was changed for the spokes. It also appears from these results that changes to spoke material properties have a more significant influence on spoke vibration when compared to changes in ring properties. In summary, the spoke vibration amplitudes for the different material models in the order of increasing magnitudes are: *Marlow* < *Unchanged Mooney Rivlin* < *Unchanged Neo Hookean.*

From Figure 5.56, a general trend is shown that the spoke vibration decreased when the stiffness of the Mooney Rivlin and the Neo Hookean models was increased between the extreme limits of plus and minus 25% change. Conversely, for the extreme limits, vibration amplitudes increased when the stiffness of the Mooney Rivlin and Neo Hookean models was reduced. However, it should be noted that in the case of the unchanged Mooney Rivlin model for the ring, the unchanged gave the smallest amplitude when compared to both the plus and minus extreme limits tested, thus implying that there is an optimal value somewhere between the limits. Another instance where an optimal value occurs can be seen in the Neo Hookean model for the spokes, where the unchanged spoke vibration amplitude was higher than both the plus and minus stiffness limits. Note

also that the unchanged Neo Hookean model for the spokes had the largest amplitude when compared to all models. In summary, the amplitudes for spoke vibration for the different materials in order of increasing magnitudes for the four sets of data are:

(a) Mooney Rivlin for ring: Unchanged < +25% < -25%

(b) Neo Hookean for ring: +25% < Unchanged < -25%

(c) Mooney Rivlin for spokes: +25% < Unchanged <-25%

(d) Neo Hookean for spokes: +25% < -25% < Unchanged

7.3.2 Ground Vibration

From Figure 5.57, when considering ground vibration, a trend is shown that the vibration levels increased when the referenced Marlow model was replaced with a least square fitted Mooney Rivlin and Neo Hookean models. The Neo Hookean model for both ring and spokes produced large vibrations compared to both Mooney Rivlin and Marlow models. The largest ground vibration amplitude occurs with the Neo Hookean model for the spokes. The ground vibration amplitudes for the different material models in the order of increasing magnitudes are: *Marlow < Unchanged Mooney Rivlin < Unchanged Neo Hookean.*

From Figure 5.58, similar to trends found in the spoke vibration, on varying the stiffness of the different material models for the ring and the spoke, a trend is shown that the vibration decreased when the stiffness of the Mooney Rivlin and the Neo Hookean models was increased from +25% to -25%. Conversely, the vibration increased when the stiffness decreased between the extreme limits. However, In the case of the Neo-Hookean material for the ring and Mooney Rivlin for the spokes, the Unchanged stiffness gave the lowest vibration amplitude, suggesting that a optimal value is somewhere

between the plus/minus 25% stiffness limits. Similar to spoke vibration, the unchanged Neo Hookean model for the spokes had the largest ground vibration amplitude when compared to all models. The amplitudes for ground vibration for the different materials, with plus/minus 25% change in stiffness, in order of increasing magnitudes for the four sets of data are:

(a) Mooney Rivlin for ring: +25% < Unchanged < -25%

(b) Neo Hookean for ring: Unchanged < +25% < -25%

(c) Mooney Rivlin for spokes: Unchanged < +25% < -25%

(d) Neo Hookean for spokes: +25% < -25% < Unchanged

7.4 Energy Loss Study

To study the effects of material changes on energy loss from impact rolling over obstacles, reduction in axial hub velocities and proportion of energy lost by different materials models were studied and compared. From Figure 6.16 and Figure 6.17, a general trend is shown that the axial velocity and kinetic energy of the Tweel after traversing the obstacle reduced slightly when Marlow properties for the ring were replaced by a least square curve fit model of Mooney Rivlin. Conversely, these parameters increased when the same model was used for the spokes. However, when a least square curve fit Neo Hookean model was used for the ring and spokes, the parameters increased and decreased respectively. The energy reduction after impact rolling over the obstacle with height 7.5% of the radius of the Tweel, and for the rolling speed of 3000 mm/sec, for the different materials in the ring and spokes in order of increasing energy loss are:

(a) Ring: Neo Hookean < Marlow < Mooney Rivlin,

(b) Spokes: Mooney Rivlin < Neo Hookean < Marlow.

When the stiffness of the Tweel with Mooney Rivlin and Neo Hookean material models was varied, a general trend in the final velocity and kinetic energies after traversing the obstacle was seen. The final axial velocity and kinetic energy (KE) reduced when the stiffness of a least square curve fit Mooney Rivlin model was increased for both the ring and the spokes. Conversely, the values of these parameters increased with the reduction in stiffness. On the other hand, when the stiffness of the Neo Hookean model for both ring and spokes was increased, the final velocity and KE increased. A reduction in the values of the final velocity and KE was seen when the stiffness of the Neo Hookean model was reduced. The Neo Hookean models with reduced shear modulus for the ring and the spokes showed the largest reduction in final velocity and KE. It is inferred that the percentage reduction in velocity and proportion of energy lost are directly proportional to the final velocity and KE respectively. In summary, the energy reduction after impact rolling over the obstacle with height 7.5% of the radius of the Tweel, for the different materials in the ring and spokes, with plus/minus 25% change in stiffness, in order of increasing energy loss are:

(a) Mooney Rivlin for ring: +25% < Unchanged < -25%

(b) Neo Hookean for ring & spokes: -25% < Unchanged < +25%

(c) Mooney Rivlin for spokes: Unchanged < +25% < -25%

7.5 Future Work

In the present work, changes to material stiffness were made independently for the spoke properties and ring properties. In future work, changes in material stiffness to both the spoke and ring properties would be done together, rather than separate. This could provide a more fundamental understanding of the effects of different materials on the behavior of energy loss and vibration for the Tweel. In addition, the effects of visco-elastic damping can also be investigated.

For the energy loss after impact rolling over obstacles, the effects of geometric design parameters such as spoke length and curvature, ring thickness, etc. could be investigated to optimize the Tweel for low energy loss. Parameter studies on the changes in energy loss at different rolling speeds and obstacle heights could be investigated. Effects of reducing ground surface traction, so that slip between the wheel and ground occurs when traversing the obstacle could also be studied.

REFERENCES

1. Rhyne, T. B. and Cron, S. M., ‘‘Development of a Non-Pneumatic Wheel,’’ *Tire Science and Technology*, TSTCA, Vol. 34, No. 3, July – September 2006, pp. 150-169

2. Cron, S., *Use of Connectors in Abaqus/Explicit to Simulate Dynamic Motion Along a Curved Path*, in *2004 ABAQUS User's Conference*. 2004.

3. Manga, K.K., 2008, “Computation Method for Solving Spoke Dynamics on High Speed Rolling Tweel™,” Master’s Thesis, Clemson University, Clemson, SC.

4. Ramachandran, M., 2008, “Nonlinear Finite Element Analysis of Tweel™ Geometric Parameter Modifications on Spoke Dynamics during High Speed Rolling” Master’s Thesis, Clemson University, Clemson, SC.

5. Rutherford, W., 2009, “Use of Orthogonal Arrays for Efficient Evaluation of Geometric Designs for Reducing Vibration of a Non-Pneumatic Wheel during High-Speed Rolling,” Master’s Thesis, Clemson University, Clemson, SC.

6. Bezgam, S., 2009, “Design and analysis of alternating spoke Pair concepts for a non-pneumatic tire with reduced vibration at High speed rolling”, Master’s Thesis, Clemson University, Clemson, SC.

7. Proddaturi, A., ”Robust Parameter Design and Finite Element Analysis for a Non Pneumatic Tire with Low Vibration”, Master’s Thesis, Clemson University, Clemson, SC.

8. Manga, K.K., Thompson, L.L., Ziegert, J.C., Rhyne, T.B., and Cron, S.R., "Computational Method to Examine Spoke Dynamics in a High Speed Rolling Wheel", Paper SAE-2009-01-0071, April 2009.

9. Maya Ramachandran, Shashank Bezgam, Lonny L. Thompson, John C. Ziegert, Timothy B. Rhyne, Steven M. Cron, “On the effects of edge scalloping for collapsible spokes in a non-pneumatic wheel during high speed rolling”, ASME International Mechanical Engineering Congress and Exposition, IMECE2009, Nov 13-19, 2009, Lake Buena Vista, Florida, USA, ASME Paper IMECE2009-11342.

10. William Rutherford, Shashank Bezgam, Amarnath Proddaturi, Lonny Thompson, John C. Ziegert , Timothy B. Rhyne, Steven M. Cron, "Use of Orthogonal Arrays for Efficient Evaluation of Geometric Designs for Reducing Vibration of a Non-Pneumatic Wheel during High-Speed Rolling", Presented at the September 2009 Meeting of the Tire Society, to appear in journal *Tire Science and Technology, 2010.*

11. Steven M. Cron, "Role of Abaqus in the Development of the Michelin Tweel® Tire", Proceedings of the 2010 Simulia Users Conference, Providence, Rhode Island.

12. Abaqus Analysis User Manual

13. http://en.wikipedia.org/wiki/Orthotropic_material

14. Shashank Bezgam, Lonny Thompson, John C. Ziegert , Timothy B. Rhyne, Steven M. Cron, "Numerical study of vibration of an alternating spoke pair design concept for a non-pneumatic tire during high-speed rolling", presented at the 2010 Tire Society meeting, and for consideration for publication in the journal Tire Science and Technology.

15. http://www.oofem.org/resources/doc/matlibmanual/node6.html

16. http://en.wikipedia.org/wiki/Poisson_ratio

17. ABAQUS CAE/User's Manual

18. Meriam J.L. and Kraige, L.G., *Dynamics,* Wiley, 2007.

19. Abaqus Theory Manual

APPENDIX

Appendix A:Analytical model of a Rigid Wheel

Consider a rigid wheel of mass ‘m’, and outer radius R, rolling over a flat ground until the wheel impacts an obstacle of height ‘b’; see Figure Appendix 1. The center of gravity for the rigid wheel is denoted by point G, and the point where the wheel comes in contact with the obstacle is denoted by C.

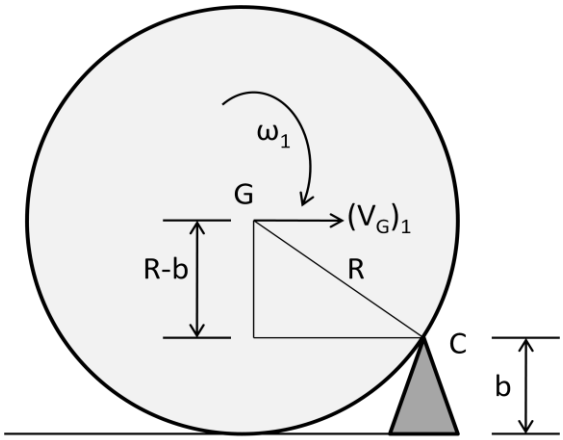

Appendix 1: Rigid wheel just before the first impact

The rigid wheel impacts twice when it rolls over the obstacle. The first impact is when the wheel strikes the obstacle and the second impact is when the rigid wheel strikes the ground after traversing the obstacle. When the wheel first impacts the obstacle, its motion is assumed to change almost instantaneously from rolling without slip on the ground to a fixed axis rotation about the point of impact. Let $(h_c)_1$ be the angular momentum about the contact point C just before the first impact and let $(h_c)_2$ be the angular momentum about point C just after the first impact. Assume that there is an infinitesimal time interval right after impact between the wheel and contact point, in

which the wheel does not change position significantly, and does not lose contact with the round. The angular impulse-momentum equation about point C can be written as,

$$(h_c)_1 + \int \sum M_c dt = (h_c)_2$$

Neglecting non-impulsive forces, the angular impulse defined by integral term can be neglected or approximated to zero since the time interval of impact is extremely small, and the impact force is assumed to have its line of action thru point C. In this case, angular momentum is conserved about point C, and the above equation is approximated as,

$$(h_c)_1 = (h_c)_2$$

The angular momentum about point C is defined by the angular momentum

$$(h_c)_1 = I_G \omega_1 + m(V_G)_1 (r - b)$$

Assuming no slip condition and using the kinematic equation $(V_G)_1 = \omega_1 R$ and $I_G = m k_G{}^2$, the above expressions simplifies into,

$$(h_c)_1 = m(V_G)_1 R \left(1 + \left(\frac{k_G}{R} \right)^2 - \frac{b}{R} \right)$$

From Figure Appendix 2, just after impact, the wheel is assumed change direction such that the direction of velocity is parallel to the tangent to the rigid wheel passing

through the point of contact C. This is because the coefficient of restitution is assumed to be zero, (i.e.), the normal component of velocity after impact is considered to be zero. The model then assumes that the wheel sticks to the obstacle and pivots around C.

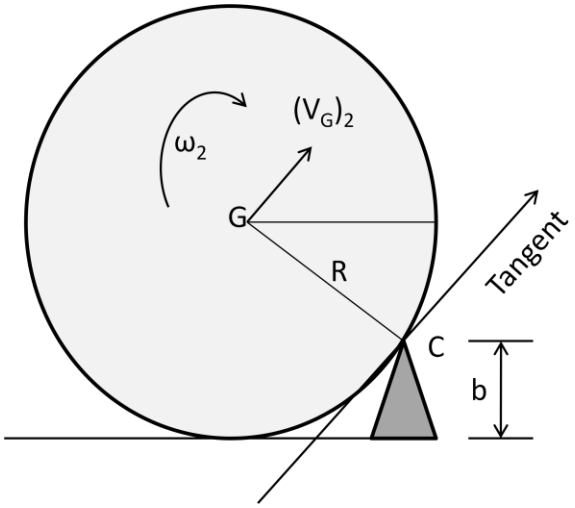

Appendix 2: Rigid wheel after first impact

Similar to the earlier derived expressions, the angular momentum just after the initial impact is given as,

$$(h_c)_2 = I_G\omega_2 + m(V_G)_2 R$$

Assuming no slip condition and using the kinematic relation $(V_G)_2 = R(\omega_G)_2$ and $I_G = mk_G^{\ 2}$, the above expression simplifies to,

$$(h_c)_2 = -m(V_G)_2 R\left(1+\left(\frac{k_G}{R}\right)^2\right)$$

From conversion of angular momentum about C, $(h_c)_1 = (h_c)_2$, the speed just after impact can be written in terms of the speed just before impact as;

$$(V_G)_2 = \left[1 - C\frac{b}{R}\right](V_G)_1$$

where

$$C = \left(1 + \left(\frac{k_G}{R}\right)^2\right)^{-1}$$

This is the velocity of the rigid wheel after the first impact, (i.e.), after it strikes the obstacle. After traversing the obstacle, the rigid wheel again makes contact with the flat ground. This is considered to be the second impact. Assuming the wheel pivots about C, the speed just before impacting the ground $(V_G)_2$ is the same as the speed just after the first impact with direction parallel to the tangent plane rotated 90 degrees about C. The point of impact when the rigid wheel makes contact with the ground is denoted as P.

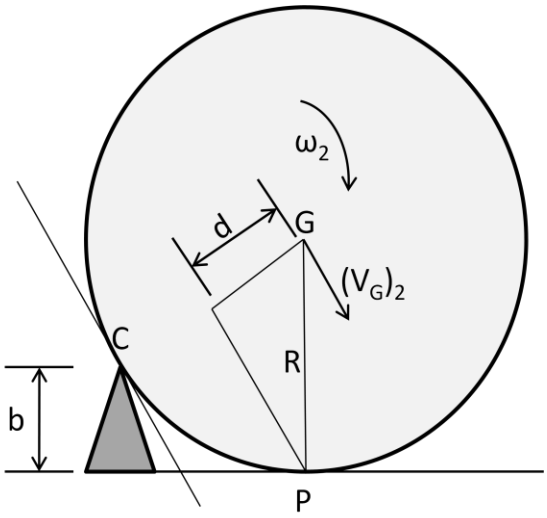

Appendix 3: Rigid wheel just before the second impact

On neglecting non-impulsive forces and conserving angular momentum about the point P,

$$(h_p)_2 = (h_p)_3$$

The angular momentum just before impact about point P is,

$$(h_p)_2 = I_G\omega_2 + m(V_G)_2 d$$

where $d = r\text{-}b$. Using no slip condition $(V_G)_2 = R\omega_2$, the above expression can be expressed as

$$(h_p)_2 = m(V_G)_2 R\left(\left(\frac{k_G}{R}\right)^2 + 1 - \frac{b}{R}\right)$$

Once the wheel impacts the ground, it is assumed once again that the coefficient of restitution is zero, (i.e.), no bounce or rebound is considered. In such a case, the normal

(vertical) speed is zero and hence the rigid wheel is constrained to move horizontally. Appendix 4 shows the motion of the rigid wheel after impacting the ground.

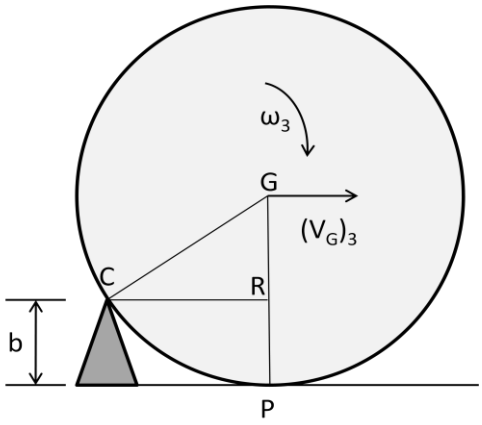

Appendix 4: Rigid wheel just after the second impact

The angular momentum about P after impact is,

$$(h_p)_3 = m(V_G)_3 R\left(1+\left(\frac{k_G}{R}\right)^2\right)$$

Using principles of conservation of angular momentum before and after the second impact, the final velocity with which the rigid wheel travels after traversing the obstacle is given to be,

$$(V_G)_3 = \left[1-C\frac{b}{R}\right](V_G)_2 = \left[1-C\frac{b}{R}\right]^2 (V_G)_1,$$

where $C = \dfrac{1}{1+\left(\dfrac{k_G}{R}\right)^2}$

Note the square on the term on the bracket appears due to the two impact events during wheel traversing the obstacle. Using the notation $V_i = (V_G)_1$ and $V_f = (V_G)_3$, the relative change in velocity before impact and after traversing the obstacle is

$$\frac{\Delta V}{V_i} = \frac{V_i - V_f}{V_i} = 1 - \left[1 - C\left(\frac{b}{R}\right)\right]^2$$

The rigid-body kinetic energy for general motion of the rigid wheel is given by

$$E_K = \frac{1}{2} m V_G{}^2 + \frac{1}{2} I_G \omega^2$$

Assuming no-slip kinematics

$$\omega = V_G / R$$

The kinetic energy can be written as,

$$E_K = \frac{1}{2} m \left(1 + \left(\frac{k_G}{R}\right)^2\right) V_G{}^2$$

The initial rigid body kinetic energy is

$$E_i = \frac{1}{2} m \left(1 + \left(\frac{k_G}{R}\right)^2\right) V_i^2$$

The final kinetic energy for the rigid wheel after traversing the obstacle is

$$E_f = \frac{1}{2} m \left(1 + \left(\frac{k_G}{R} \right)^2 \right) V_f{}^2 = \frac{1}{2} m \left(1 + \left(\frac{k_G}{R} \right)^2 \right) \left[1 - C \frac{b}{R} \right]^4 V_i^2$$

Thus the kinetic energy loss is given by,

$$\frac{\Delta E}{E_i} = \frac{E_i - E_f}{E_i} = 1 - \left[1 - C \left(\frac{b}{R} \right) \right]^4$$